CENTRAL AMERICAN GAP WINDS' IMPACT ON EASTERN NORTH PACIFIC TROPICAL CYCLONES

A Dissertation

by

DAN FU

Submitted to the Office of Graduate and Professional Studies of
Texas A&M University
in partial fulfillment of the requirements for the degree of

DOCTOR OF PHILOSOPHY

Chair of Committee,	Ping Chang
Co-Chair of Committee,	Lixin Wu
Committee Members,	R. Saravanan
	Christina M. Patricola
Head of Department,	Shari Yvon-Lewis

August 2018

Major Subject: Oceanography

ABSTRACT

Hurricane Patricia in 2015 was the second-strongest tropical cyclone on record worldwide, with a maximum surface wind speed of 215 mph (~ 96m s^{-1}). Although Patricia fortuitously spared major cities, it reminded us of the threat tropical cyclones (TCs) pose in the eastern North Pacific (ENP) and the importance of improving our understanding and prediction of ENP TCs.

Patricia's intensity and the hyperactive 2015 ENP hurricane season have been partially attributed to the strong El Niño; however, there is still a lack of fundamental understanding of the relationship between the El Niño-Southern Oscillation (ENSO) and ENP TCs. In addition to being an active TC region, the ENP is also characterized by a unique topographically-locked feature, the Central American gap winds (CAGW). Here, we demonstrate that ENSO modulates ENP TCs in distinct spatial patterns, with enhanced (reduced) TC occurrence in the western portion of the ENP during El Niño (La Niña), but reduced (enhanced) TC occurrence in the eastern nearshore area, where landfalling TCs preferentially form. This intrabasin difference is primarily driven by ENSO-induced anomalous CAGW variability, which intensify (weaken) during El Niño (La Niña), producing low-level anticyclonic (cyclonic) relative vorticity anomalies and thus an unfavorable (favorable) environment for TC genesis.

Besides ENSO-related CAGW's modulation, the synoptic CAGW events also have great influences on ENP TCs. Many satellite observations reveal that

CAGW-induced cyclonic vorticity can trigger cyclogenesis especially when it interacts with the monsoon trough and easterly waves. Therefore understanding the distinct roles that the synoptic versus seasonal timescale CAGW play in modulating ENP TCs is of particular importance. To estimate CAGW's contributions on ENP TCs, we performed numerical simulations with a high-resolution (27km) TC-permitting tropical channel model (TCM).

Two sets of experiments were performed for the 1990-2016 hurricane seasons. By closing mountainous gaps at Tehuantepec (TT) and Papagayo (PP), ENP TC activity significantly decreases about 25%, and ENSO-driven intrabasin variability is greatly eliminated. Analysis shows that CAGW-induced vorticity primarily contributes to this reduction, while reduced vertical wind shear offsets this unfavorable environmental condition by some degree. Furthermore, the CAGW-affiliated mid-level aridification is also responsible for this TC suppression.

DEDICATION

I dedicate this dissertation to my wife, Xue Liu, and our newborn daughter, Evelyn Fu. You are my deepest motivations that inspire me to pursue self-improvement. Love you forever!

ACKNOWLEDGEMENTS

I would like to express my sincerely gratitude to my advisor, Prof. Ping Chang, for his expert guidance, patience and encouragement throughout the course of my Ph.D. study. His sharp mind in sciences and many constructive suggestions are highly appreciated. Without his persistent and illuminating instructions, this dissertation would not have been possible. His perspective insight and responsible attitude into scientific research not only benefit my study here but also illumine my future endeavors.

I would also like to thank my Co-Chair Prof. Lixin Wu as well as my committed members, Prof. Ramalingam Saravanan and Dr. Christina Marie Patricola for their constructive comments and many inspiring discussions during the study here. Dr. Christina Marie Patricola has provided me detailed and patient instructions on running the tropical channel version of WRF. Without her help, I would not have completed the numerical simulations used in this dissertation.

I would like to thank my colleagues during my Ph.D. study over the past few years. A special thank goes to Chuan-Yuan Hsu who instructed me to improve my usage of Linux language and coding skills. My grateful thanks are also extended to Wei-Ching Hsu for our inspiring discussions. Profs. Shari Yvon-Lewis and all of other faculty members of the Department of Oceanography, Texas A&M University, are also appreciated for their friendships and instructional teachings during my graduate study. They broaden my scientific insights.

I am grateful to China Scholarship Council for their financial support. I am also grateful to the Texas A&M University Supercomputing Facility and the Texas Advanced Computing Center (TACC) at the University of Texas at Austin, which provided the computing resources used in this dissertation.

The deepest gratitude is given to my wife, Xue Liu, for her endless love and always understanding and continuous encouragement throughout all of our years at Texas A&M University, which motivates me and gives me confidence to complete my study. I also would like to express my heartfelt thanks to my parents and parents in law for their solid supports in our daily lives. Finally, I would like to thank my little daughter, Evelyn Fu. She brings more brightness to our lives.

CONTRIBUTORS AND FUNDING SOURCES

Contributors

This work was supervised by a dissertation committee consisting of Professor Ping Chang, Professor Lixin Wu of the Department of Oceanography and Professor Ramalingam Saravanan of the Department of Atmospheric Science and Dr Christina Marie Patricola of the Climate and Ecosystem Sciences Division at Lawrence Berkeley National Laboratory.

All work for the dissertation was completed independently by the student.

Funding Sources

Graduate study was supported by a fellowship from Texas A&M University and China Scholarship Council.

NOMENCLATURE

ACE	Accumulated Cyclone Energy
CAGW	Central American Gap Winds
CCMPv2	Cross-Calibrated Multi-Platform Version 2
CFSR	Climate Forecast System Reanalysis
CFSv2	Climate Forecast System Version 2
CISK	Conditional Instability of the Second Kind
EDR	Eastern Development Region
ENP	Eastern North Pacific
ENSO	El Niño-Southern Oscillation
IBTrACS	International Best Track Archive for Climate Stewardship
CTL	Control Simulation
NOGAP	Non-Gap Simulation
GPI	Genesis Potential Index
NA	North Atlantic
NCEP	National Center for Environmental Prediction
NHC	National Hurricane Center
PDI	Power Dissipation Index
PI	Potential Intensity
PP	Papagayo

QuikSCAT	Quick Scatterometer
RRTM	Rapid and Accurate Radiative Transfer Model
SST	Sea Surface Temperature
TC	Tropical Cyclone
TCM	Tropical Channel Model
TRMM	Tropical Rainfall Measuring Mission
TT	Tehuantepec
VWS	Vertical Wind Shear
WDR	Western Development Region
WISHE	Wind-Induced Surface Heat Exchange
WMO	World Meteorological Organization
WNP	Western North Pacific
WRF	Weather Research Forecasting
YOTC	Year of Tropical Convection

TABLE OF CONTENTS

LIST OF FIGURES

Page

LIST OF TABLES

Page

CHAPTER I

INTRODUCTION

1.1 Background

1.1.1 Eastern North Pacific hurricane seasons

A tropical cyclone (TC) is a rapidly rotating vortex system with organized clouds and thunderstorms that originates over global tropical or subtropical oceans. A TC is typically characterized by a closed low-level atmospheric circulation surrounded by strong winds and a low-pressure center inside, and it is one of the most intense and destructive natural hazards that poses a great threat to lives and properties.

The eastern North Pacific (ENP) basin (0-30°N, 140°W-80°W) is the most active TCs genesis region in the globe, in terms of genesis per unit area and per unit time (Molinari et al., 2000). Climatologically, ENP TC activity begins in early June and lasts until the end of November, with peak activity in late August and early September. The National Hurricane Center (NHC) defines the ENP hurricane season from May 15th to November 30th, which accounts for more than 95% (792 out of 832) of the total number of TCs that occurred during 1970-2015. On average, about 16 named TCs form in this region each hurricane season, accounting for 19% of global named TCs, 9 of which can further intensify to hurricanes (Romero-Vadillo et al., 2007; Zhao and Raga, 2015), with maximum sustained winds of 33 m/s (64 knots) or higher.

Due to their dominant westward mean trajectories, ENP TCs often propagate towards the open ocean, and the landfall ratio (landfall events per total TCs) is relatively small compared with other basins. Possibly for this reason, studies of ENP TCs have received less attention compared to other basin TCs. However, the importance of ENP TCs should not be overlooked because they not only can inflict destructive power on the Hawaiian Islands (Chu and Wang, 1997), but also have a strong ability to regulate Central America and southwestern North America summer precipitation, causing potential canyon floods when TC-associated winds and moisture interact with mountainous topography (Ritchie et al., 2011; Wood and Ritchie, 2013; Englehart and Douglas, 2001, 2002). The enlightening examples are the devastating coastal flooding triggered by Hurricane Pauline in 1997 and Patricia in 2015. The latter is the strongest hurricane on record for the Western Hemisphere and inflicted an estimated $460 million USD damage across Mexico and Southern Texas (Avila, 2015; Kimberlain et al., 2016). Therefore, gaining a better understanding of ENP TC activity has both outstanding scientific motivation and profound socioeconomic implications.

1.1.2 Variability of TCs over ENP

El Niño-Southern Oscillation (ENSO) is the most dominant mode of climate variability on interannual timescales (Rasmusson and Carpenter, 1982; Philander, 1990). Atmospheric variations in the ENSO cycle are manifested in the sea-level pressure (SLP) difference oscillation between Tahiti and Darwin, Australia. Oceanic variations are characterized by sea-surface temperature (SST) fluctuations in the central-to-eastern

equatorial Pacific that are gauged by the Niño3 (5°S-5°N, 160°E-150°W) and Niño3.4 (5°S-5°N, 170°W-120°W) index. Through its effect on global atmospheric circulation and upper tropical oceans, ENSO can strongly modulate TC activity (Landsea, 2000; Chu, 2004), but its specific influence on TCs varies from basin to basin (Bove et al., 1998; Nicholls, 1979; Chan, 1985; Gray, 1984a). In general, the North Atlantic (NA) experiences below-normal TC occurrence, intensity, as well as U.S. landfall ratio during El Niño, and above-normal during La Niña (Gray, 1984a; Tang and Neelin, 2004; Bove et al., 1998), whereas ENSO's influence on Western North Pacific (WNP) TCs appears to be mainly limited to TC intensity, location and track, with little influence on TC frequency (Chan, 1985; Wang and Chan, 2002).

In addition to NA and WNP TCs, ENSO also impacts ENP TC activity. During El Niño, vertical wind shear over the ENP is reduced in response to anomalously warm central-to-eastern Equatorial Pacific SST, which tends to favor above-normal ENP TC activity (Landsea, 2000). Anomalously large eastern Pacific ocean heat content during El Niño can also affect TC intensity (Jin et al., 2014). However, whether there is a statistically robust relationship between ENSO and observed TC activity over the ENP has been called into question (Gray and Sheaffer, 1991; Whitney and Hobgood, 1997; Ralph and Gough, 2009). By longitudinally subdividing the ENP main development region (MDR; 8°N-20°N, 140°W-85°W) into a Western Development Region (WDR) and Eastern Development Region (EDR) along 112°W, recent studies found that only TCs that originated in the WDR are robustly correlated with ENSO (p-value < 0.05), with

more frequent and intense TCs observed during El Niño than La Niña (Collins and Mason, 2000; Ralph and Gough, 2009; Collins, 2007; Jien et al., 2015). Locations of TC genesis and dissipation within the ENP are also characterized by a westward shift during El Niño compared to neutral ENSO and La Niña (Irwin and Davis, 1999). Such a TC response in the WDR has been attributed to changes in SST and mid-tropospheric relative humidity during ENSO (Collins, 2007; Collins, 2016). However, ENSO's impact on TCs in the EDR, which have a much higher probability to make landfall along the Pacific coast of Central America, has not been thoroughly investigated. There is currently no consensus on whether and how ENSO can exert an influence on TCs in the EDR.

Besides ENSO's impact, a recent study (Patricola et al., 2016) also identified a remote impact of tropical Atlantic SST variability on ENP TC activity. As a dominant mode of Atlantic climate variability on interannual-to-decadal time scales, the Atlantic Meridional Mode (AMM; Chang et al., 2000; Chiang and Vimont, 2004) is given to be able to remotely modulate environmental favorability of ENP tropical cyclogenesis. During the positive phase of the AMM, in which the SST in the Northern Tropical Atlantic is anomalously warm, ENP TC activity tends to be below normal, while it is above normal during AMM negative phase. This result reveals that AMM associated SSTs in the tropical Atlantic, albeit weaker than those associated with ENSO, are also an important factor for ENP TC activity, and highlights the importance of considering both changes in interannual tropical Pacific and Atlantic variability in seasonal ENP TC predictions.

1.1.3 Central American Gap Winds and their impact on ENP TCs

Besides the highest density of tropical cyclogenesis, the ENP features some distinctive characteristics in atmospheric and oceanic environment due to the presence of the Sierra Madre mountain range in Central Americas. This mountain range has an average height of 1000m with peaks reaching above 3000m, blocking low-level flows from the Gulf of Mexico and the Caribbean Sea. However, the barrier created by the Sierra Madre is punctuated by three main narrow mountainous gaps with only 250m elevations located at the Isthmus of Tehuantepec (TT), Gulf of Papagayo (PP), and in Central Panama (PN). The depth of these gaps can approach ~1000 meters vertically (Figure 1.1). During boreal winter (November through March), intermittent winter storms from the Gulf of Mexico and more steady trade winds force strong wind jets penetrating through these narrow gaps and into the ENP, generating the Central American Gap Winds (CAGW; Steenburgh et al., 1998; Chelton et al., 2000a; Chelton et al., 2000b; Romero-Centeno et al., 2007). The sustained wind velocity of CAGW can exceed 20m/s, with a maximum event of 49.9 m/s recorded by ship observation near TT in February 1974 (Stumpf, 1975; Schultz et al., 1997). The intense surface winds can significantly reduce SST through strong wind-driven mixing, particularly in the Gulf of Tehuantepec during boreal winter (Sun and Yu, 2006; Liang et al., 2009). Although the CAGW at TT and PP are strongest during boreal winter, they are also characterized by the secondary peaks during July-August caused by the westward intensification of the Azores-Bermuda high pressure system (Chelton et al., 2000a; Romero-Centeno et al., 2007).

Since the secondary peak of CAGW occurs within ENP hurricane seasons, how near-surface vorticity fields generated by these gale-force low-level jets that funnel through topographic gaps can influence the development of ENP TCs becomes a very important issue. Understanding this issue can improve not only our understanding of dynamical processes of tropical cyclogenesis, but also seasonal TC forecasts in the region that can alleviate the potential threat of TCs in the ENP.

Although formation mechanisms for TCs still remain to be fully unraveled, two main theories exist for tropical cyclogenesis. These are known as the 'bottom-up' and 'top-down' theory, which are distinguished by whether positive feedback loops begin from surface or mid-level. The well-known CISK (Conditional Instability of Second Kind; Charney and Eliassen, 1964) and WISHE (Wind Induced Surface Heat Exchange; Emanuel, 1986) are among the most prominent 'bottom-up' theories. These theories reason that near-surface or low-level cyclonic circulation (low-pressure system) causes convection, resulting in rising motion of sufficiently heated water vapor (CISK) and upward transport of sea-surface heat (WISHE), which in turn causes the release of latent heat and further strengthens the low-level cyclonic circulation and convection, forming a positive feedback loop. In contrast, the 'top down' theory (Ritchie and Holland, 1997; Simpson et al., 1997) emphasizes the downward propagation of vorticity due to interactions between mid-level mesoscale vortices and low-level cyclonic circulation, which strengthens the near-surface vortex structure and help to develop a more cohesive rotating system. Although none of these theories can completely explain TC formation,

they all emphasize the importance of the existence of an initial low-level or near-surface cyclonic vorticity for tropical cyclogenesis and further development.

The earliest studies related to the topic of CAGW and ENP TCs formation trace back to early 1990s. Using simple two-dimensional models, previous studies found that surface cyclonic vorticity can be generated in the lee side of an idealized terrain with gaps similar to Sierra Madre (Zehnder 1991; Zehnder and Gall, 1991; Mozer and Zehnder, 1996). With the availability of atmospheric reanalysis data, analyses further support the notion that CAGW can induce surface cyclonic vorticity. Of particular note are the case study of Hurricane Guillermo (1991) and of Hurricane Hernan (1996), both of which demonstrate TC development under the favorable environmental condition created by CAGW-induced surface cyclonic vorticity and the presence of easterly waves (Farfàn and Zehnder, 1997; Molinari et al., 2000).

Studies of CAGW approached to a new era after satellite scatterometer wind measurement became available. The spaceborne scatterometers are unique instruments among the majority of satellite remote sensors in their ability to retrieve near-surface wind speeds and directions over the oceans. These remotely sensed wind measurements have much greater spatial and temporal coverage than *in situ* observations, as well as many of global reanalysis wind products. The high-resolution scatterometer winds allow more detailed studies of CAGW, including the dynamical structure of jets, seasonal variation and wind climatology (Bourassa et al., 1999; Chelton et al., 2000a; Chelton et al., 2000b; Romero-Centeno et al., 2007). By directly separating CAGW events from the

background circulation, Holbach and Bourassa (2014) recently found that CAGW events are especially effective in triggering topical cyclogenesis when they interact with the monsoon trough, allowing CAGW-induced surface vorticity to be injected into large-scale existed TC-favorable environment. Indeed, Hurricane Patricia (2017), the strongest Pacific hurricane to make landfall in Mexico, appeared to be initialed from a precursor disturbance of CAGW strengthening event near TT (Avila, 2016; Rogers et al., 2017).

Although CAGW-induced low-level vorticity appears to play a role in tropical cyclogenesis over ENP, it is difficult to quantify its relationship with ENP TC activity. As pointed by many of studies and TC reports, easterly waves, breakdown of the Intertropical Convergence Zone (ITCZ), and the presence of the monsoon trough are also very important for ENP TC developments (Levine, 2012;). This suggests that ENP tropical cyclogenesis is a highly complex process, in which small-scale CAGW-induced vorticity and large-scale cyclonic vorticity features from background flow are both required. For this reason, there is a need to further understand the impact of CAGW on ENP TC activity and gain a better understanding of the dynamics behind the relationship between CAGW and ENP cyclogenesis.

1.2 Motivations and Objectives

As discussed in section 1.1.3, the relationship between ENP TC activity and CAGW variability is a new research area with remaining large uncertainties. Better understanding this relationship can potentially improve seasonal forecast skill of ENP TCs and

minimize the potential threats that TCs pose on Central America and the Hawaii islands. This is because understanding this relationship may be the key to resolve the controversy surrounding the role of ENSO in modulating TC activity over the EDR. Given that it has been well established that ENSO can modulate CAGW, the first objective of this study is to address the following questions:

1) Can ENSO modulate TC activity over the EDR through its impact on CAGW? If so, what is the underlying physical mechanism responsible for this modulation?

Advanced high-resolution satellite observations are required for accurate TC detections. As such, reliable TC observations are only available after 1970s when geostationary satellite observations were used to track TC development and paths. The relative short observational record hinders the understanding of how TC variability is controlled by climate modes. In this scenario, numerical models have always been very important tools in TC studies, both in the studies of TC relationships to climate variability and TC dynamics (Zhang and Wang, 2003; Patricola et al., 2015; Patricola et al., 2017; Walsh et al., 2015). To properly simulate TCs, the resolution of numerical models must be sufficiently fine, which makes global model simulations a major challenge given the current computational capability.

A remedy for this problem is the use of a regional modeling approach, where high-resolution simulations can be conducted in a limited domain over TC active regions. Recently, Patricola et al. (2015, 2017) configured a Weather Research and Forecasting

(WRF) model-based tropical channel model (TCM) to study how climate variability modulates TC activity. Although the TCM shows some success in reproducing observed characteristics of TC activity, major deficiencies and biases of the model are noted in simulating the spatial distributions of ENP TCs and associated regional-scale atmospheric circulations (Patricola et al., 2015).

To gain better understanding of ENP TCs variability, it is highly desirable to improve the TCM's skill in simulating ENP TCs. Thus, the second objective of the study is to address the following issues:

2) What causes the TCM's biases in simulating ENP TCs? And how can we reduce these biases to improve TC simulations in ENP?

With the improved TCM, we will be in a better position to investigate the impact of CAGW on ENP TCs. The third objective of the study is to conduct extensive TCM experiments to further quantify CAGW's impact on ENP TCs. In particular, we will investigate the following questions:

3) How much contribution can CAGW make to tropical cyclogenesis in ENP? How will ENP TCs activity be changed if CAGW is significantly reduced by eliminating the mountain gaps in the Sierra Madre?

This dissertation comprises five chapters. In Chapter II, we address the first set of research questions by conducting observational analysis. We perform a detailed analysis on the ENP TC spatial distribution in response to ENSO. We also investigate the underlying dynamical processes responsible for the ENSO-induced TC distribution

change in the region using reanalysis datasets. In Chapter III, we address the second set of research questions. A large set of model sensitivity experiments was conducted to determine the causes of TCM's biases and improve the TCM's skill in simulating ENP TCs. The improved model simulation was carefully validated against observations. In Chapter IV, we address the third set of scientific questions. We use the improved TCM to conduct idealized numerical experiments where the Sierra Madre mountain gaps were closed. Finally, in Chapter V, we summarize major findings of this dissertation research and discuss future research directions.

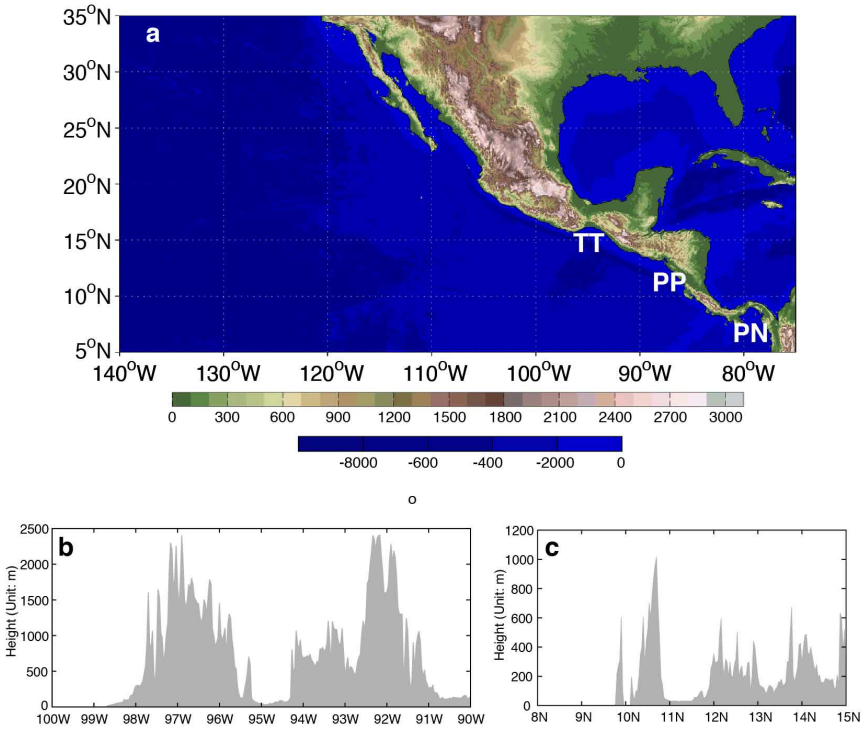

Figure 1.1. (a) Land topography (unit: m, top color bar) and ocean depth (unit: m, bottom color bar). Gaps at Tehuantepec, Papagayo, and Panama are marked as TT, PP and PN respectively. Cross sections of surface elevation at (b) TT along 16.5°N and (c) PP along 85°W.

CHAPTER II

INTRABASIN VARIABILITY OF EASTERN NORTH PACIFIC TROPICAL CYCLONES DURING ENSO REGULATED BY CENTRAL AMERICAN GAP WINDS*

2.1 Introduction

An understanding of the interannual variability of TCs and associated underlying physical mechanisms is crucial to improve seasonal TC forecast skill. On the interannual timescale, ENSO is the strongest climate mode of variability, and it significantly influences global atmospheric circulations and upper ocean heat content. The question of how this tropical climate variability has affected and will affect TCs has been the subject of intensive study. The earliest theoretical and observational studies of ENSO's impact on TC activities started in the late 1970s and early 1980s, the time when the intimate linkage between El Niño and Southern Oscillation was first recognized.

Gray (1984a) first documented that El Niño can substantially suppress TC activity over NA, resulting from increased upper-level zonal wind, while La Niña often induced above-normal TC activity. The greatly enhanced shear between upper-level and low-level wind made the environmental conditions unfavorable for TC development, thus, NA TC

activity tended to be significantly weaker during El Niño than La Niña. This showed us a possible method for estimating seasonal TC activity before the onset of boreal summer, since ENSO is noticeably predictable. In contrast to NA, ENSO tends to hardly change WNP TC occurrences, but significantly influence TC intensities, formation locations, and tracks (Chan 1985; Wang and Chan, 2002), where more TCs tended to initiate southeastward toward the central Pacific and had longer trajectories during El Niño than La Niña. The strengthened low-level shear vorticity due to anomalous equatorial westerlies during El Niño induced the enhanced TC activity in the southeast quadrant of the WNP, while the suppressed TC activity in the northwest quadrant is the net result of stronger than normal upper-level convergence and subtropical WNP high-pressure system (Wang and Chan, 2002).

The detailed studies of relationship between ENSO and ENP TCs were published much later than those in for the NA, probably due to the relatively limited threat that ENP TCs pose. In addition, from a statisticical point of view, the robustness of ENSO's modulation on ENP TC activity was even under great controversy (Gray and Sheaffer, 1991; Whitney and Hobgood, 1997; Ralph and Gough, 2009). Recent studies revealed that only TCs over the WDR of ENP had a significant positive correlation with the ENSO index, with more frequent and intense TCs during El Niño than La Niña (Collins and Mason, 2000; Ralph and Gough, 2009; Collins, 2007; Jien et al., 2015). Given that the anomalous SST fluctuations during ENSO were present over the Pacific coast of Central America, it raises the questions of why TCs over the EDR were insignificantly modulated

by ENSO? Since the majority of landfalling ENP TCs form in the EDR, more investigations are needed to understand the underlying dynamic mechanism to better protect lives and properties from the threat of TCs.

Of particular note is that ENSO's impact on WNP TCs is also non-uniformly distributed spatially. This southeast-northwest asymmetry suggests that ENSO's impact on ENP TCs may also have a similar east-west spatial variation. Many previous studies on ENSO's impact on ENP TCs used area-integrated measures, such as TC counts, TC days, accumulated cyclone energy (ACE; Bell et al., 2000) and power dissipation index (PDI; Emanuel; 2005), to relate ENP TC variability with ENSO indices (Ralph and Gough, 2009; Collins, 2007; Jien et al., 2015). Such measures cannot be applied to understand intrabasin TC variability, as they average out the opposite changes of TC activity in different parts of a TC basin. To address this issue, we will not simply analyze the area-integrated TC response to ENSO, but carry out analyses focusing on ENSO's impact on the spatial distribution of TCs within the ENP.

A previous study by Collins and Mason (2000) proposed 116°W as a boundary separating the EDR and WDR. In this study, we follow their convention and analyze TC variability in these two sub-basins in response to ENSO. However, unlike Collins and Mason (2000), our analyses do not include Central Pacific TCs between 180° and 140°W, because the focus of this study is on the eastern part of the ENP near the coastline where mountain influences are potentially greater. Thus, our WDR extends only to 140°W, rather than to the dateline (Collins and Mason, 2000).

The organization of this chapter is as follows. Section 2 introduces the datasets, the variables that represent environmental favorability of tropical cyclogenesis, and the analysis methodologies. Section 3 illustrates the general spatial characteristics of ENP TC responses to ENSO events, and validates the similarities and differences with conventional conclusions. Section 4 further examines the relative importance that each environmental factor contributes to this spatial-variation of TC responses, and its relationship with CAGW is analyzed in section 5. Finally, section 6 summarizes the preliminary results and discusses an additional perspective from the synoptic timescale.

2.2 Data and analysis method

In this chapter, all composite and diagnostic analyses focus on the period from June 1st through November 30th (hereafter 'hurricane season'), which accounts for more than 95% (792 out of 832) of the total number of TCs during 1970-2015. Note that our analysis period is slightly different from the ENP hurricane season defined by the National Hurricane Center (NHC), which runs from May 15th through November 30th. Since the number of TCs during our research period covers more than 95% of total TC number in the region, it is unlikely that the results are sensitive to this minor difference in hurricane season definition.

We use the hurricane season averaged Niño3.4 index derived from the detrended HadISST sea surface temperature dataset of the Met Office Hadley Centre (Rayner et al., 2003) to define ENSO events. The seasonal mean values above the 75th (below the 25th)

percentile are chosen as El Niño (La Niña) hurricane seasons. During the period from 1970-2015, 13 El Niño hurricane seasons (1972, 1976, 1982, 1986, 1987, 1991, 1994, 1997, 2002, 2004, 2006, 2009, 2015) and 11 La Niña hurricane seasons (1970, 1971, 1973, 1975, 1988, 1998, 1999, 2000, 2007, 2010, 2011) are identified (Figure 2.2), which is in general agreement with previous studies (Bove et al., 1998; Jien et al., 2015; Camargo et al., 2007).

The World Meteorological Organization (WMO) subset of International Best Track Archive for Climate Stewardship (IBTrACS-WMO; Knapp et al., 2010) dataset v03r09 is used to calculate genesis density and track density field. The IBTrACS data works directly with all the Regional Specialized Meteorological Centers and other international centers to create a global merged best track dataset to overcome data availability issues. IBTrACS-WMO has been endorsed as an official archive of TC information for public use.

In order to better resolve spatial variability within the ENP basin, track density on a yearly basis is defined as the total number of 6-hourly TC central locations within each 2° (latitude) ×2° (longitude) square box during each hurricane season. To reduce noise and better capture principal anomaly patterns of TC locations, track density is then smoothed by averaging the surrounding eight points. Genesis density has a similar definition, except only the number of tropical cyclogenesis events (first record of TC that develops to at least a tropical depression) in each 2°×2° square box are counted. Genesis density is also smoothed in the same way as track density.

In addition to the Student's t-test, a bootstrap technique (Efron and Tibshirani, 1991) is also applied to determine the statistical significance of both genesis and track density. El Niño composites are constructed using 13 randomly chosen years from a total of 46 years. This re-sample process is then repeated 10,000 times to obtain a 95% and 90% confidence interval. The same process is also applied for the La Niña composite anomaly, but using 11 randomly sampled years out of 46-year climatology.

To reveal the underlying physical mechanism of intrabasin ENP TC variability, the National Centers for Environmental Prediction (NCEP) Climate Forecast System Reanalysis (CFSR; Saha et al., 2010) and its extension, the NCEP Climate Forecast System version 2 (CFSv2; Saha et al., 2014), are used for TC environmental condition analyses. The CFSR is a reanalysis product from quasi-global fully coupled atmosphere-ocean-land surface-sea ice model assimilated with observations. The horizontal resolution of spectral atmospheric model is T382 (~38km) with 64 sigma-pressure hybrid levels. For scientific research purpose, the atmospheric outputs are interpolated to 37 vertical pressure levels with different horizontal resolutions available. The CFSR covers a 32-year period from January 1979 to March 2011, and was then upgraded to CFSv2 to extend data availability. The CFSv2 uses improved forecast model components as well as data assimilation system, and the real-time analysis can be accessed with finer horizontal resolution (spectral T574, ~27km). To better represent TC environmental conditions, we use 0.5°×0.5° 6-hourly rather than monthly mean data. 11 El Niño (1982, 1986, 1987, 1991, 1994, 1997, 2002, 2004, 2006, 2009, 2015) and 7 La

Niña (1988, 1998, 1999, 2000, 2007, 2010, 2011) hurricane seasons are identified during the entire 37-year period from 1979 to 2015 and are used to diagnose TC environmental condition changes during El Niño and La Niña events.

The environmental favorability for tropical cyclogenesis is assessed by analyzing the genesis potential index (GPI; Emanuel and Nolan, 2004), which is defined as:

$$\text{GPI} = /10^5\eta/^{3/2}(\frac{H}{50})^3(\frac{V_{pot}}{70})^3(1+0.1V_{shear})^{-1} \quad (1)$$

where η is absolute vorticity at 850 hPa (s^{-1}), H is relative humidity at 700 hPa (%), V_{shear} is the magnitude of vertical wind shear between 850 and 200 hPa (m s^{-1}). V_{pot} is hurricane maximum potential intensity (PI; m s^{-1}; Emanuel, 1995; Bister and Emanuel 1998, 2002;), defined as:

$$V^2{}_{pot} = C_P(T_S - T_O)\frac{T_S}{T_O}\frac{C_k}{C_D}(\ln\theta^*{}_s - \ln\theta_s) \quad (2)$$

where T_S is SST (K) and T_o is outflow air temperature at tropopause (K). C_P is heat capacity of air, $C_k$and C_d are the surface exchange coefficients of enthalpy and the drag coefficient (dimensionless), respectively. $\theta^*{}_s$ and θ_s are surface saturation equivalent potential temperature and boundary layer equivalent potential temperature (K). The application of PI theory is discussed online (http://wind.mit.edu/~emanuel/holem/node3.html). FORTRAN and MATLAB subroutines are available online (ftp://texmex.mit.edu/pub/emanuel/TCMAX/). To estimate the primary contributions that lead to the ENSO-induced GPI anomalies, the GPI is also recalculated by interannually varying just one term while setting the other

three terms to values of the long-term climatology (Camargo et al., 2007; Patricola et al, 2014, 2016).

The ocean surface wind vector is derived from the National Aeronautics and Space Administration's (NASA's) Quick Scatterometer (QuikSCAT) Version-4 (V4) wind product (Ricciardulli and Wentz, 2015). This dataset has horizontal resolution of 0.25°×0.25°, based on an improved Ku-band Geophysical Model Function (GMF) to optimize wind speed retrievals, especially in high wind speed areas. QuikSCAT ocean surface wind is available from 19 July 1999 to 23 November 2009, and is widely used in CAGW observational studies (Romero-Centeno et al., 2007; Holbach and Bourassa, 2014; Brennan et al., 2000).

By vector identity, vertically integrated horizontal moisture flux can be written as:

$$\frac{1}{g}\int_{70000Pa}^{50000Pa} q\boldsymbol{V}_h\, dp \quad \text{and} \quad \boldsymbol{V}_h = u\boldsymbol{i} + v\boldsymbol{j} \tag{3}$$

where q is specific humidity (kg kg^{-1}), u and v represent the standard horizontal zonal and meridional wind components (m s^{-1}), p is air pressure (Pa), and g is gravitational acceleration (m s^{-2}). Therefore, $q\boldsymbol{V}$ has the units of kg kg^{-1} m s^{-1}. Since the units of dp/g, Pa/(m s^{-2}) can equally convert to kg m^{-2}, the term 'mass weighted' is able to use for vertical integration. The vertically-integrated moisture flux can be calculated in units of kg m^{-1} s^{-1}. To convert to a column of water, we assume the water vapor has a constant density of 10^3 kg m^{-3}, so the units of the vertically integrated moisture flux can be written as mm m s^{-1}.

2.3 Observed intrabasin TC variability

We first made a composite of TC genesis location and track density for all El Niño and La Niña events during the period from 1970 to 2015 and compared the results to the climatological genesis location and track density for this period. 13 El Niño and 11 La Niña hurricane seasons were identified based on the 75th and the 25th percentiles of the Niño3.4 index (Figure 2.2).

Figure 2.3 shows the difference in TC genesis and track density (defined in Section 2.2) averaged over the 13 El Niño and 11 La Niña events relative to the 46-year (1970-2015) climatology. It is evident that, despite the marked increase of TC activity in the WDR that is consistent with previous studies (Collins, 2007; Jien et al., 2015), El Niño suppresses TCs in the EDR, as in the Caribbean and Gulf of Mexico. Both TC genesis (Figure 2.3a) and track density (Figure 2.3b) in the ENP exhibit a westward shift during El Niño, with a prevailing decrease near the Pacific coast of Central America and the western side of the Sierra Madre Mountains. We examined the robustness of this westward shift pattern by performing a Student's t-test and a bootstrap statistical test (Figure 2.4), as well as by performing a regression analysis where both TC genesis and track density were regressed onto the hurricane season mean Niño3.4 index (Figure 2.4). The fact that the response pattern survives this statistical scrutiny gives us the confidence that El Niño can, in a statistical sense, cause a decrease (increase) in TC activity in the EDR (WDR) of the ENP.

Similar spatial variability of ENP TCs, but opposite in sign, occurs during La Niña, with an expected decrease of TC activity in the WDR and an increase in the EDR (Figures 2.3c, d). These findings point to an east-west spatial pattern in the ENP TC response to ENSO, which we refer to as intrabasin TC variability. The average TC frequency change caused by the intrabasin variability in the nearshore area is comparable to the well-known ENSO-induced TC change in the North Atlantic. Within 550 km off the west coast of Central America, the distance within which TC centers can generate observable rainfall at coastal stations (Englehart and Douglas, 2001), the TC frequency decreases by ~22.4% (increases by ~16.2%) during El Niño (La Niña). These changes are similar in magnitude to those observed in the Caribbean and Atlantic during ENSO (Gray, 1984a). This ENSO-related ENP TC activity change in the nearshore area is also consistent with Gutzler et al. (2013).

2.4 Environmental factors that control intrabasin variability

We next examine whether this intrabasin TC variability is consistent with our current understanding of the dynamic processes controlling TC variations by analyzing GPI. GPI is calculated based on daily-averaged NCEP CFSR (1979-2010) and CFSv2 (2011-2015) datasets. We chose CFSR and CFSv2 because they produce a more realistic representation of fine-scale atmospheric circulation features over the EDR than other reanalysis products (Alexander et al., 2012). However, owing to the shorter record length of CFSR and CFSv2 data, only 11 El Niño and 7 La Niña hurricane seasons were

identified during the 1979-2015 period. But, the TC activity response to El Niño and La Niña is insensitive to changes in the record length (Figure 2.5), providing justification for using the shorter period composite in the following diagnostic analyses.

GPI is widely used to examine environmental favorability for TC genesis, and the seasonal cycle of GPI averaged over the ENP main development region (MDR; 8°-20°N, 140°W to the North American coast; see gray box in Figure 2.6c) indeed corresponds well with the observed number of TCs (Figure 2.6a). The correlation between MDR-averaged hurricane season mean GPI and observed ENP TC frequency during 1979-2015 has a value of 0.59 (p-value < 0.01 based on the Student's t-test; Figure 2.6b), indicating that GPI describes the basin-wide ENP TC variability well (Camargo et al., 2007; Zhao and Raga, 2015). Consistent with the observed intrabasin TC variability shown in Figure 2.3, GPI anomalies during El Niño display an east-west pattern with increased GPI values in the WDR and decreased GPI values in much of the EDR (Figure 2.7a). During La Niña, GPI anomalies are also characterized a similar spatial pattern, but with the opposite sign (Figure 2.7f).

To identify the dominant atmospheric processes that drive intrabasin TC variability, we further evaluated the relative importance of various atmospheric parameters that determine environmental favorability for TCs. Over much of the ENP, the El Niño-induced changes in vertical wind shear and hurricane maximum potential intensity provide more favorable conditions for tropical cyclogenesis (Figures 2.7d and f), consistent with a previous study (Camargo et al., 2008). However, in the EDR, the

changes in vorticity and relative humidity create less favorable conditions for TC genesis (Figures 2.7b and c). The negative GPI anomaly due to changes in vorticity is particularly important, and dominates over that due to humidity changes near the coastal area. Combined, these negative GPI anomalies overpower the positive GPI anomalies associated with changes in vertical wind shear and hurricane maximum potential intensity, resulting in a net negative GPI anomaly in the near coastal region (Figure 2.7a). As expected, GPI anomalies during La Niña show nearly the same patterns, but opposite in sign, and the positive GPI anomalies near the Pacific coast are again attributed to the vorticity and relative humidity changes (Figures 2.7g and h). Of particular note is that both the low-level vorticity-induced and mid-tropospheric moisture-induced negative (positive) GPI anomalies during El Niño (La Niña) show a well-defined structure extending westward from the Sierra Madre topographic gap areas, especially near the Isthmus of Tehuantepec (TT; Figure 1.1b) and Gulf of Papagayo (PP; Figure 1.1c). This prompted us to probe further into the connection between the topographically-locked features and the ENP intrabasin TC variability during El Niño (La Niña), particularly the TC suppression (enhancement) in the EDR.

2.5 The role of CAGW in the intrabasin variability

The Sierra Madre blocks large-scale, low-level flow from North America and the Caribbean towards the ENP. There are three major narrow topographic gaps at TT, PP and Panama (PN), and the depth of these gaps can approach ~1000 meters vertically

(Figure 1.1). During boreal winter (November through March), intermittent winter storms from the Gulf of Mexico and more steady trade winds force strong wind jets penetrating through these narrow gaps and into the ENP, generating the CAGW (Steenburgh et al., 1998; Chelton et al., 2000a; Romero-Centeno et al., 2007). Although the CAGW at TT and PP are strongest during boreal winter (Chelton et al., 2000a; Romero-Centeno et al., 2007), they are also characterized by a secondary peak during July-August caused by the westward intensification of the Azores-Bermuda high pressure system (Romero-Centeno et al., 2007).

Figure 2.8 shows the 1999-2009 hurricane season mean ocean surface winds derived from National Aeronautics and Space Administration's (NASA's) QuikSCAT wind product, along with the corresponding SST. Both CAGW at TT and PP are clearly visible in the climatology, but the northerly TT jet is stronger and more effectively cools local SSTs. The CAGW at TT follows anticyclonic arcs downwind from the coast. In contrast, the CAGW at PP is more zonal because of the orientation of topographic gaps and the influence of steady trade winds. ENSO modulates the strength of the CAGW (Alexander et al., 2012; Romero-Centeno et al., 2003), with intensified winds observed at both TT and PP during El Niño, due to an increased frequency of cold frontal intrusions and a southward shift of the ITCZ.

Because of its narrow structure and strength, the CAGW plays a dominant role in determining low-level relative vorticity in the EDR, which is a key factor in influencing environmental favorability for tropical cyclogenesis. Figures 2.9a, b, and c show the

climatology, and the El Niño- and La Niña-induced anomalies of 925 hPa relative vorticity in the ENP, respectively, along with the 925 hPa wind vector. It is evident that the stronger horizontal wind shear associated with the CAGW at TT and PP generates two relative vorticity dipoles in the EDR (Figure 2.9a). The negative pole near TT is particularly pronounced, because the anticyclonic curvature of the jet path after it leaves the Gulf of TT strengthens the existing anticyclonic relative vorticity.

During El Niño, the intensified CAGW at both PP and TT (Figure 2.10a) contributes to the anticyclonic (negative) relative vorticity anomalies north of 10°N, especially between TT and PP and along the western flank of the TT jet (Figure 2.9b), resulting in a less favorable environment for tropical cyclogenesis (Figure 2.7b) and TC suppression in the EDR (Landsea, 2000; Charney and Eliassen, 1964; Emanuel, 1986; Montgomery and Enagonio, 1998; Gray, 1979). The southern flank of the PP jet, on the other hand, is characterized by a cyclonic (positive) relative vorticity anomaly. During La Niña, however, the reduced CAGW at TT and PP (Figure 2.10b) generates positive relative vorticity anomalies, which make the environment more favorable for TC genesis in the EDR (Figures 2.9c, 2.7h). These changes in the relative vorticity are remarkably consistent with observed negative (positive) genesis density and track density anomalies in the EDR during El Niño (La Niña). We thus conclude that the CAGW-induced low-level relative vorticity change during ENSO serves as a primary cause for the ENP TC intrabasin variability, particularly in the EDR.

A secondary but important factor contributing to TC variability in the EDR is the mid-tropospheric moisture change. Figures 2.9d, e, and f show climatological 700 hPa – 500 hPa integrated specific humidity, overlaid by the integrated moisture flux, and the corresponding anomalies during El Niño and La Niña. At tropospheric mid-levels, above the extent of the CAGW, the integrated specific humidity over the EDR is reduced during El Niño (Figure 2.9e) and increased during La Niña (Figure 2.9f). The reduced (increased) mid-tropospheric moisture, during El Niño (La Niña) further contributes to the negative (positive) GPI anomaly and provides another source to suppress (enhance) TC activity in the EDR (Collins, 2007; Gray 1979, 1968). Further investigation is needed to understand the underlying dynamic mechanism responsible for the moisture changes in the region.

2.6 Summary and discussion

This chapter provides a new perspective on the impact of ENSO on ENP TC activity. It suggests that the previous view of increased (decreased) basin-wide ENP TC activity during El Niño (La Niña) caused by changes in vertical wind shear, SST, and mid-tropospheric relative humidity is incomplete. The ENP TC response to ENSO is characterized by intrabasin variability, with enhanced TC activity confined to only the WDR and reduced TC activity in the EDR during El Niño, and the opposite during La Niña. Furthermore, this study identifies a topographically locked feature – CAGW– as a primary player in regulating TC activity in the EDR through low-level relative vorticity changes. As all TCs that make landfall onto the Pacific coast of Central America and

Mexico form in the EDR, the results presented here have important implications for improving seasonal forecast skill of ENP TCs and their impacts. It points to the necessity of properly resolving and representing the CAGW and its response to ENSO in TC forecast models.

We note that the overall reduction of TC activity over the EDR in response to El Niño does not exclude occurrences of individual extreme hurricanes in the region during El Niño. Indeed, Hurricane Patricia in 2015 and Hurricane Pauline in 1997, both among the strongest hurricanes to make landfall over Mexico, occurred during strong El Niño years. Individual hurricane genesis can be initiated by short-lived synoptic events that may not contribute significantly to the mean environment for TC genesis. Hurricane Patricia, for example, appeared to be initiated by a synoptic-scale CAGW strengthening event near TT that provided an injection of cyclonic relative vorticity on the cyclonic shear side and spurred the formation of the initial tropical depression (Kimberlain et al., 2016). These types of synoptic CAGW events are especially effective in triggering tropical cyclogenesis when they interact with the monsoon trough (Holbach and Bourassa, 2014). Understanding synoptic CAGW events as a mechanism of tropical cyclogenesis is an active research area, and more studies are clearly needed to elucidate the underlying dynamical processes and the distinction between their roles in synoptic versus seasonal and longer timescales.

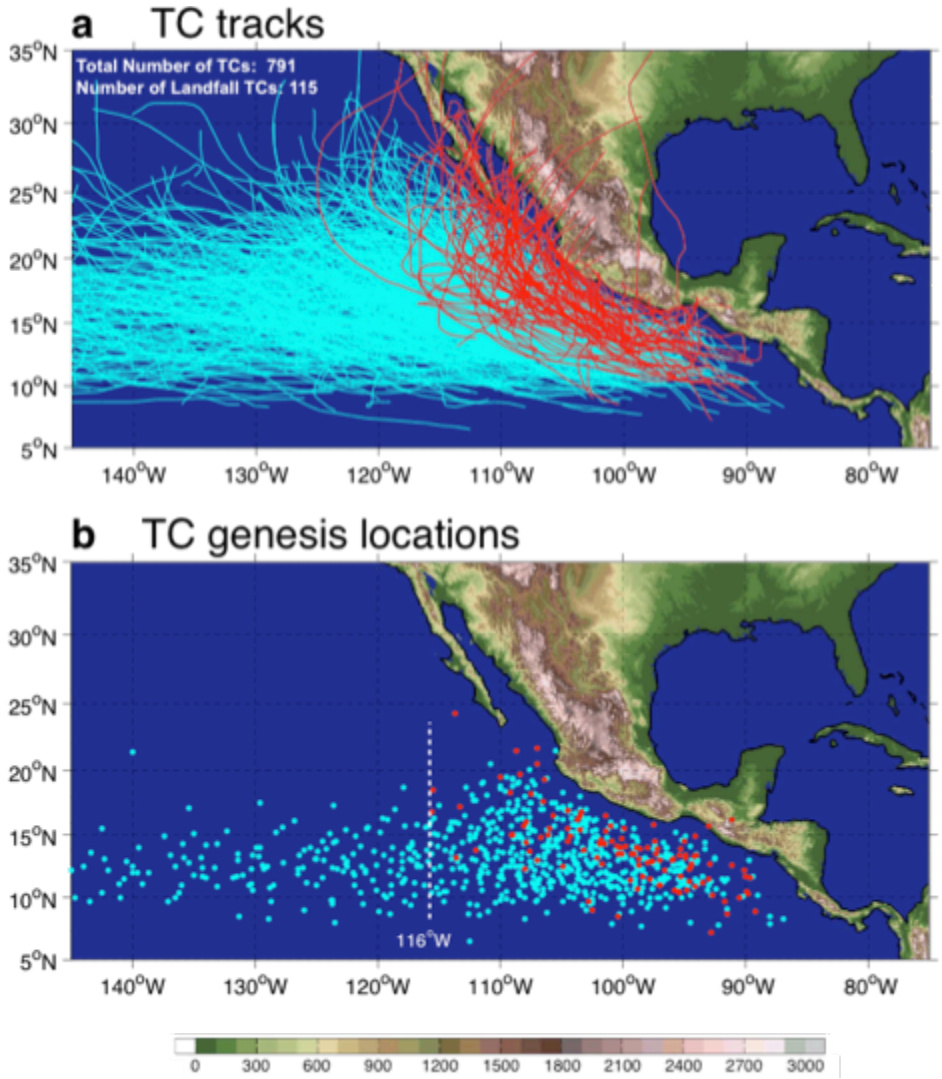

Figure 2.1 Distributions of observed a) TC tracks and b) TC genesis locations over the ENP during 1970 to 2015 hurricane seasons. Red curves and dots indicate TCs that made landfall onto the Pacific coast of Central America and Mexico. Land topography (unit: m) is shaded green-brown.

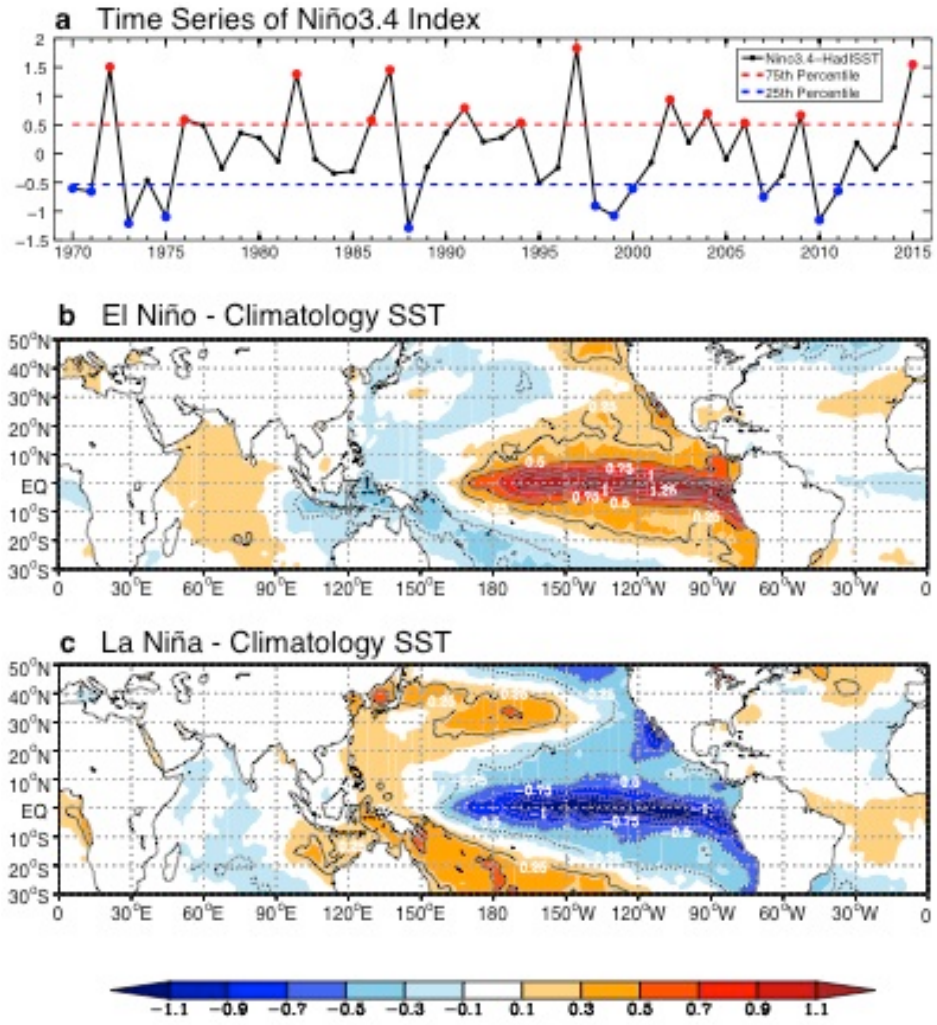

Figure 2.2 a) Time series of the hurricane season (June -November) mean Niño3.4 index (black curve with dots), with the 75th (red dash) and the 25th percentile (blue dash) values. El Niño and La Niña events are indicated in red dots and blue dots respectively. Difference in hurricane season mean SST from the b) El Niño hurricane seasons c) La Niña hurricane seasons composite minus climatology (contour interval is 0.25 °C).

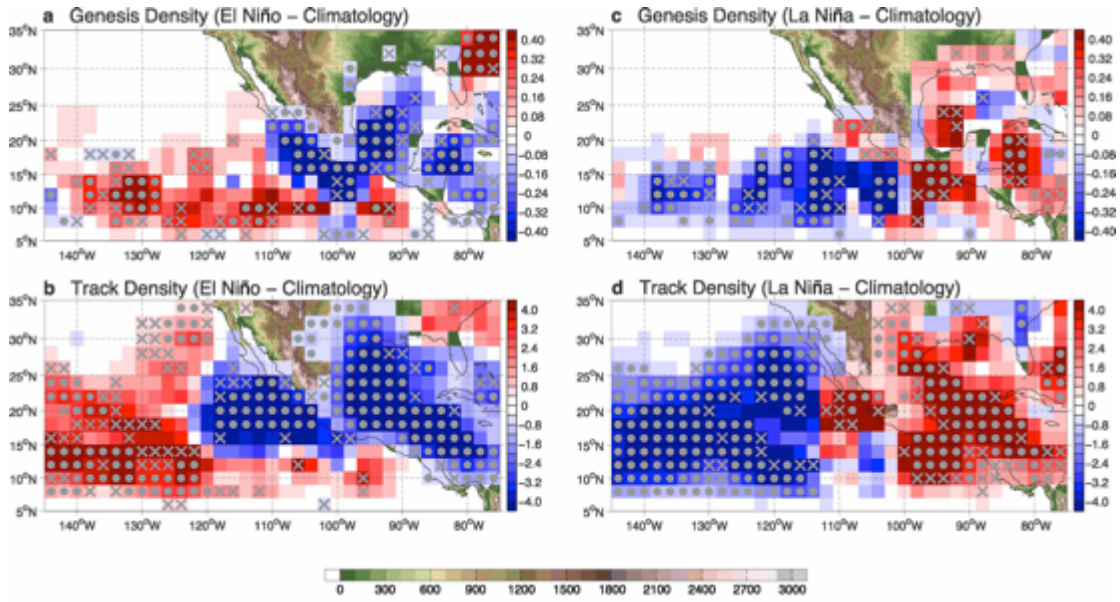

Figure 2.3 The El Niño hurricane seasons composite minus climatology difference in a) TC genesis density (unit: TCs per 10 seasons), and b) TC track density (unit: TCs per 10 seasons). c), d) are same as a), b) but for the difference from the La Niña hurricane seasons composite minus climatology. Gray dots (crosses) denote statistical confidence at the 95% (90%) level. Statistical significance test is performed based on the two-sample t-test. Land topography (unit: m) is shaded green-brown.

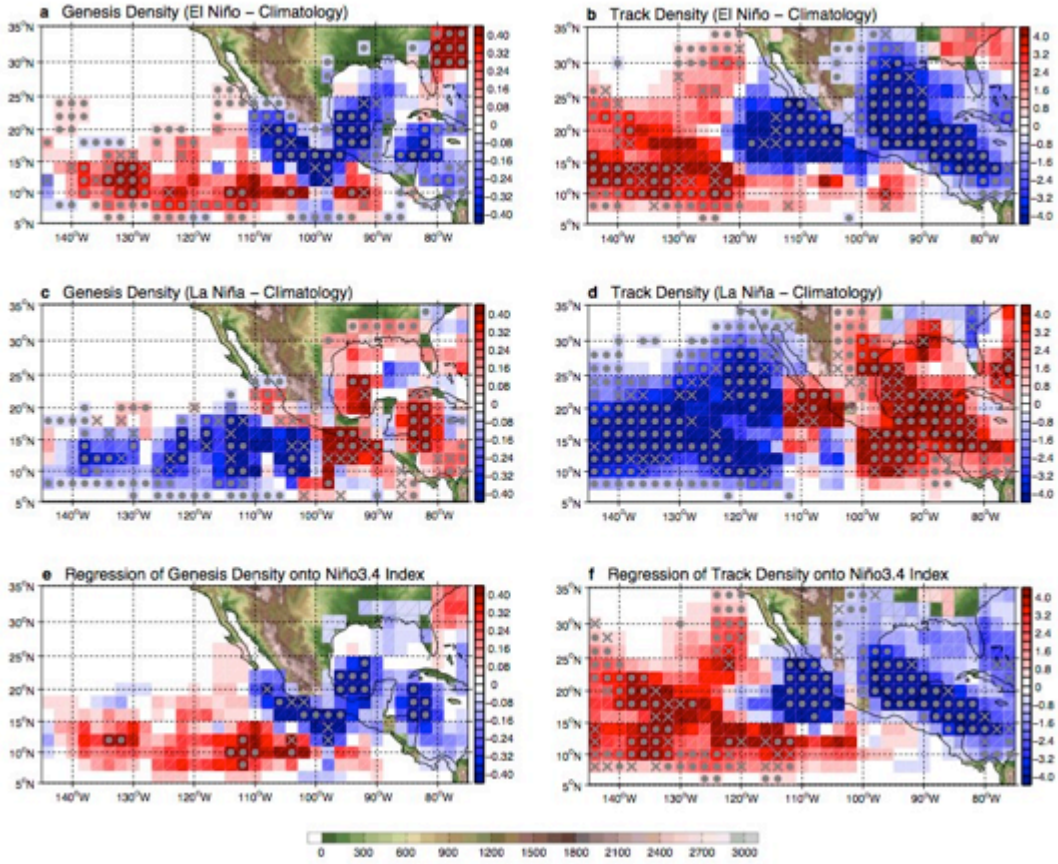

Figure 2.4 The El Niño hurricane seasons composite minus climatology difference in a) TC genesis density anomaly (unit: TCs per 10 seasons), and b) TC track density anomaly (unit: TCs per 10 seasons) similar to Figure 2.3a) and b), except using a bootstrap technique to determine statistical confidence level. c), d) are similar, but for the La Niña hurricane seasons composite minus climatology. Regression of e) TC genesis density and f) TC track density onto the hurricane season averaged Niño3.4 index. Gray dots (crosses) denote statistical confidence at the 95% (90%) level based on the two-sample t-test. Land topography (unit: m) is shaded green-brown.

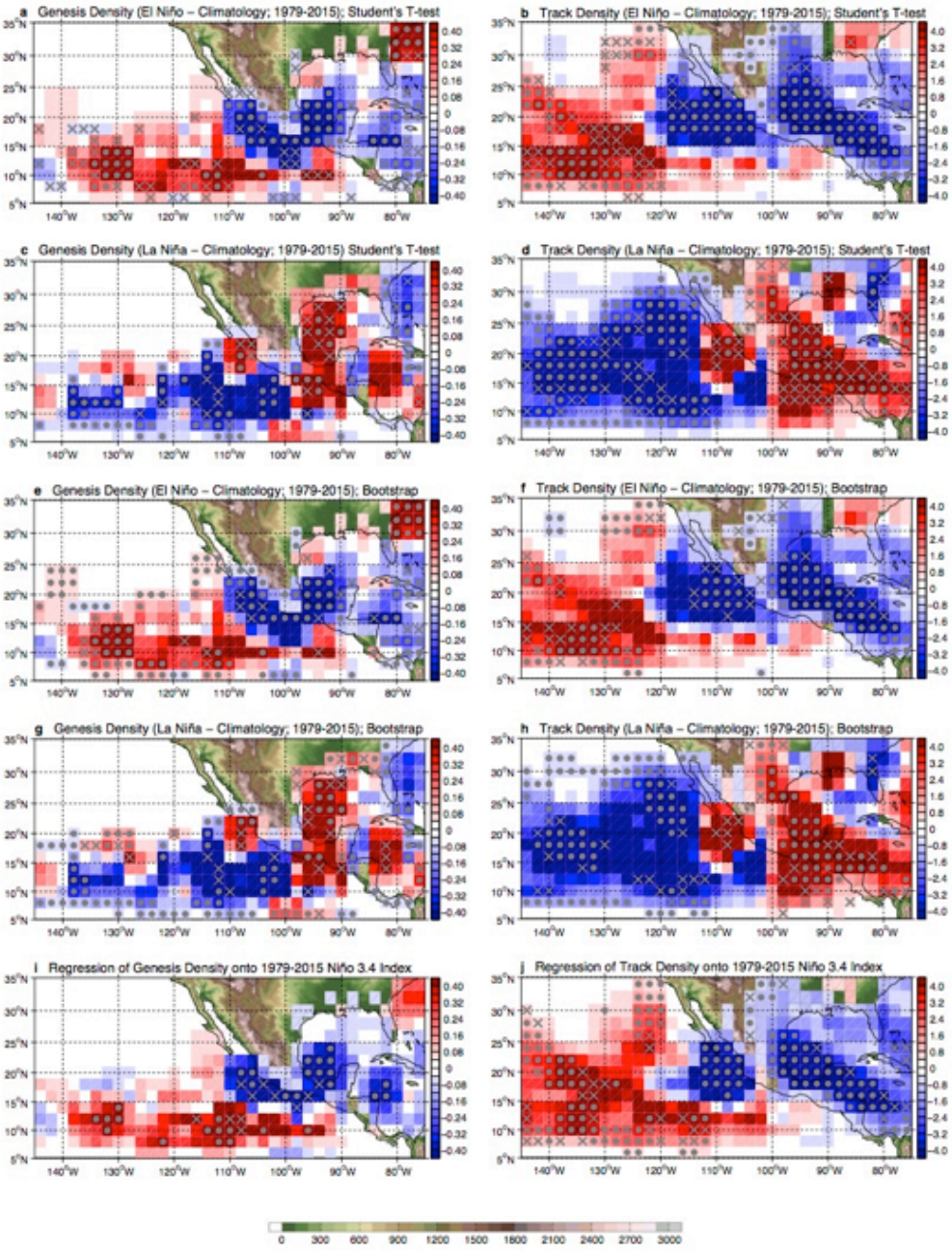

Figure 2.5 The composite of El Niño hurricane seasons during 1979-2015 minus 37-year (1979-2015) climatology difference in a) TC genesis density (unit: TCs per 10 seasons), and b) TC track density (unit: TCs per 10 seasons), applied by the two-sample t-test to determine statistical confidence level. c), d) are similar, but for the La Niña hurricane seasons composite minus 37-year climatology. e), f), g) and h) are same as a), b) ,c), and d) but using bootstrap technique to determine statistical confidence level. Regression of i) TC genesis density and j) TC track density onto the hurricane season averaged Niño3.4 index during 1979-2015. Gray dots (crosses) denote statistical confidence at the 95% (90%) level. Land topography (unit: m) is shaded green-brown.

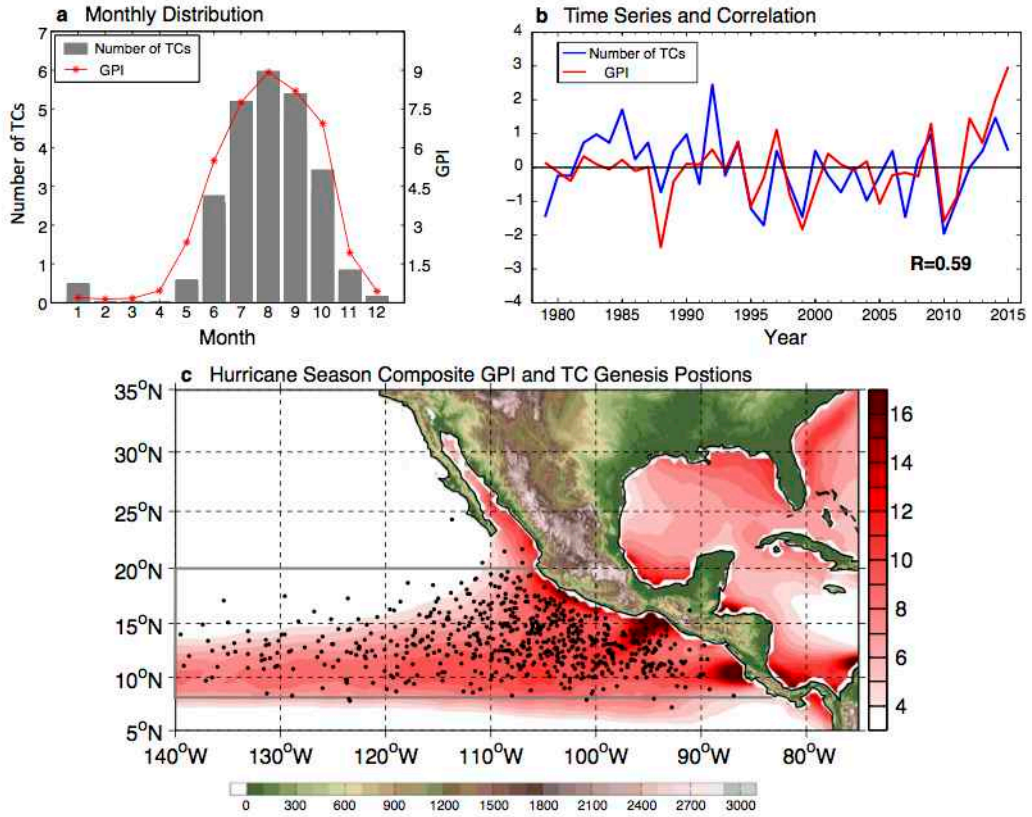

Figure 2.6 a) Seasonal cycle of genesis potential index (GPI, unitless, red curve with dots) averaged over the ENP TC main development region (MDR; 8°N-20°N, 85°W-American coast, see gray box in panel c)) and monthly averaged number of ENP TCs (gray bar) from January to December. b) Normalized time series of hurricane season mean GPI averaged within MDR (red curve) and number of ENP TCs (blue curve). c) Climatological hurricane season mean GPI (shading) and all of TC genesis locations (black dots) during 1979-2015 hurricane seasons. Land topography (unit: m) is shaded green-brown.

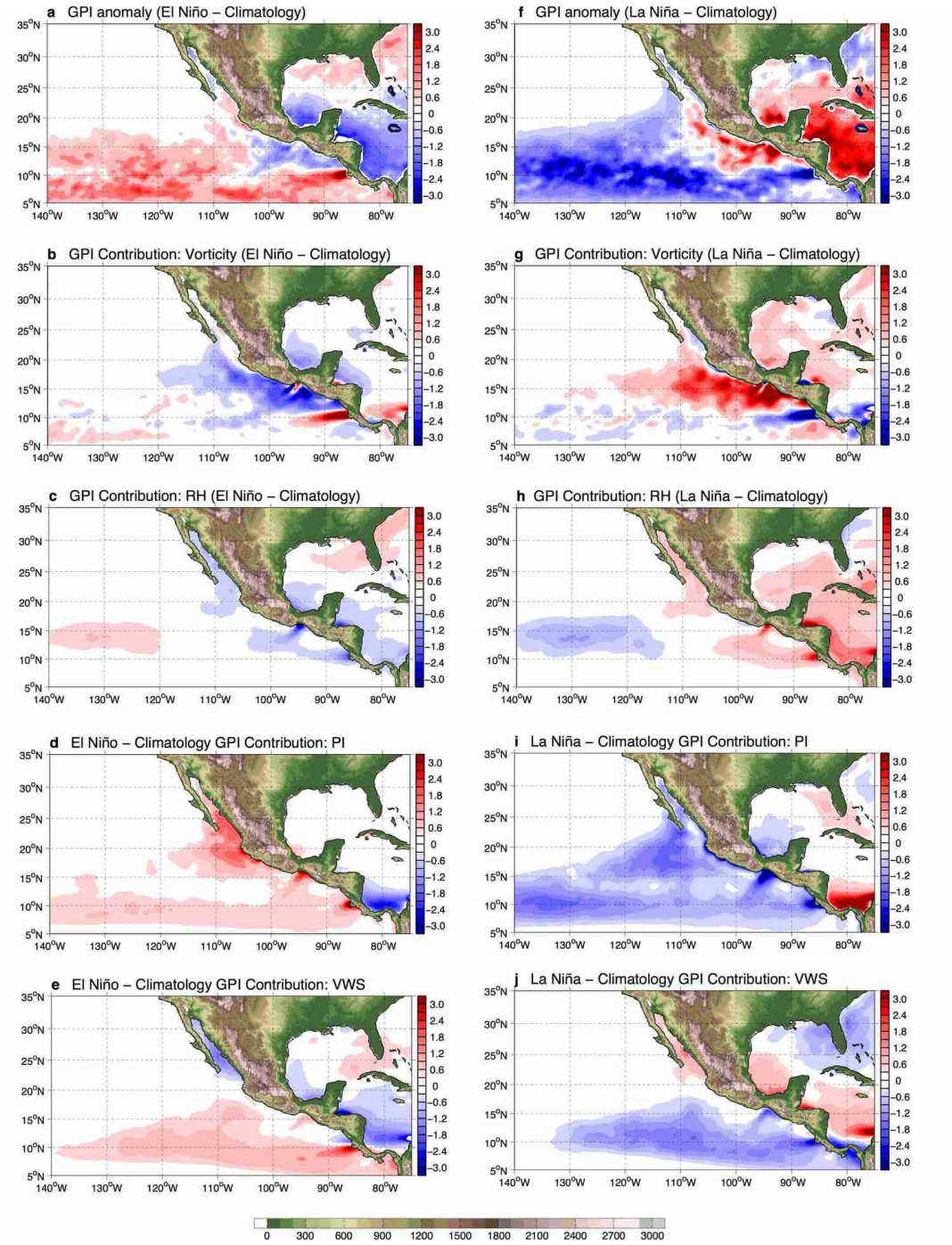

Figure 2.7 a) The El Niño hurricane seasons composite minus climatology difference in genesis potential index (GPI, unitless) and difference of GPI (unitless) calculated by varying just b) vorticity, c) relative humidity, d) potential intensity and e) vertical wind shearwhile setting the other three terms to values of the climatology. f), g), h) i), and j)are similar, but for the GPI anomaly from the La Niña hurricane seasons composite minus climatology. Positive indicates environmental conditions are more favorable for TC genesis, and vice versa. Land topography (unit: m) is shaded green-brown.

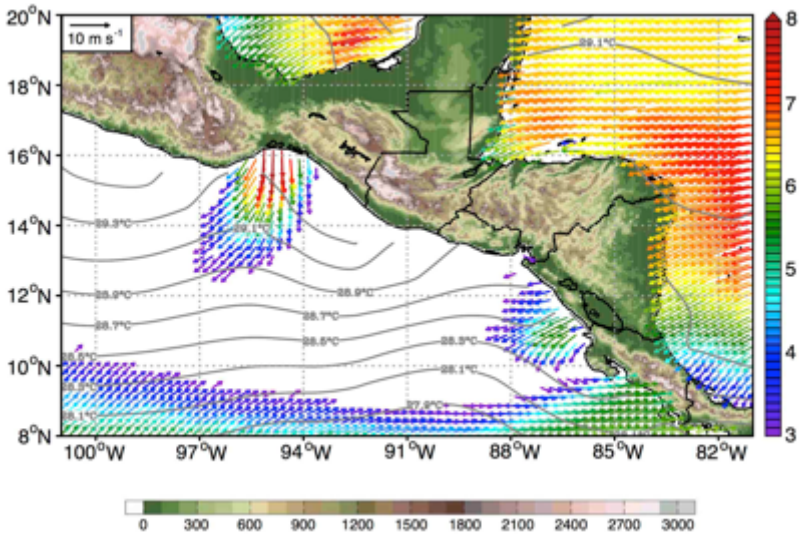

Figure 2.8 Climatological hurricane season averaged ocean surface wind (vectors, unit: m s^{-1}) is derived from QuikSCAT V4 wind product. Colors of vectors indicate wind speeds as shown in the right colorbar, only plotting the region where the wind speed is higher than 3 m s^{-1}. Climatological hurricane season averaged SST (contours, unit: °C) is plotted at intervals of 0.2°C. Land topography (unit: m) is shaded green-brown.

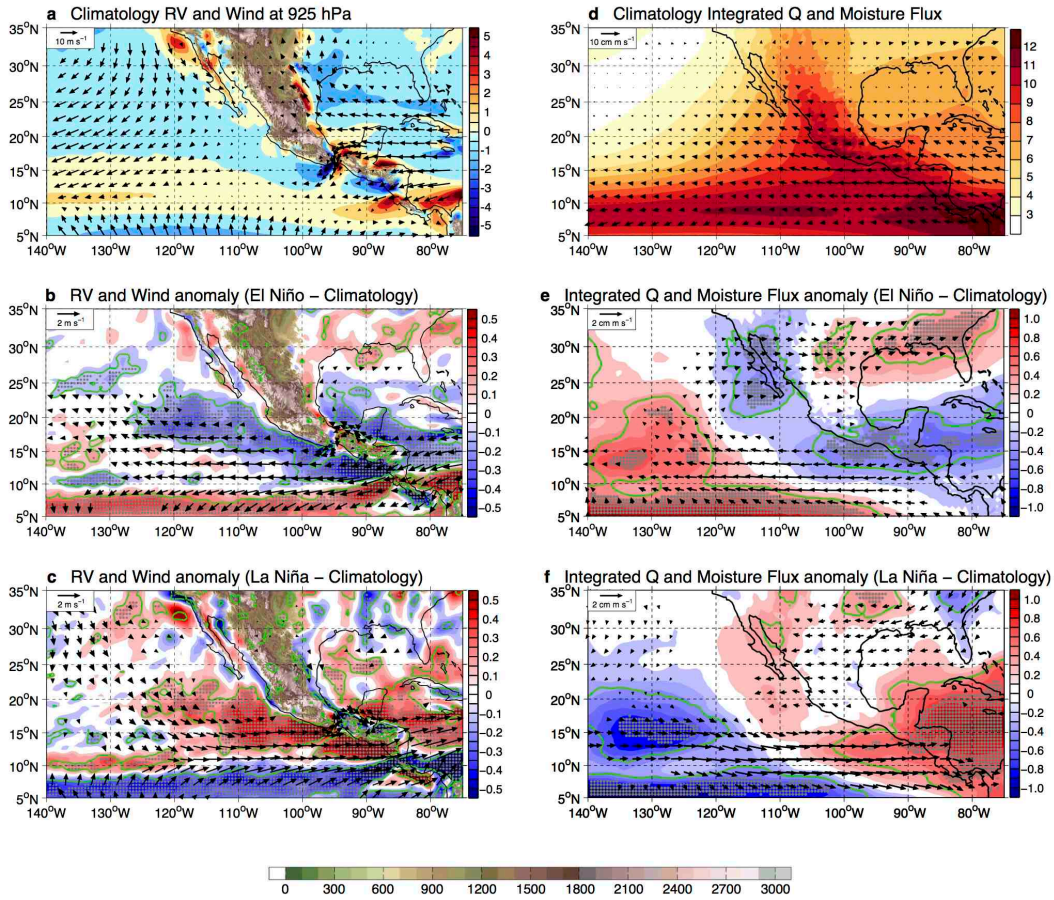

Figure 2.9 a) Climatological, b) the El Niño hurricane seasons and c) the La Niña hurricane seasons composite minus climatology difference in relative vorticity (*rv*; shadings, unit: 10^{-5} s^{-1}) and wind vectors (unit: m s^{-1}) at 925 hPa. d) Climatological, e) the El Niño hurricane seasons and f) the La Niña hurricane seasons composite minus climatology difference in 700 hPa through 500 hPa integrated specific humidity (*q*; shadings, unit: mm) and moisture flux (*qV*; vectors, unit: cm m s^{-1}). Gray dots (green contours) highlight the statistical confidence at the 95% (90%) level. All vector anomalies are plotted only where the confidence level is above 95%. Statistical significance test is performed based on the two-sample t-test. Land topography (unit: m) at atmospheric pressure level is shaded green-brown.

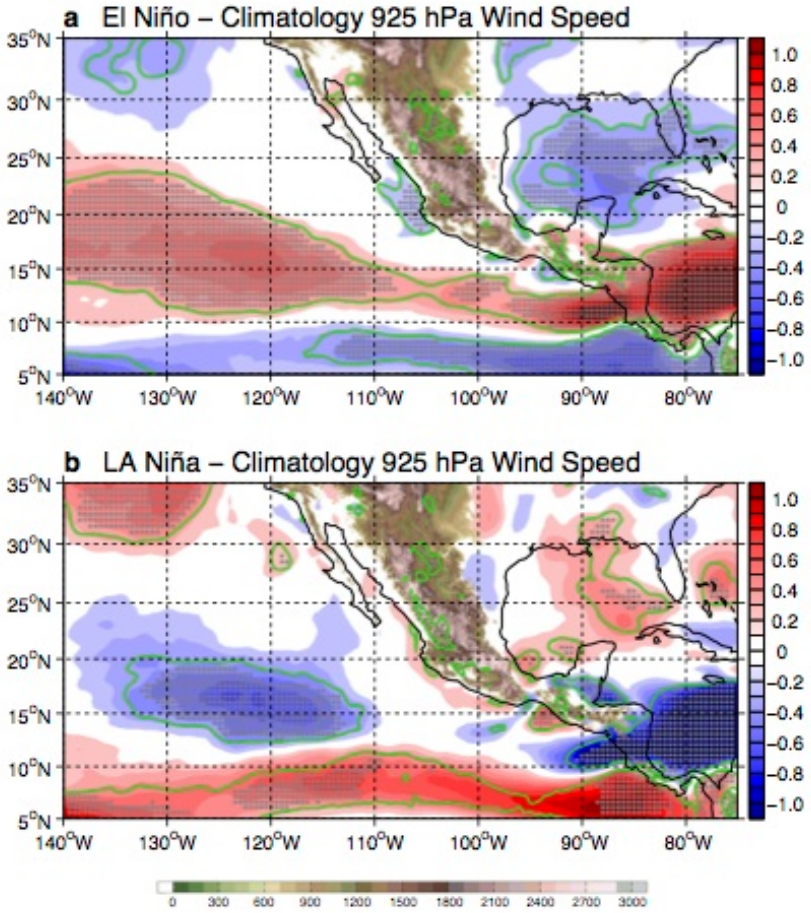

Figure 2.10 a) The El Niño and b) the La Niña hurricane seasons composite minus climatology difference in mean scalar wind speed at 925 hPa (unit: m s^{-1}). Gray dots (green contours) highlight the statistical confidence at the 95% (90%) level based on the two-sample t-test. Land topography (unit: m) at atmospheric pressure level is shaded green-brown.

CHAPTER III

EASTERN NORTH PACIFIC TROPICAL CYCLONE SIMULATION BY TROPICAL CHANNEL MODEL

3.1 Introduction

In addition to the ENSO-induced ENP intrabasin TC variability due to anomalous CAGW activity, synoptic-scale CAGW variability can also modulate individual ENP TCs. By directly categorizing CAGW events by their wind velocities, Holbach and Bourassa (2014) documented that CAGW-induced vorticity perturbations can contribute to the development of ENP TC initial disturbances and that this contribution is more effective when CAGW events interact with the monsoon trough. Indeed, the formation of Hurricane Celia (2004), Hurricane John (2006), and Hurricane Patricia (2015) can be traced back to CAGW events based on satellite observations (Holbach and Bourassa, 2014; Kimberlain et al., 2016). Therefore, it seems that CAGW can play a different role in different time scales. On seasonal-to-interannual time scales, strengthened CAGW during El Niño tends to suppress TC genesis in the EDR, while on synoptic scales, CAGW events can initiate TC genesis. This different role of CAGW in ENP TC requires a more detailed investigation. One of the challenges to address this issue is how to separate the role of synoptic CAGW events from other influences on TCs, such as the monsoon trough and ITCZ. To tackle this issue from a purely observational perspective

can be extremely difficult because of the insufficient sample size, as well as possible covariations in the various influences on TCs.

Although observations of TC central locations and intensities are available dating back to 1851, precise atmospheric probes of TCs only started in the 1970s, when routine use of satellites to track TC development was available. In addition, due to the limited availability of high-resolution reanalysis data, observation-only analyses cannot completely reveal TC variability and relationships between climate modes and TC activity. On the other hand, high-resolution numerical models have been dramatically improved over the recent years and play an increasingly important role in understanding and predicting TCs. In addition, they allow us to perform experiments that can shed light on the causality of the physical factors that influence TCs.

TC simulations using numerical models can be traced back to Manabe et al. (1970), who noted TC-like vortices, with warm core structures, low sea level pressure, heavy precipitation, and strong low-level convergence and upper-level divergence similar to observed tropical cyclones, albeit weaker intensity, in a global circulation model (GCM) simulation. Their findings indicate the possibility of simulating TCs using global climate models. However, to balance the computational costs and the extended simulation periods with multiple ensemble members, even with the current high-performance computing capability, most climate simulations are made with relatively coarse resolutions (~100 km), which are inadequate to directly simulate accurate TC structures. As a result, many current generation climate models have strong biases in TC simulations,

including that simulated TCs are often too frequent and too weak. Perhaps more importantly, Emanuel and Sobel (2013) pointed out that atmosphere-only GCM simulations forced with observed SSTs may lead to an imbalance in surface heat budgets, which may thereby influence precipitation and TC intensity.

A remedy for the coarse resolution problem is the use of a regional modeling approach in which enhanced model resolution that permits explicit TC simulations can be achieved in a limited domain over certain TC active regions. The Weather Research and Forecasting (WRF; Skamarock, 2005) model has been a widely used Regional Climate Model (RCM) in the study of TCs. WRF is a fully compressible, nonhydrostatic model, with a vertical terrain-following hydrostatic pressure coordinate. The model uses high-order numerics, which aims at reducing numerical errors.

To compliment the observational analysis presented in the previous chapter and further quantify CAGW's impacts on ENP TCs, in this chapter we introduce a tropical channel model (TCM) based on WRF version 3.5.1. The TCM utilizes periodic boundaries in the zonal direction with its meridional boundaries placed in the extratropics, allowing atmospheric waves and disturbances to propagate throughout the tropics. As such, it is optimally configured to simulate TCs in the entire global tropics. Given that ENP tropical cyclogenesis is highly influenced by the combination of African easterly waves that propagate from NA and the local monsoon trough (Molinari and Vollaro, 2000; Levine, 2012), the TCM configuration is ideally set to realistically simulate ENP TCs.

Following Patricola et al. (2015, 2017), the TCM covers the entire tropics and subtropics from 30°S to 50°N, with a TC-permitting horizontal resolution of 27km. The top of model is set at 50 hPa level, with 32 vertical layers. The model integration time step is 60s, and output is saved every 6 hour. Initial, northern and southern boundary conditions, and SST are prescribed from the 6-hourly National Centers for Environmental Prediction (NCEP) Climate Forecast System Reanalysis (CFSR, Saha et al., 2010) and its extension, the Climate Forecast System version 2 (CFSv2, Saha et al., 2014).

Although Patricola et al. (2015, 2017) show some success in reproducing observed characteristics of ENSO-induced TC variability in both NA and ENP, they also reveal some severe biases in ENP. For example, the TCM described in Patricola et al. (2015, 2017; hereafter PTCM) simulated too many TCs in the far eastern region of ENP, while TCs' westward propagations were not well captured. Perhaps as a result, the observed ENSO-induced intrabasin variability of the TCs within the ENP, especially the westward (eastward) shift of the TCs during El Niño (La Niña), was not well captured by PTCM. Additionally, the GPI analyses of the model simulations shown in Patricola et al. (2015, 2017) failed to reproduce the negative (positive) GPI anomaly in the eastern portion of ENP during El Niño (La Niña); although the negative (positive) contributions to the GPI from vorticity and relative humidity were captured by the model, they were not sufficiently strong to overpower the positive contribution from the vertical wind shear. Given that the observed CAGW-induced low-level vorticity dipoles seem to dominate the GPI anomalies near the eastern portion of ENP (Figures 2.7b and g), it is possible that the

simulated CAGW by PTCM may not be realistic enough to have a dominant influence on TC activity in this region, causing discrepancy between the observed and simulated TC response to El Niño in ENP. Without further improvement to reduce this significant model bias in ENP region, the TCM is not suitable for this study.

Therefore, the objectives of this Chapter are eliminating the core PTCM model biases in ENP TC simulations, and optimizing the TCM configuration to mostly reproduce a realistic CAGW climate, as well as the associated large-scale circulation features that also potentially contribute to TC genesis.

The Chapter is organized as follows. Section 2 discusses the sensitivity experiments to improve model biases in the ENP. We also introduce a critical TC detection and tracking algorithm to minimize the uncertainty from tracking simulated "non-TC" systems in the same section. Section 3 and 4 validate the newly-configured TCM performance in simulating ENP TCs and CAGW contrasting with observations. ENSO's modulation on the simulated large-scale circulations and TC activity is illustrated in Section 5, to complement the observational analysis presented in Chapter II. A short summary and discussion is presented in Section 6.

3.2 TCM sensitivity experiments and TC-tracking algorithm

3.2.1 Sensitivity to physical parameterizations

Many previous studies documented that use and choice of physical parameterizations in numerical models can have major influences on TC and climate

simulations (Hu et al., 2010; Evens et al., 2012; Nasrollahi et al, 2012; Crétat et al, 2012). To minimize uncertainties that model biases create in the conclusions of this study, a set of 15 sensitivity runs (Table 3.1), each with different physical parameterization schemes, were conducted to obtain the most optimal TCM configuration for simulating ENP TC and climate. Since Yonsei (YSU) University planetary boundary layer (PBL) is shown to have small biases compared to surface and boundary layer observations south of the U.S. (Hu et al., 2010) – in an area close to ENP, we assume that the YSU PBL scheme is also suitable in this study. Three different cumulus (CU), microphysics (MP), and radiation (RA) schemes (Table 3.1) are evaluated to reduce model uncertainties in simulating regional climate. Sensitivity simulations are initialized at 1 May 2008, and outputs are archived every 6-hour from June 1 to Dec 1, after one month of spin-up. The reason we chose the 2008 hurricane season to validate TCM simulation is due to the neutral phase of ENSO and the availability of the Year of Tropical Convection (YOTC) product. YOTC is a joint research program to conduct a better understanding of tropical convection systems, and it is widely used in assessing atmospheric model's representation of tropical convection (Waliser et al., 2012).

The 15 sets of numerical sensitivity tests were evaluated in terms of CAGW, ITCZ over ENP, large-scale circulation, and computational cost. We require that the elected physical parameterizations appropriately represent not only the fine-scale CAGW variability, but also the larger-scale regional circulation related to tropical cyclogenesis. We used Cross-Calibrated Multi-Platform version 2 (CCMPv2) Surface Wind Vector

analyses (Atlas et al., 2011), Tropical Rainfall Measurement Mission (TRMM) multi-satellite precipitation analysis, and YOTC as benchmarks, and found that the simulation (number 12) with the new Simplified Arakawa-Schubert (NSAS; Han and Pan, 2011) CU scheme, Lin (Lin et al., 1983) MP scheme, Dudhia (Dudhia, 1989) shortwave radiation, and rapid radiative transfer model (RRTM; Malwer, 1997) produced most realistic results with moderate computational costs (Figure 3.1, Figure 3.2, Figure 3.3 and Figure 3.4).

3.2.2 TC detection and tracking method

The algorithm to detect and track TCs is adapted from Knuston et al. (2007) and Murakami et al. (2011). But given that fact that ENP TC tracks are usually shorter and more concentrated in space than those over the western North Pacific (WNP) and NA, a set of modified TC detection and tracking criteria was developed for ENP. Using 6-hourly data, grid points in space and time satisfying the following conditions are marked as potential TC snapshots:

1) The local maximum relative vorticity at 850hPa exceeds 1.6×10^{-4} s^{-1}, with minimum wind velocity of 10 m s^{-1}.
2) The local minimum of sea level pressure (SLP) that is within a distance of 2° latitude or longitude from the vorticity maximum center is defined as TC center. SLP needs to increase by at least 4 hPa from the TC center within a radius of 5°.
3) The local maximum of air temperature averaged at 300 and 500 hPa is defined as the

warm-core center. The warm-core center should also be located within a distance of 2° from TC center, and be 0.8 K warmer than the surrounding 5° radius environment local mean.

After identifying potential TC snapshots based on the threshold listed above, the trajectory analysis is performed to connect these together:

1) For each TC snapshots, a spatial scan is performed to see if other satisfied snapshots exist within a distance of 300 km during the next 6 hour.
2) If no other snapshot exists, the trajectory is regarded as having ended. In the case where multiple potential snapshots exist, if the TC center is located south of 35°N, the closest point that is located west and poleward of the current location is chosen as belonging to the same trajectory. Otherwise, eastward/northeastward trajectories are designated.
3) The simulated TC trajectory must last at 2 days, and have a maximum 10m wind velocity within 3° radius of the TC center greater than 17.5 m s^{-1} for at least 2 days (not necessarily continuous).

We build this relatively strict TC detection and tracking algorithm to minimize the error from tracking only "TC-like" disturbances, such like tropical waves and subtropical low-pressure systems. Given that Knuston et al. (2007) and Murakami et al. (2011) used a model with even higher horizontal resolution than TCM, which should better resolve TCs, we believe our modified tracking code is suitable for this study.

3.3 TCM simulated ENP TC climate

Having optimized the TCM configuration, we performed a set of 27-season simulations, which were integrated season by season from the year of 1990 to 2016. A 10-member ensemble is run for each simulation for each year's hurricane season (1 June -1 December), with an initial condition in April or May (see details in Table 3.2) and one month of model spin-up. By designing the control simulation this way, the impact of tropical SST variability on TC activity can be comprehensively evaluated. In addition, the large ensemble size can significantly reduce the simulation uncertainty coming from internal atmospheric variability. This set of control simulations is named as "interseasonal control runs" (refer to CTL hereafter). We finished 270 sets of CTL runs in total.

Figure 3.5 shows the composites of all TC snapshots that reached hurricane categories (maximum surface wind speed $\geq$33m s^{-1}). The rainfall field from TCM simulations includes features resembling well-defined rainbands surrounding a relative low-pressure center inside, creating a clear "eye" structure (Figure 3.5a). The simulated "eye" has a typical width of about 50km, which is consistent with observations. We note that the simulated TC rainfall is highly concentrated at the conventional first and fourth quadrant, which may be caused by the distribution of the land surface rather than the influences from environmental vertical wind shear (Chen et al., 2006), and further investigation is needed. The iconic mature TC structure of low-level inflow and upper-level outflow are also well simulated near the eye-wall area (Figure 3.5c; Frank,

1977). In addition to the good agreement of a realistic inner core structure, simulated TCs also show a remarkably warm-core near the TC center, which peaks at about 350-400hPa (Figure 3.5b). The simulated TC maximum tangential velocity is attained at about 850hPa and less than 100 km from the TCs center, which is again consistent with observations (Frank, 1977). These results confirm that the 27-km TCM is able to resolve TCs, and simulated ENP TCs show great agreement with observed typical TC structures.

To evaluate the model's ability to represent ENP TC spatial distributions, we constructed composites of TC track density. The seasonal track density is defined as the number of 6-hourly TC records (only counting tropical storm or greater category) that passed through each 2°×2° grid box during each hurricane season. We also used a 9-point smoothing filter to reduce the noise and capture principal patterns. The ENP TC observations were derived from the International Best Track Archive for Climate Stewardship v03r10 (IBTrACS, *Knapp et al.,* 2010). To fairly compare to model simulations, we only selected TCs with tropical storm intensity or stronger (i.e., those TCs that possess 1-min sustained surface wind speed at least of 17.5 m s^{-1}).

Compared to observations (Figure 3.6a), the new TCM configuration produces reasonably improved ENP TC spatial distributions (Figure 3.6b), with the majority of simulated TCs confined to the ENP coastal area south of 30°N, and a well-captured westward propagation of some TCs into the central Pacific. Although the TCM underestimates climatological ENP TC activity, interannual variability is reasonably well represented (Figure 3.7), with correlation coefficients between observed and TCM

simulated TC number, accumulated cyclone energy (ACE; Bell, 2000) and number of hurricanes reaching 0.69, 0.69 and 0.58, respectively, which are statistically significant at the 99% confidence level. In addition, the ratio of absolute seasonal mean value to the standard deviations of the 10 ensemble members is typically more than 3 (i.e., high ratio of signal-to-noise; not shown), indicating that variations in TC activity associated with internal atmospheric variability are weaker than those from intrinsic interannual variability, indicating a good potential of skillful seasonal TC predictions.

The spatial distribution of genesis density, defined as the number of tropical cyclogenesis events within a 2°×2° grid box, is shown in Figure 3.8. Consistent with track density, the TCM-simulated ENP TC genesis density compares well to the observed. Most observed and simulated cyclogenesis events occurred in the ENP MDR region, and are especially concentrated near the coastal area east of 120°W. This spatial agreement of TC genesis locations is further supported by GPI analysis. The spatial pattern of model computed GPI is also highly similar to the results from CFS datasets (Figures 3.8c and d), both with a large value of GPI extending westward from the Sierra Madre mountain gaps areas and gathering to a narrow band closing to 120°W. This similarity indicates that the model can represent environmental favorability for TC genesis reasonably well, and the new version of the TCM can better resolve the regional circulations that control ENP TC propagations compared to the TCM used in previous studies.

We note that although 27-km horizontal resolution is high enough to resolve ENP tropical cyclogenesis and TC propagations, the resolution may still be too coarse to

represent the TC inner-core dynamics well, resulting in simulated TCs that are overall weaker than observed. The observed and simulated ENP TC intensities are summarized in a wind-pressure scatterplot in Figure 3.9. The TCM simulates hurricanes into the Saffir-Simpson category-4 range (i.e., 920-944 hPa) in terms of minimum sea level pressure, but only into the category-2 (43-49 m s^{-1}) and occasionally category-3 (>50 m s^{-1}) in terms of maximum surface wind. The strongest hurricane simulated by the model reached a central pressure of about 928 hPa, with maximum surface winds of 52 m s^{-1}, while the most powerful observed hurricane in the ENP basin (Patricia, 2015) had a lowest central pressure of 872 hPa and surface wind of 96 m s^{-1}. The model simulated TC wind-pressure relationship (e.g., red solid line in Figure 3.9) is substantially less linear than the observed, as model deficiencies suppress surface wind speed for a given central sea-level pressure, progressively beginning at values exceeding about 30 m s^{-1}. In addition, the value of simulated seasonal mean number of TCs is also systematically lower than observations. This bias in simulating number of TCs and the wind-pressure relationship deficiency can be partially attributed to the limited model resolution. In addition, air-sea flux parameterizations (Green and Zhang, 2013) may also play a role.

3.4 Simulated CAGW and regional circulation

In addition to the improved spatial distributions of simulated ENP TCs, the TCM is also able to capture well structures of CAGW and associated regional circulations. Figure 3.10 shows the climatology of the TCM simulated 10-m wind field over oceans, in

comparison to the CCMPv2 wind. The CAGW near TT and PP are clearly visible from seasonal mean maps of both observations and model simulations, which seems primarily driven by the prevailing Bermuda-Azores High system. The mean position of the Bermuda-Azores High system is nicely captured, while the simulated downstream Caribbean low-level jet (CLLJ) is stronger than observed. The monsoon troughs are also clearly depicted by the convergence of streamlines in both observations and the TCM simulation, but the cross-equatorial winds from the southern hemisphere in the TCM simulation seem to be slightly weaker. Combined, the simulated seasonal CAGW at TT and PP are stronger.

The synoptic scale CAGW events at TT and PP are identified based on the criteria from Holbach and Bourassa (2014). Consistent with anomalous high seasonal mean 10-m wind speed, the TCM tends to reproduce more frequent (~18% more) and stronger CAGW events than satellite observations (Figures 3.10c, d). Also, consistent with observation, the simulated TT CAGW is typically stronger and has a larger spread in the peak than PP CAGW. Although the TCM simulated CAGW is stronger than observed, the model's overestimates may not be significant given the fact that the actual sampling coverage of satellite-retrieval wind products is less regular than 6-hour model outputs, both in time and space, particularly at the latitudes near CAGW (Holbach and Bourassa, 2014). More importantly, the anticyclonic arcs of offshore TT CAGW are nicely reproduced, as this is the feature whose underlying dynamic explanations are still controversial.

Figure 3.11 shows some regional circulation features that can strongly influence seasonal TC activity. Similar to the atmospheric reanalysis calculated vertical wind shear (VWS), which is defined as the magnitude of 6-hour interval wind vector difference between 200 and 850 hPa, the TCM shows relatively weak environmental shear near the coast (Figures 3.11a and b), and it provides favorable conditions for TC developments. Due to the positive bias in CAGW, the simulated VWS is slightly stronger at TT and PP, but overall corresponds well. The pattern of simulated rainfall rate also compares well with TRMM satellite observations, especially the observed shadows downstream of the CAGW. The width of the simulated ITCZ is still slightly broader, possibly resulting from weaker cross-equatorial winds in the TCM simulation. Despite the limited flaws, this moderate ENP rainfall simulation shows great improvements from many previous studies, as climate models tend to simulate excessive rainfall in this region. It suggests that tropical convection is well reproduced in TCM simulation.

3.5 ENSO's modulation of TCs in TCM

By forcing the TCM with historical interannual SST variability, we can evaluate ENSO's modulation on simulated ENP TC activity. Based on the ENSO classification reported in Chapter II, 8 El Niño and 6 La Niña hurricane seasons were identified. Note however, the actual sample size in the TCM is 10 times larger than in observations due to the 10-member ensemble of TCM simulations.

Figure 3.12 shows the observed and simulated vertical wind velocity at 500 hPa during El Niño and La Niña, comparing to long-term climatology. The tropical deep convection center shifted toward the tropical central and eastern Pacific during El Niño, whereas it became anomalously strong over Maritime Continent during La Niña. Model simulated responses of tropical convection overall agreed with atmospheric reanalysis data, where large anomalous patterns over the Pacific were clearly visible. Although there was another anomalous convection center near 10°N stretching westward from the dateline in the TCM simulation, the intensity was not comparable to the convection anomalies east of dateline. This suggested that, given model forcing of observed SSTs, the TCM can generate realistic ENSO-related large-scale atmospheric instabilities. As a result, we expect the model simulated TC responses to ENSO to be reasonable.

Figure 3.13 shows anomalous VWS between 200 and 850 hPa during different ENSO phases. Consistent with observations, the VWS is characterized by a remarkable decrease in the central Pacific during El Niño, while VWS over NA greatly increased. VWS anomalies are similar, but opposite in sign, during La Niña. The increase of VWS makes environmental condition less favorable for TC development, by disrupting the flow of moisture and heat propagating upward from the sea surface and entraining relatively dry air into the TC. With the presence of strong VWS, the TC will be vertically-titled downstream, less efficient at gaining the massive heat release associated with water vapor condensation, and less likely to strengthen.

Another environmental factor that influences TC activity is mid-level humidity. Figure 3.14 shows the 600 hPa specific humidity responses to composites of El Niño and La Niña events. Tightly linked with tropical convection instabilities, the mid-troposphere tropical central Pacific was moister during El Niño than La Niña, potentially providing a greater energy source for TC development. Combined with the simulated VWS changes, ENSO-induced anomalous atmospheric circulations associated with favorability of TC activity are represented well by the TCM.

Figure 3.15 demonstrates the ENSO-induced TC track density anomalies in both observations and the TCM simulations. Due to the limited sample size of observations, the observed track density anomalies shown here were not perfectly identical to some previous studies, which made composites based on a larger data archive, but the overall anomalous patterns were consistent. During El Niño, WNP TC activity tended to shift toward the central Pacific, which was also the case for ENP TCs, where intrabasin variability was observed. TCs over the NA were strongly suppressed during El Niño, resulting primarily from the increased VWS. In our TCM simulation, the anomalous TC activity during El Niño hurricane seasons was even better-represented compared to earlier TCM configurations, with a homogeneous increase in the central Pacific and a decrease in NA. The observed CAGW-related ENP intrabasin TC variability was also reproduced in the model, which is a great improvement from PTCM. The TC responses to La Niña are analogous to El Niño, but opposite in sign.

3.6 Summary and discussion

In this Chapter, we performed large sets of numerical sensitivity tests to correct the model bias in previous TCM studies. With refined physical parameterization scheme configurations, the TCM shows great improvement in simulating ENP TCs, CAGW, and regional circulations linked with tropical cyclogenesis. Although the simulated ENP TCs are overall weaker than observations, likely resulting from the relatively coarse TCM horizontal resolution, they are characterized by the iconic observed TC structure. In addition, the simulated ENP TCs are also correlated strongly with observations on the interannual timescale. Given that TCM is relatively cheap and easy to run, it provides a great potential to improve seasonal TC forecasting skill by downscaling the TCM from coarse resolution coupled global seasonal forecast models.

Due to limited computational resources, we note that the physical parameterization schemes we selected may not be the "best", but they are appropriate to address this topic of research. For different research topics, similar benchmark work is highly suggested before investigation.

Table 3.1 15 sets of sensitivity tests to investigate the optimized TCM physical parameterizations.

ID	Cumulus	Mircophysics	Shortwave radiation	Longwave radiation
01	Kain-Fritsch	Purdue Lin	Goddard	RRTMG
02	Kain-Fritsch	Purdue Lin	Dudhia	RRTM
03	Kain-Fritsch	WDM6	Dudhia	RRTM
04	Kain-Fritsch	Eta Ferrier	Dudhia	RRTM
05	Kain-Fritsch	Purdue Lin	New Goddard	New Goddard
06	Betts-Miller-Janjic	Purdue Lin	Goddard	RRTMG
07	Betts-Miller-Janjic	Purdue Lin	Dudhia	RRTM
08	Betts-Miller-Janjic	WDM6	Dudhia	RRTM
09	Betts-Miller-Janjic	Eta Ferrier	Dudhia	RRTM
10	Betts-Miller-Janjic	Purdue Lin	New Goddard	New Goddard
11	New Simplified Arakawa-Schubert	Purdue Lin	Goddard	RRTMG
12	New Simplified Arakawa-Schubert	Purdue Lin	Dudhia	RRTM
13	New Simplified Arakawa-Schubert	WDM6	Dudhia	RRTM
14	New Simplified Arakawa-Schubert	Eta Ferrier	Dudhia	RRTM
15	New Simplified Arakawa-Schubert	Purdue Lin	New Goddard	New Goddard

Table 3.2 Initial conditions, lateral boundary conditions (LBCs) and SST for TCM simulations.

	Ensemble member	LBCs	SST	Atmospheric initial conditions
CTL	1-10	6-hourly 1990~2016	6-hourly 1990~2016	April 23, 25, 27, 29 and May 1, 2, 3, 4, 5, 6 of each year

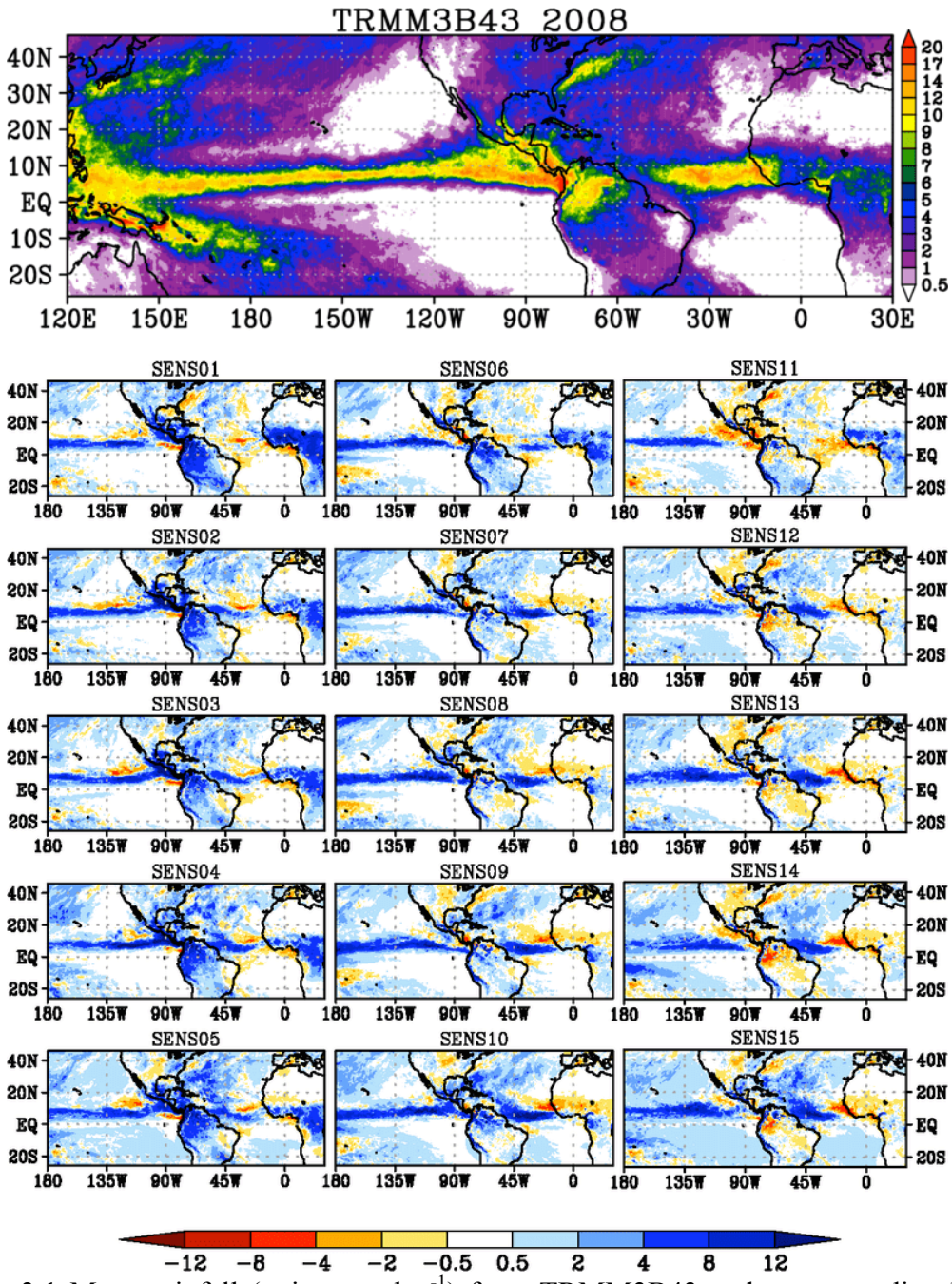

Figure 3.1 Mean rainfall (unit: mm day^{-1}) from TRMM3B43 and corresponding biases from 15 runs of sensitivity experiments during the 2008 hurricane season.

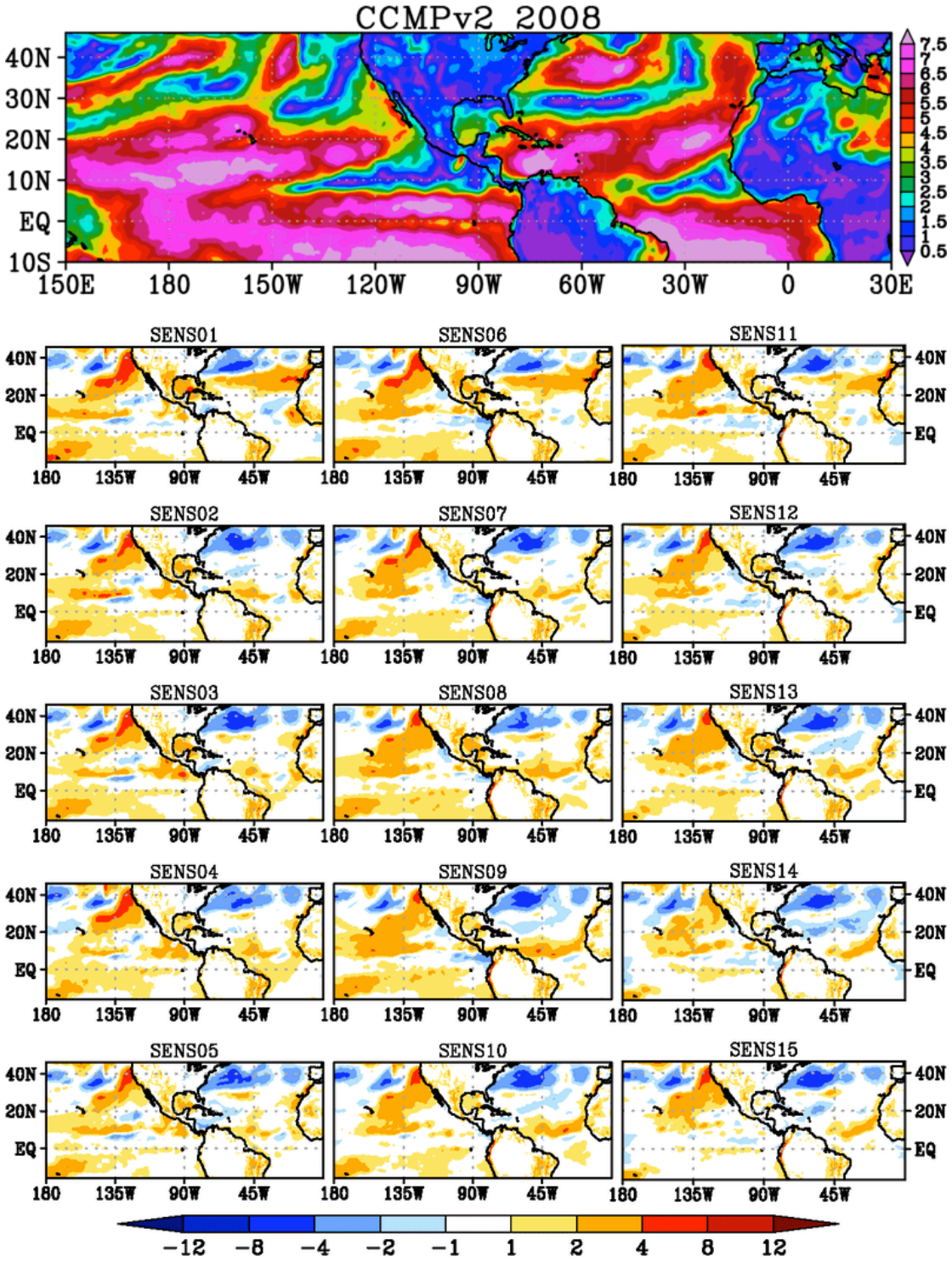

Figure 3.2 Mean 10-m wind speed (unit: m s^{-1}) from CCMPv2 and corresponding biases from 15 runs of sensitivity experiments during the 2008 hurricane season.

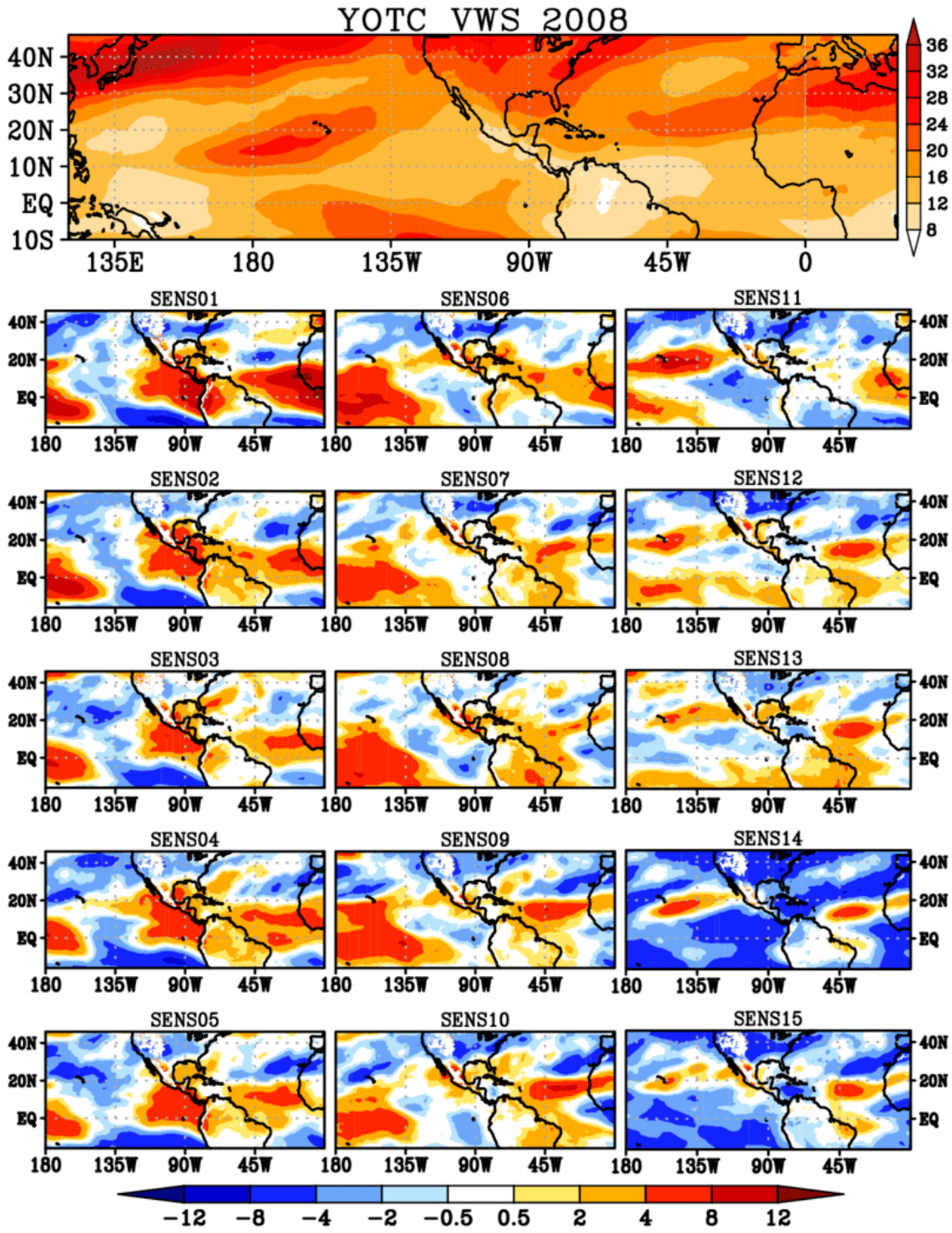

Figure 3.3 Mean vertical wind shear between 200 and 850 hPa (unit: m s^{-1}) from YOTC and corresponding biases from 15 runs of sensitivity experiments during the 2008 hurricane season.

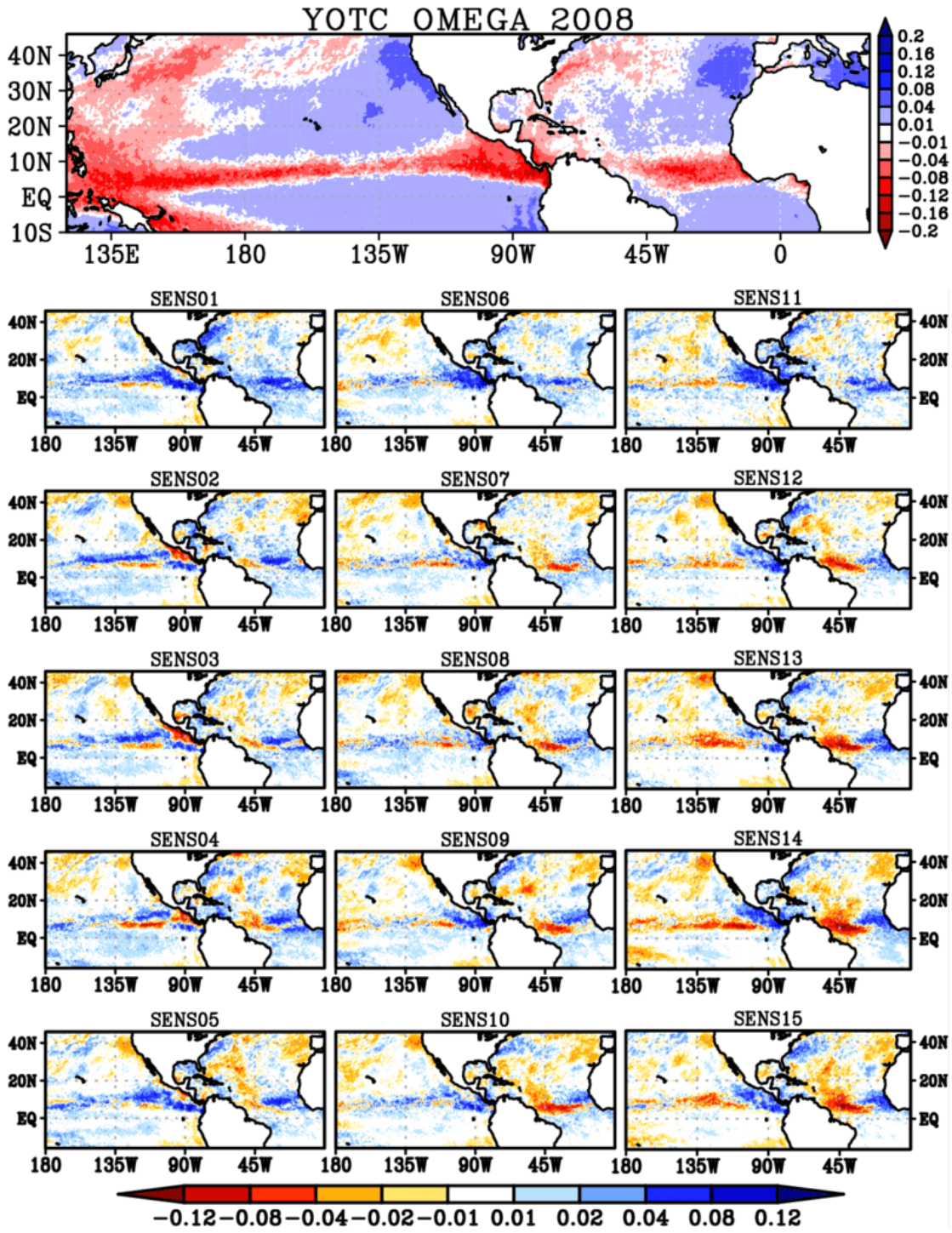

Figure 3.4 Mean 500 hPa vertical wind velocity in pressure level (ω; unit: Pa s^{-1}) from YOTC and corresponding biases from 15 runs of sensitivity experiments during the 2008 hurricane season. Note that warm colors indicate upward motion, while blue colors indicate downward motion.

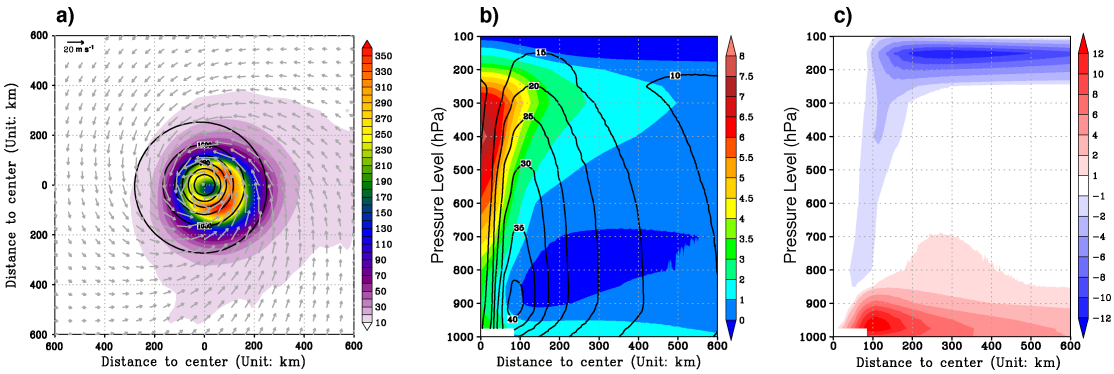

Figure 3.5 Composites structure for TCM simulated ENP TCs. a) Mean 10-m surface wind velocity (unit: m s^{-1}; vector), precipitation rate (unit: mm day^{-1}; shading), and sea level pressure (unit: hPa; contour). Vertical cross section of b) azimuthal mean temperature anomaly (unit: K; shading) along with tangential wind speed (unit: m s^{-1}; contour), and c) radial wind speed (unit: m s^{-1}; positive means inflow, and negative means outflow). Composites are made with simulated TCs that intensified into hurricane strength (≥33m s^{-1}).

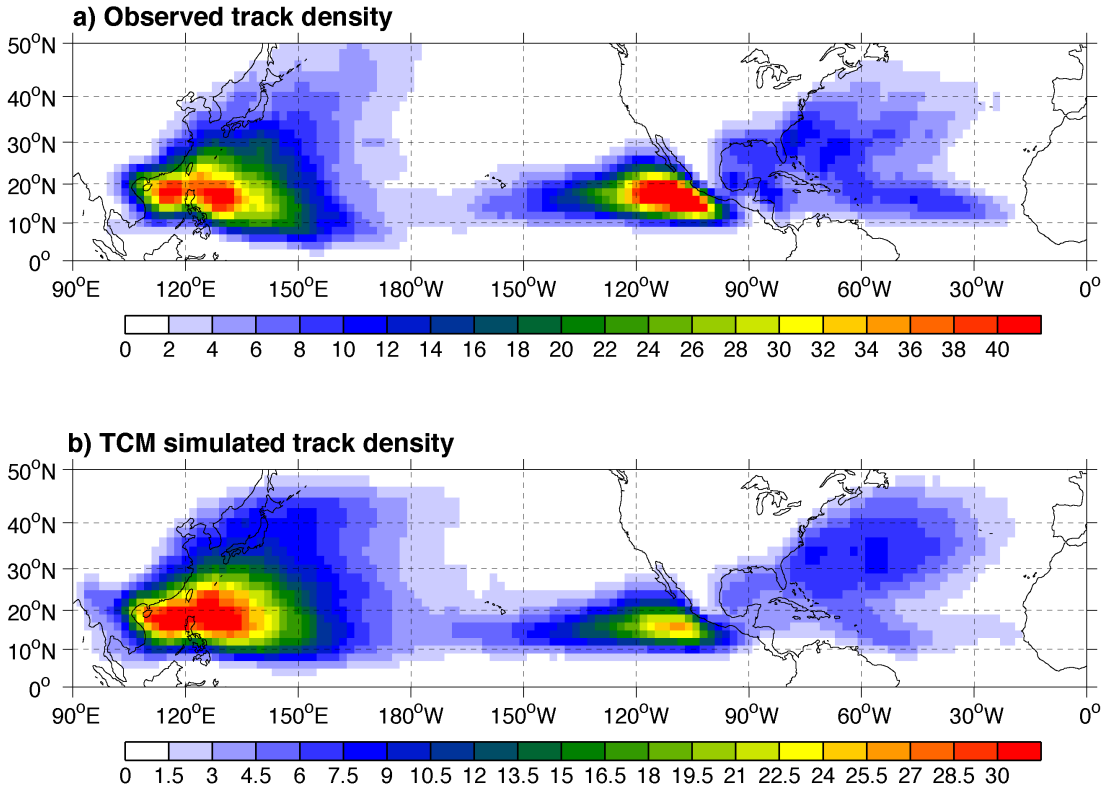

Figure 3.6 TCs track density (unit: TCs per decade) derived from a) IBTrACS and b) TCM 10-member CTL runs. Note that colorbars shown on two panels are different, given the fact that TCM has 10 times more sample size than observation.

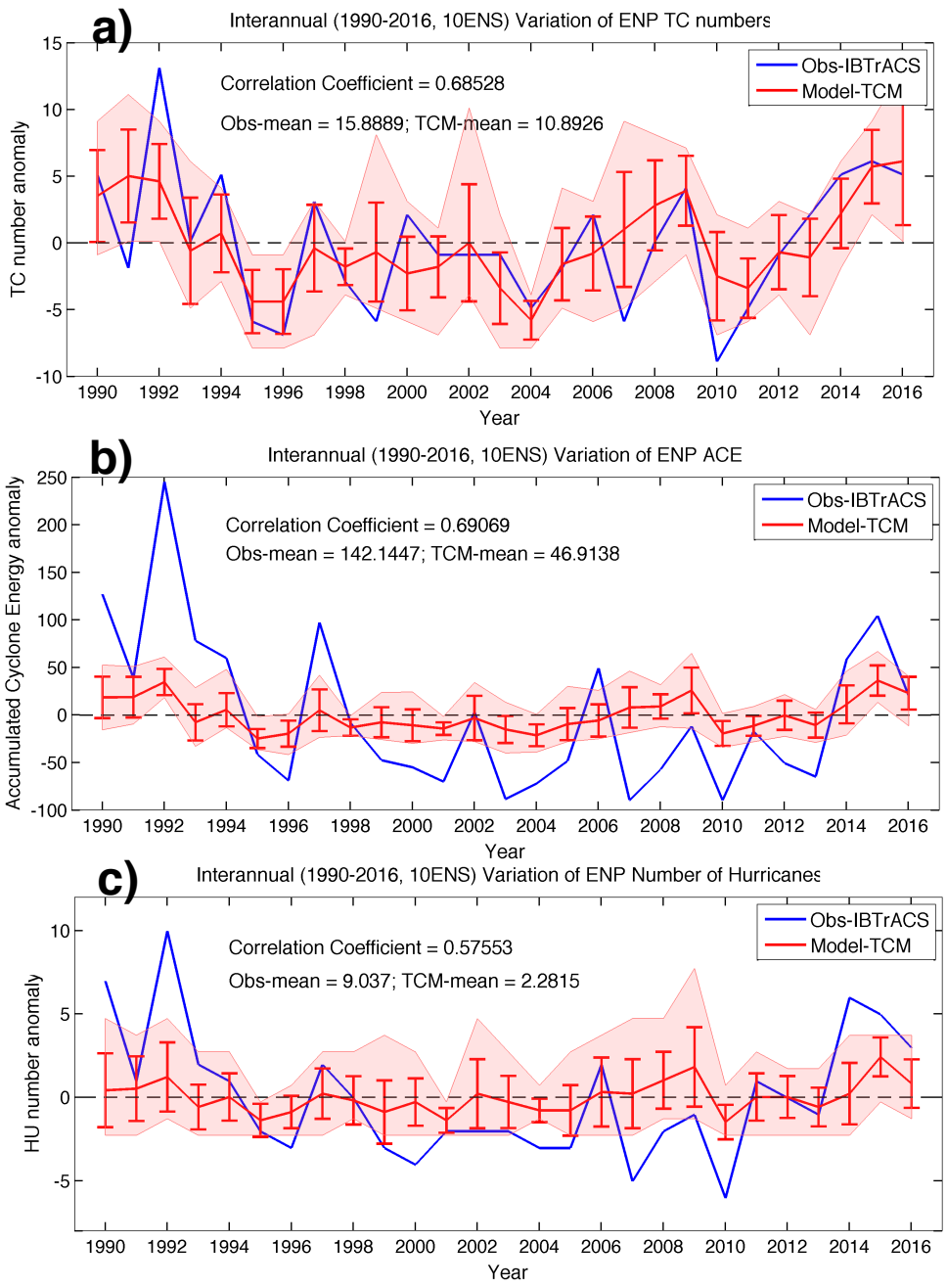

Figure 3.7 Time series of observed (blue) and TCM simulated (red) ENP a) TC number anomaly b) ACE and c) hurricane number from 10-member ensemble simulation. Shaded area shows the simulated maximum and minimum number for each season from the 10-member integrations. Error bar represents the two-sided standard deviation. Correlation coefficient and mean value of the two time series are listed in the panel, respectively.

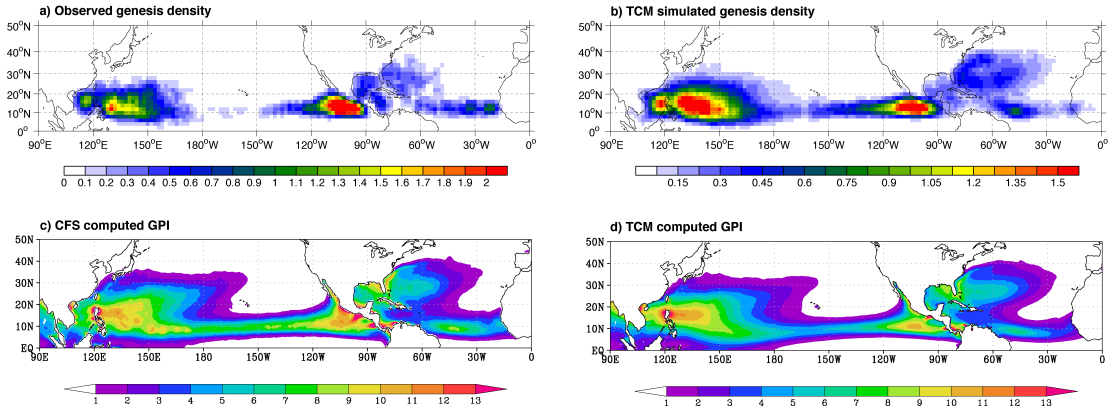

Figure 3.8 TCs genesis density (unit: TCs per decade) derived from a) IBTrACS and b) TCM 10-member CTL runs. Note that the colorbars shown on the two panels are different, given that TCM has 10 times more sample size than observation. GPI (unitless) averaged during JJASON 1990-2016 from c) CFS (CFSR for 1990-2010, CFSv2 for 2011-2016) and d) TCM 10-member CTL runs.

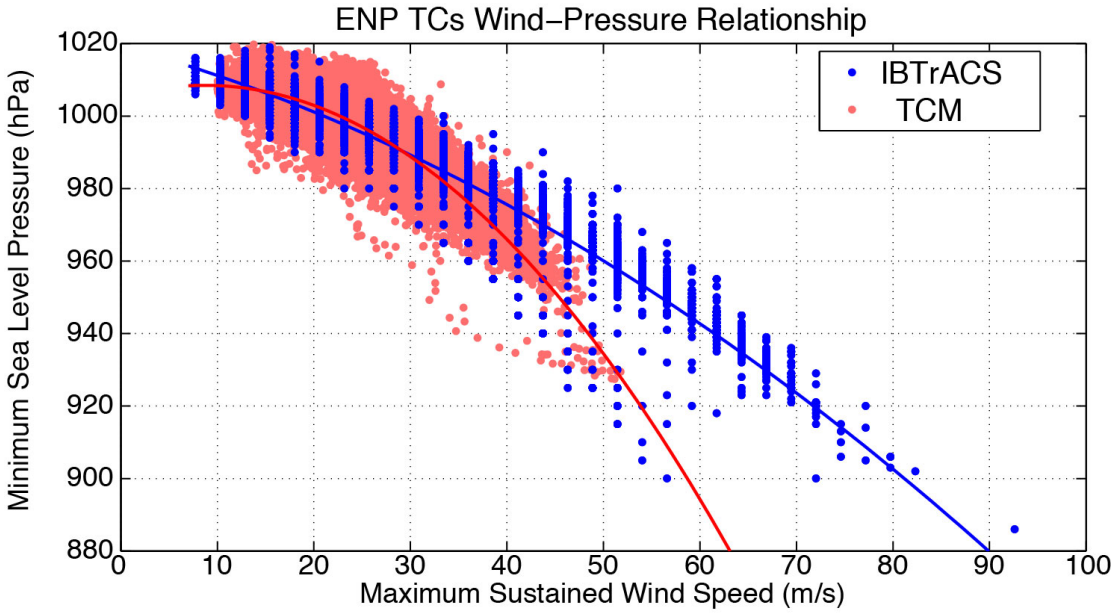

Figure 3.9 Scatterplot of maximum TC 10-m surface wind velocity (unit: m s^{-1}) versus minimum TC sea level pressure (unit: hPa) from observations (blue) and 10-member ensemble TCM simulations (red). Solid lines are least squares quadratic best-fit lines to the points.

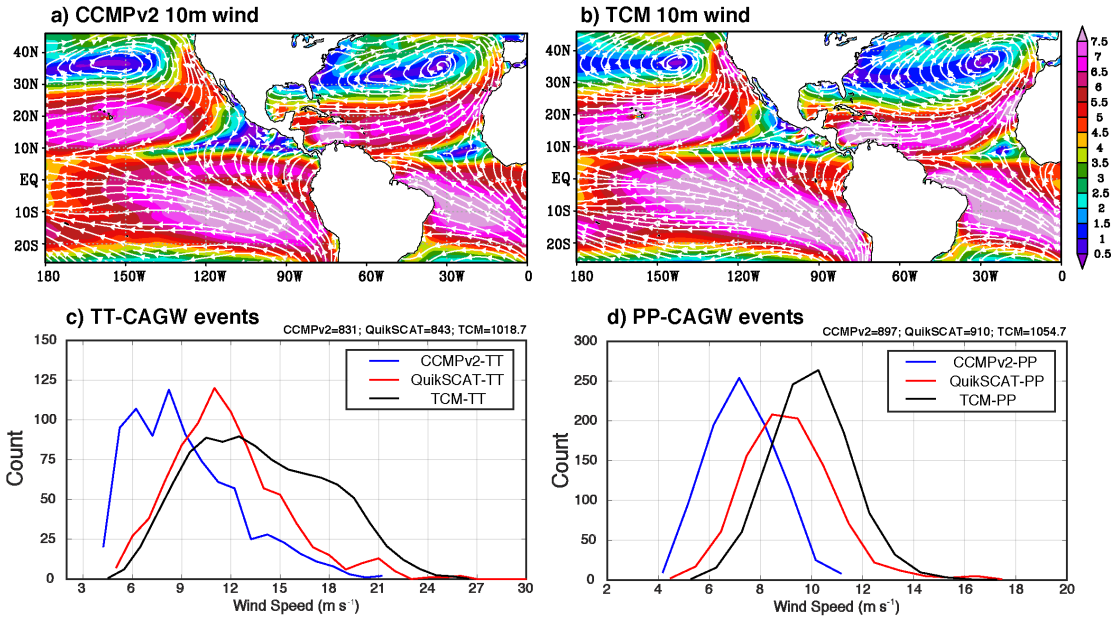

Figure 3.10 Composite of JJASON 1990-2016 averaged 10-m wind over oceans from a) CCMPv2 and b) TCM 10-member ensemble CTL runs. Color shading indicates wind velocity (unit: m s^{-1}), and streamline indicates wind direction. c) and d) are probability distribution functions of CAGW events at TT and PP, respectively. The blue curves indicate CCMPv2, the red curves indicate QuikSCAT and the black curves indicate TCM derived CAGW events. For a comparison, only CAGW events that occurred during JJASON 2000-2009 (QuikSCAT period) are counted. Total numbers of CAGW events are listed on the panels.

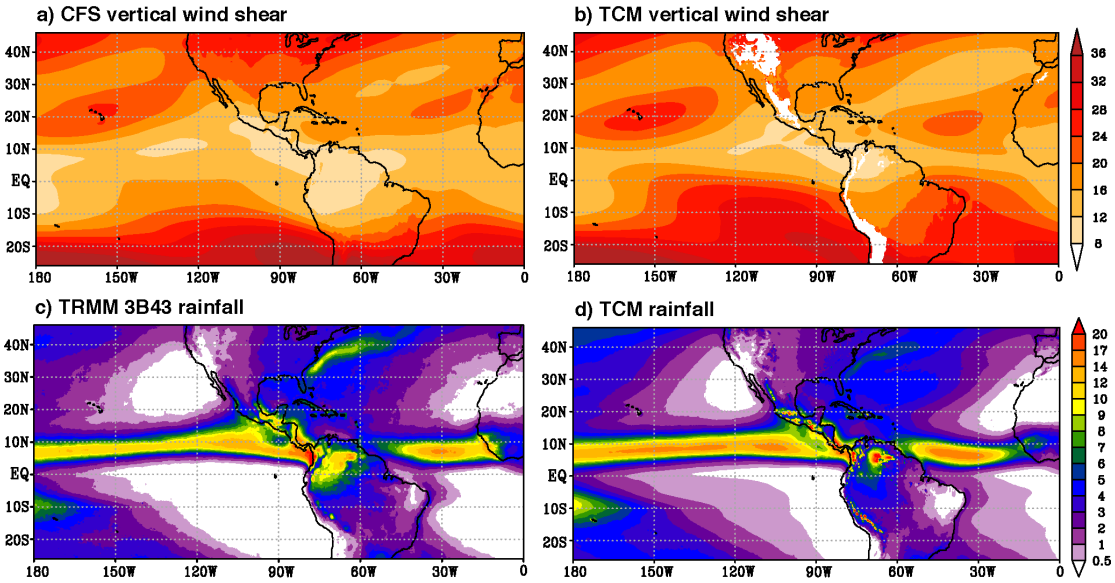

Figure 3.11 Composite of JJASON 1990-2016 averaged vertical wind shear (unit: m s^{-1}) from a) atmospheric reanalysis and b) TCM 10-member ensemble CTL runs. c), d) as in a), b), but for averaged rainfall (unit: mm day^{-1}) during JJASON 1999-2016 averaged (TRMM period) from TRMM and TCM.

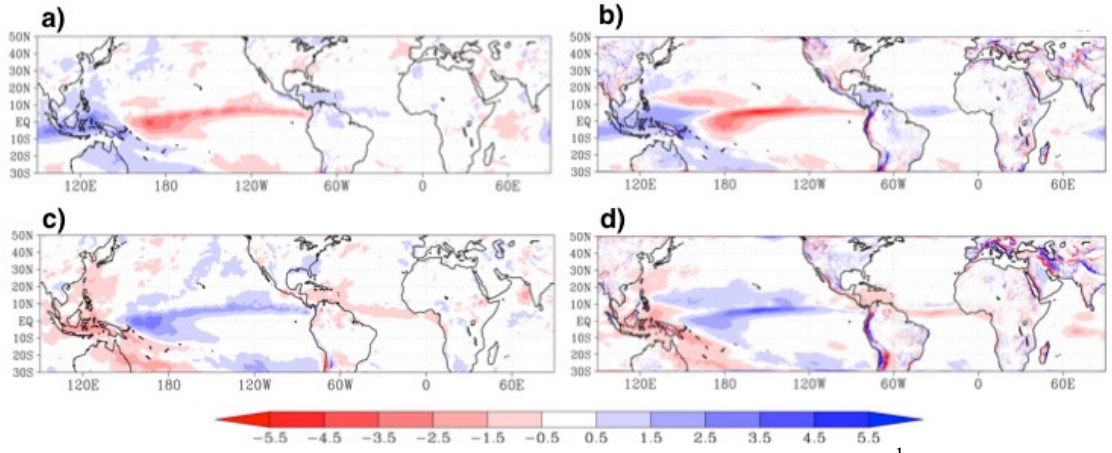

Figure 3.12 The difference in 500hPa vertical velocity (ω ; unit: Pa s^{-1}; negative indicates upward motion) from the composite of El Niño hurricane seasons minus climatology in a) atmospheric reanalysis and b) the TCM simulations. c) and d) are similar, but for the difference from La Niña hurricane seasons composite minus climatology. ENSO classifications are obtained from Figure 2.2.

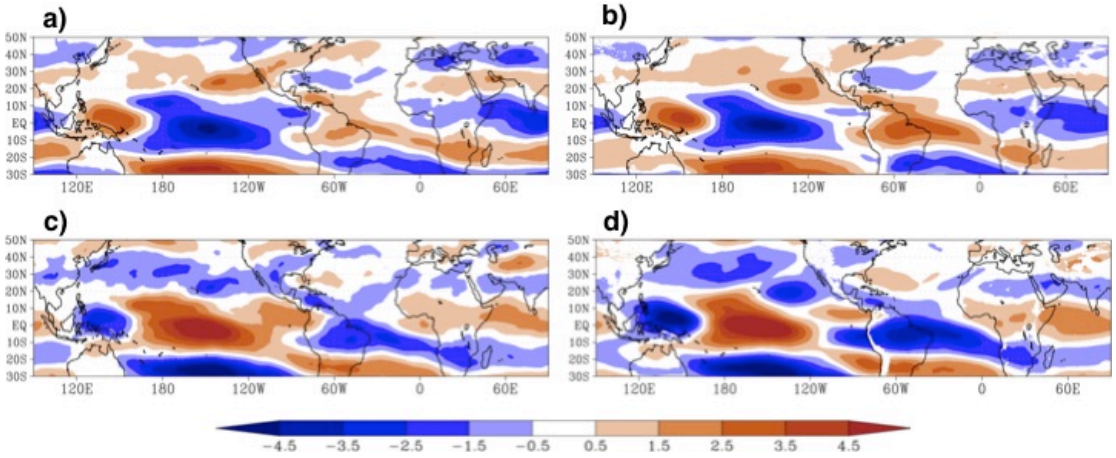

Figure 3.13 The difference in 200-850 hPa VWS (unit: m s^{-1}) from the composite of El Niño hurricane seasons minus climatology in a) atmospheric reanalysis and b) the TCM simulations. c) and d) are similar, but for the difference from La Niña hurricane seasons composite minus climatology. ENSO classifications are obtained from Figure 2.2.

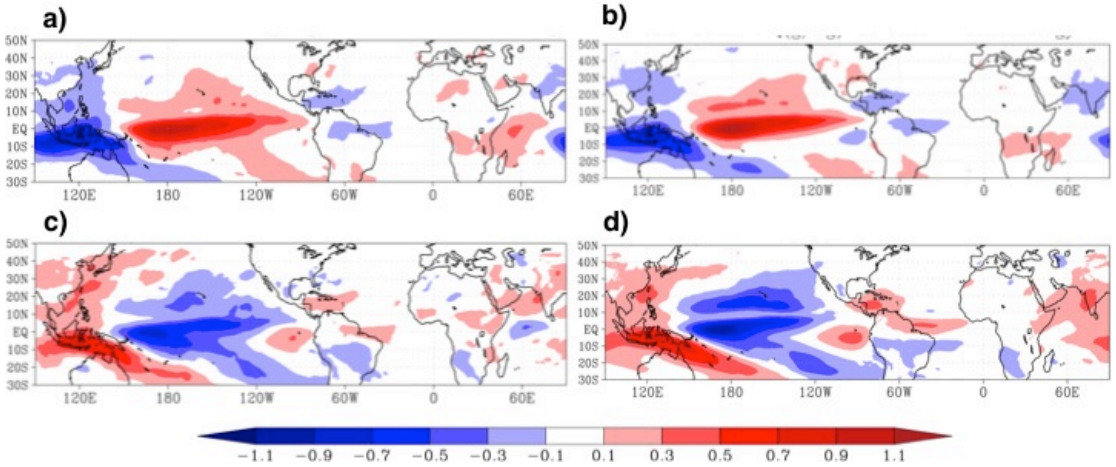

Figure 3.14 The difference in 600 hPa specific humidity (unit: g kg^{-1}) from the composite of El Niño hurricane seasons minus climatology in a) atmospheric reanalysis and b) the TCM simulations. c) and d) are similar, but for the difference from La Niña hurricane seasons composite minus climatology. ENSO classifications are obtained from Figure 2.2.

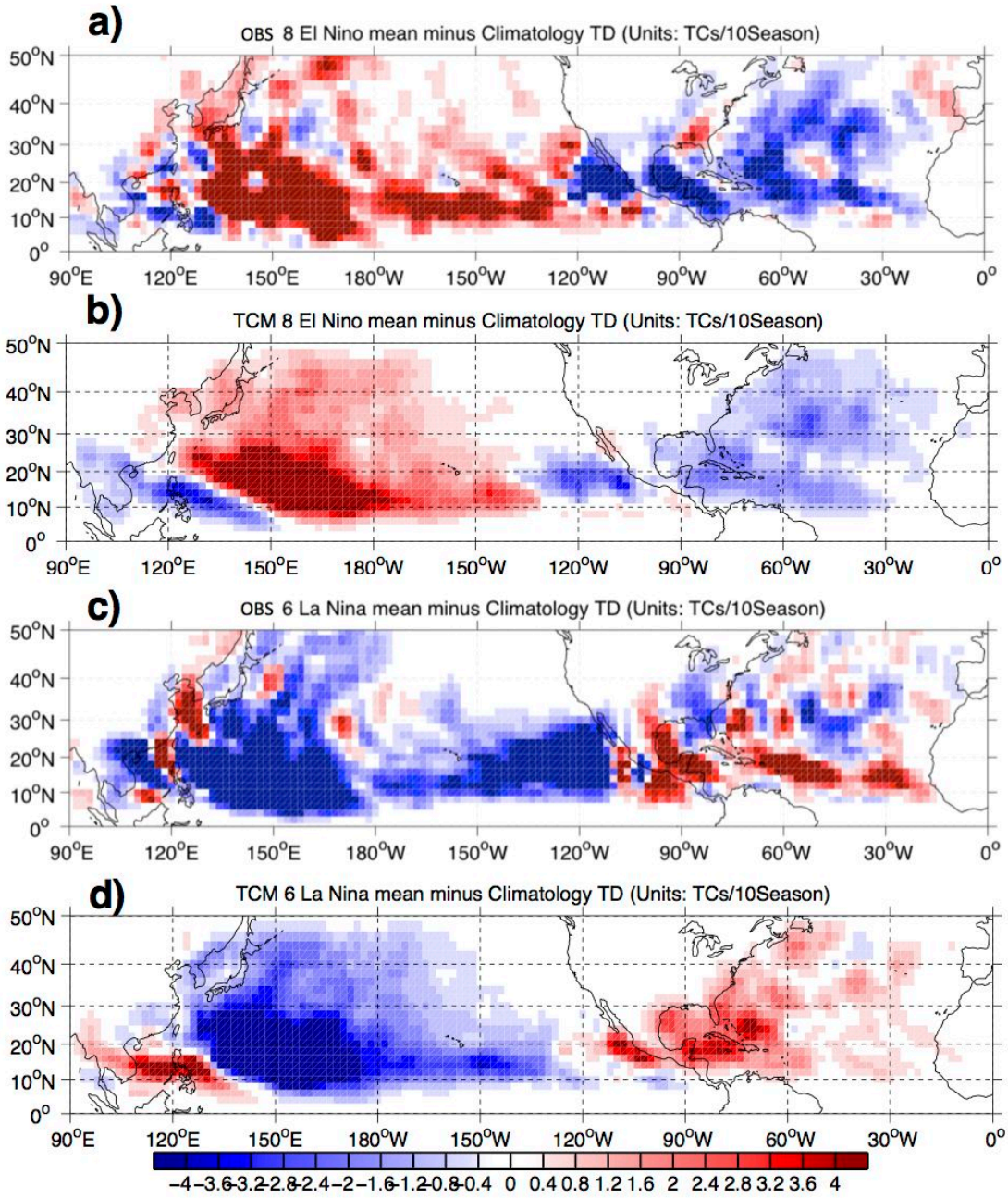

Figure 3.15 The difference in TC track density (unit: TCs 10seasons^{-1}) from the composite of El Niño hurricane seasons minus climatology in a) observations and b) the TCM simulations. c) and d) are similar, but for the difference from La Niña hurricane seasons composite minus climatology. ENSO classifications are obtained from Figure 2.2.

CHAPTER IV

QUANTIFY GAP WINDS' IMPACT ON EASTERN NORTH PACIFIC TROPICAL CYCLONES

4.1 Introduction

As discussed in previous Chapters, in addition to the highest density of TC activity, the ENP is also characterized by a unique topographically-locked feature, CAGW. CAGW features a secondary peak during the hurricane season, and is able to induce significant seasonal intrabasin TC variability, a distinctive east-west spatial variation in TC activity, under the influence of ENSO. Nevertheless, satellite observations also indicate that some individual TC cases are closely related to synoptic-scale CAGW events, for example, Hurricane Celia (2004), Hurricane John (2006), and Hurricane Patricia (2015). This discrepancy suggests that CAGW may modulate ENP TCs in different ways for different timescales. On one side, anomalously strong CAGW causes net negative low-level nearshore vorticity anomalies that inhibit ENP TC developments on the seasonal timescale, and on the other side, a moderate CAGW event can trigger cyclonic disturbances that initiate tropical cyclogenesis on the synoptic timescale. Thus, there remains large uncertainty in the net effect of CAGW's on ENP TCs, and more rigorous undertakings are required to fully understating the underlying dynamic mechanisms and improve seasonal forecasting skills.

In addition to the contributions from CAGW, several other environmental controls are also important for ENP tropical cyclogenesis (Levine, 2012). The confluence of southwest cross-equatorial flow and northeast trade winds generates a large-scale cyclonic background within the monsoon trough, and the tropical easterly waves that traverse Atlantic basin can also create synoptic-scale environments rich in initial cyclonic disturbances (Avila, 1991; Avila and Pasch 1992; Molinari et al., 1997, 2000). More importantly, these synoptic-scale events are not separate phenomena, as several observations revealed the interaction between African easterly waves and CAGW could create perturbations in the monsoon trough that further enhanced low-level relative vorticity. Furthermore, the presence of both an African easterly wave and the monsoon trough are not necessary for tropical cyclogenesis, as WNP TCs can form just within the monsoon trough (Frank, 1988; Ritchie, 1995; Lander, 1994; Chen et al., 2004; Chen et al., 2008; Yoshida and Ishikawa, 2013), while NA TC genesis is typically related to African easterly waves (Dunn, 1940; Frank, 1970; Landsea, 1993; Russell et al., 2017). Therefore, it is extremely difficult to estimate how much CAGW can influence on ENP TCs from pure observational analysis, as tropical cyclogenesis often results from the combination of several synoptic events.

As discussed in Chapter III, numerical modeling provides us the ideal tool to study TCs. Using the properly configured TCM, we can design idealized experiments that block CAGW by artificially closing the mountainous gaps, allowing us to test hypotheses that are difficult to address using just observations. By doing so, the CAGW is artificially

eliminated while still keeping the regional circulation in ENP largely unchanged. From this, we can directly estimate the contributions that CAGW make to ENP TCs. Given that the optimized TCM can reproduce realistic climatologies of ENP TCs and CAGWs compared to observations, we have confidence that the TCM is suitable to elucidate this scientific understanding.

The Chapter is organized as follows. Section 2 introduces the methodology by which we close the mountainous gaps at TT and PP, and the simulation results are validated. Section 3 discusses the TC detection and tracking results, and the response relative to the CTL simulation. The environmental condition changes relevant to the corresponding TC activity anomalies are examined in Section 4. The cause of CAGW-related anomalous mid-level moisture variability is briefly discussed in Section 5. Section 6 summarizes the preliminary results and highlights the importance of this work in improving seasonal TC forecasts.

4.2 Idealized topography experiments

In order to separate the CAGW's direct contributions from other synoptic features, we blocked the CAGW by artificially closing the topographical mountain gaps at TT and PP in the TCM. Due to the west-east orientation of the TT gap in the Sierra Madre, the land surface elevations in a rectangular box near TT (16.5°N -17.5°N, 97°W-91°W) were modified. First, the zonal means and standard deviation of topography at different latitudes were calculated. Then locations with elevations lower than the value of the

latitude-dependent mean plus on one standard deviation (critical values) were multiplied by a small factor repeatedly, until the modified elevations were larger than the original critical values. We also applied a 2-D Gaussian filter with standard deviation of 0.5 to smooth the modified topography. After artificial modification, the mountainous gap at TT was entirely closed, while keeping the non-gap regions and overall mountain stretches close to their original condition (Figure 4.1c). Due to the northwest-southeast orientation of terrain near PP, a similar technique was conducted to PP region as well, except a parallelogram, rather than a rectangular, box of surface elevations was modified. Figure 4.1d shows the original and modified surface elevations near PP, with the mountainous gap eliminated.

Using the idealized surface elevation data with closed TT and PP gaps, we performed simulations similar to CTL using 1990-2016 initial and boundary conditions. Due to the expensive numerical costs, we only conducted a 3-member ensemble (initial and boundary conditions are same as first 3 members of CTL) for each hurricane season's simulation, and completed a total of 81 idealized runs with closed mountainous gaps at TT and PP. We refer to this experiment as "interseasonal no-gap runs" (hereafter, NOGAP for short).

Figure 4.2 shows the 10m-wind field from the NOGAP simulation, overlaid by the modified topography. After closing the mountainous gaps, we successfully blocked the CAGW at TT and PP, while the Bermuda-Azores high-pressure system and CLLJ are almost identical to CTL (Figure 4.3a). Although a small region with relatively stronger

wind speed and a weak anticyclonic arc exists at north of PP, the intensity is not comparable to CAGW, and it may be induced by the increased downslope windstorm results from the topography change (Figure 4.2b). Figure 4.3c shows the difference of near surface relative vorticity relative to CTL, and the primary changes are only confined to the coastal region. In particular, the blocked mountainous gaps also force upstream anomalous flows propagating along the coast equatorward, further generating positive relative vorticity anomalies due to shear effects. The idealized topography experiment is able to eliminate the CAGW signals while maintaining a regional circulation mostly similar to that in CTL.

4.3 ENP TCs activity without CAGW

We identify TCs in the NOGAP simulation using the same TC detection and tracking algorithm discussed in Chapter III. After blocking the CAGW, the seasonal mean number of ENP TCs decreases from 11.22 in the CTL simulation to 8.31 for the NOGAP run, which represents a reduction of 25.96% (2.91 per season) compared with the CTL run (Figure 4.3a and Table 4.1). This suppression is statistically significant at the 99% level. We note that this suppression comes primarily from the EDR, where the number of TCs decreased by 2.07 per season (33.44% of reduction apart from averaged value of 6.19 in CTL; statistically significant at the 99% level) (Figure 4.3b and Table 4.1). The shadings in Figure 4.3 indicate the range of the 3-member ensemble simulation during each season. Red curves and shadings are mostly located beneath blues, indicating

that the reduction of the 27-season mean is not simply due to seasons with extremely inactive TC simulations. Indeed, the reduced TC activities are present in almost each season.

The same conclusion can be drawn from scatterplots. Figure 4.4 shows the scatterplot of simulated number of TCs from 81 sets (27 seasons × 3-member ensemble) of CTL (x-axis) versus NOGAP (y-axis). The top panel shows TCs that originated over the entire ENP, while the bottom panel sub-selects for only those TCs with genesis in the EDR of ENP. Most of markers are located just below the diagonal lines, meaning that CTL systematically simulated greater TC numbers than NOGAP. Figure 4.5 is same as Figure 4.4, except markers represent the number of simulated days with TC activities. Again, the majority of markers are beneath the dotted line. The accumulated TC days over the entire ENP in the NOGAP simulation is 45.94 per season, while the CTL simulation has 61.13 TC days per seasons, a reduction of 24.86%. When we confine to the EDR only, the number of TC days per season is similarly reduced by 22.81% (13.84 comparing to 17.93) in NOGAP (Table 4.2).

In addition to the area-integrated measures, we also evaluated this reduction in terms of spatial distribution. Figure 4.6 shows the track density and genesis density difference (NOGAP minus CTL). It reveals that the marked TC reduction covers most of the ENP, and the magnitude of this change is comparable to ENSO's observed modulation on ENP TCs (Figure 2.4). Note however, TC activity in the Gulf of Mexico and the Caribbean Sea is also changed, with negative anomalies over the west coast of the Gulf of Mexico

and positive anomalies near Panama channel. The underlying mechanism will be discussed in following section.

The simulated TC wind-pressure relation is also compared between NOGAP and CTL (Figure 4.7). The dispersion and best-fitted line in NOGAP is analogous to CTL, both showing a simulated maximum surface wind velocity of ~50 m s^{-1} minimum sea level pressure of ~940 hPa. This result suggests that CAGW's influence on TC intensity may be limited, and ENP TCs' intensification may be controlled by other environmental factors (e.g. anomalous warmer SSTs, weak VWS, sufficient moisture and, so on). In addition, the narrow band of dots in CTL that stand out from the main cluster and are beneath the regressed curve is absent in the NOGAP simulation, likely resulting from the decreased nearshore TC activity. This cluster of dots may characterize TC cases with low sea level pressure near the center but lower than typical surrounding maximum wind speed possibly due to the land's drag effect.

We also examined ENSO's impact on ENP TCs in the CTL and NOGAP simulations, over the entire ENP and over the EDR, using the definitions of El Niño and La Niña in Chapter II. The reds, blues, and blacks on Figure 4.4 and Figure 4.5 refer to El Niño, La Niña, and neutral ENSO, respectively. The markers with different colors located on the axes denote the mean value of number of TCs and TC days during each phase, respectively. Over the entire ENP, the colorful dots from the CTL simulation (x-axis) are relatively clustered, revealing that the changing of TC numbers and TC days caused by ENSO's modulation is minimal (Figure 4.4a and Figure 4.5a). Nevertheless, the colorful

crosses, which only measure TC activity in EDR, in turn demonstrate more obvious responses to ENSO's modulation, with decreased activity during El Niño and increased activity during La Niña. This is consistent with the observed ENSO-induced intrabasin TC variability discussed in Chapter II. The weak modulation over the entire ENP results primarily from the net effect of opposite sign changes in the western versus eastern nearshore area, where TC activity tends to reduce substantially during El Niño and increase during La Niña.

In contrast to the CTL simulation, ENSO's modulation in the NOGAP simulation is more significant throughout the ENP. The colorful dots on the y-axes of the scatterplots have more clear dispersals, with conventional increased TC activity during El Niño and decreased TC activity during La Niña over the entire ENP. However, the colorful crosses again gather clustered, which indicates that NOGAP simulated EDR TC activity does not change significantly under ENSO's modulations. The mean values listed on x-axes and y-axes can be found in Table 4.1 and 4.2.

Consistent with the results from scatterplots, the correlation coefficient between simulated TC activity and the Niño3.4 index also shows a significant difference depending on whether the TT and PP gaps are open or closed (Table 4.1 and Table 4.2). In the CTL simulation, the correlation between ENP number of TCs (TC days) and Niño3.4 index is only 0.12 (0.18), whereas there is a robust negative correlation of -0.39 (-0.46) for TCs that originated in the EDR region. Again, it is interesting that the correlation between ENP number of TCs (TC days) and Niño3.4 index significantly

grows to 0.36 (0.41) just by closing the CAGW. In this scenario, EDR TC activity has almost no correlation with ENSO index.

Although the mean simulated TC activity in NOGAP is about 26% weaker than that in CTL (Figure 4.3 and Table 4.1 and 4.2), all of these results further prove that the intrabasin variability of ENP TCs during ENSO is primarily driven by CAGW variability, and if the CAGW is blocked, ENSO will have a conventional robust modulation on ENP TCs, with anomalous high (low) activity over entire basin during El Niño (La Niña). We note that even without CAGW's contributions, the TC responses to ENSO in the EDR is still slightly opposite in sign compared to the TC response over entire ENP, revealing that the intrabasin variability is greatly weakened but still exists. We will discuss the underlying physical mechanism in next section.

4.4 Reasons for CAGW's impact on ENP TCs

In order to understand the underlying dynamic process that control the significant reduction of ENP TC activity in response to closing the TT and PP gaps, we also analyzed GPI for the NOGAP simulation. Consistent with the ENP TC genesis density response, the NOGAP-computed GPI also shows a substantial decrease over the majority of the ENP, except over the coastal regions that are dominated by CAGW-induced anticyclonic vorticity in CTL. Even though the fanlike CAGW can induce both cyclonic and anticyclonic vorticity through horizontal shear and additional curvature of flow, this result indicates that the CAGW overall contributes to tropical cyclogenesis, and the TC

environmental favorability in the ENP would be reduced without CAGW. In the western portion of Caribbean Sea, the increased GPI is analogous to the TC genesis density changes, while the decreased genesis density in the west coast of the Gulf of Mexico is not represented by the change of GPI. The GPI anomalies in the Gulf of Mexico exhibit a north-south dipole, but the TCs show less tendency to form in the east of the Gulf.

We further estimated which factors contributed most to the responses in GPI. To do so, we recalculated GPI by setting one term to the value from NOGAP, and setting the other three as values from CTL simulation (Camargo et al., 2007; Patricola et al., 2015). The great reduction of GPI in ENP is primarily driven by the low-level vorticity changes, caused by the eliminated CAGW-induced low-level relative vorticity (Figure 4.8b). At the same time, due to the absence of the gale-force low-level jets, the VWS between upper-level weak easterlies and low-level prevailing easterly winds also decreases, making more favorable conditions for tropical cyclogenesis (Figure 4.8d). The increased GPI in the south of the Gulf of Mexico and the Caribbean Sea is net effect of reduced vertical wind shear and anomalous cyclonic vorticity near Panama due to increased shear vorticity. Note however, above the extent of surface elevation in the mid-troposphere, relative humidity can also significantly contribute to the GPI changes (Figure 4.8c). The relative contribution from PI, a quantity based on the temperature difference between sea surface and the tropopause, is small and not shown here. Given that CTL and NOGAP were forced with same SSTs, the minimal PI contribution means that CAGW variability is not able to influence atmospheric upper-level thermodynamic conditions.

GPI analysis reveals that the overall reduction of ENP TCs in response to closing the PP and TT gaps is mainly driven by the elimination of surface vorticity, with additional contributions from drier than normal mid-troposphere humidity. On the other hand, the reduced vertical wind shear makes environmental conditions more favorable for tropical cyclogenesis. It is still largely unknown how CAGW can modulate the mid-level relative humidity that in turn contributes to ENP TC variability. In next section, we will discuss the CAGW's secondary influences on environmental moisture changes.

4.5 Mid-level moisture changes associated with CAGW

Moisture changes are highly proportional to changes in rainfall (Trenberth, 1998), and in order to confirm if these moisture changes are indeed caused by CAGW variability, we first made rainfall composites based on synoptic CAGW events. Figure 4.9 shows the rainfall response to closing the TT and PP mountainous gaps. Rainfall is clearly enhanced on the windward slope of terrain and reduced on lee side in response to closing the mountain gaps. This rainfall dipole pattern that is exactly separated by the mountainous topography strongly hints that the rainfall associated moisture change may be tightly linked with mountain waves, rather than the direct influences from CAGW.

A mountain wave is an atmospheric gravity wave that is generated when stationary upstream flow passes over a mountain or mountain barrier. When uplifted upstream flow with sufficient moisture reaches lifted condensation level (LCL), the water vapor tends to condense and precipitate before it crosses the mountaintop, forming heavy rainfall on the

top and windward slope of the mountain. In consequence, the desiccated downslope wind, generates a drier side known as a "rain shadow". The TRMM3B43-derived hurricane season mean rainfall map illustrates an enlightening example (Figure 3.10c in Chapter III). The prevailing easterlies carry moisture from the Caribbean Sea and ascend when they approach the mountain barrier at PP. The flow is expanded and adiabatically cooled to the adiabatic dew point, and the moisture condenses onto the mountain and forms heavy rainfall. After the flow passes across the mountaintop at PP, the descending wind compresses adiabatically and increases the moisture saturation level due to the increased air temperature, and creates an arid region on lee side. The same feature is also shown near TT, but perhaps as stationary upstream flows from the Gulf of Mexico or North American continent do not have as much water vapor as the Caribbean Sea, the increase of rainfall on the upwind slope is not as strong as the PP (Figure 3.7c). However, the surface elevations at TT are higher than PP, making the adiabatic compression of descending flow even stronger on lee side of mountain, so that the "rain shadow" near TT is still significant. Note that these "rain shadows" are not directly caused by the CAGW variability, instead, they are more related to the fluctuations of steady upstream flow that have great potential to generate CAGW.

Figure 4.10 is the similar rainfall difference computed from TRMM3B43 satellite retrievals. We computed the rainfall difference by using the composite of rainfall during CAGW events minus the rainfall composite of non-CAGW events. The approach to identify synoptic CAGW events was introduced in Holbach and Bourassa (2014). We

used QuikSCAT satellite retrieved ocean surface winds to select the CAGW events, and the rainfall seasonal cycle was removed before applying composite analysis. As expected, the "rainfall shadow" is of particular significance during CAGW events, when the upstream flows are anomalously strong.

Even though total precipitation is influenced by mountain waves during the formation of CAGW, it is still unknown whether this fluctuation due to mountain blocking effect can modulate mid-level moisture, as surface elevations here are only confined to 3000m above the surface. To better elucidate this, we also made vertical cross sections across the PP and TT regions. Figure 4.11 shows the meridional mean vertical cross sections averaged from 10°N to 15°N with NOGAP surface elevations. The red and blue curves in Figure 4.11a are the isotropes derived from CTL and NOGAP simulation, respectively, superimposed by the differences of potential temperatures. It is clearly seen that the upstream overlapped isotropes split just ahead of the mountain barrier at 85°W, with blue curves located above on the windward slope and beneath on the lee side of mountain. This indicates the stronger wave-like fluctuations when geostationary flows pass over the mountainous topography without gaps, and results in the stronger ascending and descending winds than the real topography with the gap. As a consequence, NOGAP has more moisture release at the windward slope and top of the mountain, and less on the leeward side due to stronger adiabatic compression (Figure 4.11b).

Consistent with GPI analysis, the mid-level specific humidity is substantially decreased west of 95°W (Figure 4.11b), further confirming our arguments that the

significant TC suppression is contributed by both removal of low-level vorticity and decrease of mid-level moisture. This mid-level moisture change seems to be related with anomalous upper-level downward motion on downstream, instead of the influences from low-level.

Figure 4.12 shows a schematic plot of the mountain barrier's blocking effect on low-level prevailing easterlies. Blue arrows indicate an idealized case, in which mountainous gaps were closed and all flows are forced to trigger vertically propagating mountain waves. But in reality, the existence of the mountainous gap can deflect the flow to generate CAGW, and the residual ascending flows further generate weaker mountain waves, represented by red arrows. Of particular note, as the wind speed at upper-levels is relatively weak (no upper-level jet), forcing weak environmental vertical wind shear and high static stability, the mountain wave can propagate vertically and extend upward into the lower stratosphere. The winds at upper-level then bifurcate to two separate branches, easterlies blowing to the ENP, with westerlies towards the NA. The westerly winds have limited differences, while the downstream easterlies, which characterize wave-like motions with horizontal wavelengths of about 500km, change significantly. With stronger mountain-lifted upstream flows, the downstream upper-level shows weaker ascending flows. These negative anomalies of vertical velocity at upper-levels in turn blocks the humidity supplies from lower levels, making mid-levels drier than normal. This anomalous decrease of mid-level moisture content plays another important role in suppressing ENP TC activity, accompanying with the significant reduction of low-level

vorticity. But the reason why strengthened mountain waves can trigger remote weaker upward motions at upper-levels is still not clearly explored. More studies about affiliated mountain waves are essentially required.

Similar vertical cross sections along latitude, averaged from 97°W to 92°W are shown on Figure 4.13. Analogous mountain waves are triggered due to mountain's blocking on intermittent northerly winds, and decreased specific humidity can be found on the lee side. Nevertheless, this decrease of specific humidity is confined to low-levels only, and without the remote influences on vertical velocity, the mid-level humidity also remains unchanged.

4.6 Summary and discussion

In this chapter, we directly quantified the impact of CAGW on ENP TC activity, by conducting idealized experiments with artificially closed mountainous gaps at TT and PP using the improved TCM configuration. In response to closing the TT and PP gaps, and thereby eliminating the CAGWs, ENP TC activity decreased by about 25%. Time series and scatterplots reveal that this significant reduction is not confined to individual seasons with extremely weak TC activity, but instead occurs during the majority of TC seasons. In addition, the TC suppression due to the gap closures is almost uniformly distributed in the entire ENP. Furthermore, CAGW primarily modulates TC occurrence, while the impact on TC intensity is limited.

Based on GPI analysis, the synoptic CAGW-induced vorticity plays the key role in supporting TC genesis, whereas the gale-force easterly CAGW increases environmental VWS and potentially inhibits TCs. Due to the formation of CAGW, the original low-level prevailing easterlies from the Caribbean Sea are split, and the mountain-lifted ascending flows further generate mountain waves after passing over mountain barrier. The weaker than normal mountain waves further increase the mid-level humidity downstream, supporting more favorable environmental conditions for tropical cyclogenesis. Combined, CAGW makes a net positive contribution to ENP TCs, with ~25% of TC activity attributable to the existence of CAGWs.

With idealized topography experiments, we further proved that ENSO-induced intrabasin TC variability is dominated by CAGW's responses to ENSO modulation. Without CAGW, ENP TCs has a much higher correlation coefficient (~0.4) with the ENSO index. In the control simulation, this coefficient is only about 0.16, whereas the correlation coefficient for TCs originating in the EDR of ENP is significantly negative (–0.43). Scatterplots also indicate that the ENSO-induced intrabasin TC variability can be significantly eliminated by blocking CAGW. But due to the compensating contributions from ENSO-induced mid-level humidity changes (Figure 4.14; Figure 2.7; Figure 2.10) (e.g. decreased specific humidity during El Niño suppresses TC formations, while increased specific humidity during La Niña favors), the intrabasin variability still exists.

Our preliminary findings shed new light on the dynamics linking ENP TC activity to unique regional topographical features, the CAGWs, and highlight the particular

importance of improving CAGW simulation in models to make skillful seasonal forecasts of ENP TCs. However, the underlying dynamic mechanism responsible for mid-level moisture changes due to remote mountain waves is still not fully revealed, and further investigation is needed. And as with any modeling study, the existence of model biases is one source of uncertainty in the results. We emphasize that the simulated anomalous strengthened CAGW and climatologically low number of simulated TCs may overestimate our quantified relative contributions. Also, the atmospheric-only simulation excludes the processes of the air-sea interaction, through which CAGW can increase ocean vertical mixing and induce cooling effects on local SSTs (Alexander et al., 2012). However, the CAGW-induced decreased local SSTs are still much higher than 26.5°C (Figure 2.8 in Chapter II), a commonly used SST criteria that favors TC gensis, indicating that the CAGW's cooling effects may not directly influence tropical cyclogenesis. Whether it will delay TC's intensification is still unrevealed.

To more precisely understand CAGW's modulation on ENP TCs, and increase the TCM's ability in simulating seasonal TC activity, a finer resolution TCM coupled with a regional ocean model is highly suggested. The increased horizontal resolution may not be required for entire domain, and localized grid refinement over the ENP and western portion of NA may be sufficient for this research topic. These are areas of planned testing and development in future work.

Table 4.1 Simulated number of TCs from CTL and NOGAP simulations in climatology and during different ENSO phases. The ENSO difference is changing ratio relative to climatology. The numbers marked by ** and * denote the differences are significant at 5% and 10% levels (one-tailed t-test), respectively.

	CTL		NOGAP	
	ENP	ENP-EDR	ENP	ENP-EDR
Climatology	11.22	6.19	8.31	4.11
El Niño mean	11.04	5.25	9.42	4.04
El Niño difference	-1.61%	-15.12%*	+13.34%*	-1.69%
La Niña mean	10.06	7.22	7.28	4.39
La Niña difference	-10.40%	+37.56%**	-12.41%	+8.59%
Neutral ENSO mean	11.87	3.36	8.10	2.49
Neutral ENSO difference	5.79%	0.77%	-2.48%	-11.64%
Correlation with Niño3.4	0.1228	-0.389**	0.3568**	-0.024

Table 4.2 Similar to Table 4.1, but listing the accumulated days with simulated TCs in CTL and NOGAP simulations.

	CTL		NOGAP	
	ENP	ENP-EDR	ENP	ENP-EDR
Climatology	61.13	17.93	45.94	13.84
El Niño mean	61.23	14.46	54.49	13.13
El Niño difference	+0.16%	-19.37%*	+18.63%*	-5.18%
La Niña mean	54.26	23.26	40.33	15.39
La Niña difference	-11.24%	+60.90%**	-12.20%	+17.25%
Neutral ENSO mean	64.24	13.73	43.26	11.24
Neutral ENSO difference	5.09%	1.23%	-5.83%	-1.33%
Correlation with Niño3.4	0.1801	-0.4572**	0.4069**	0.0155

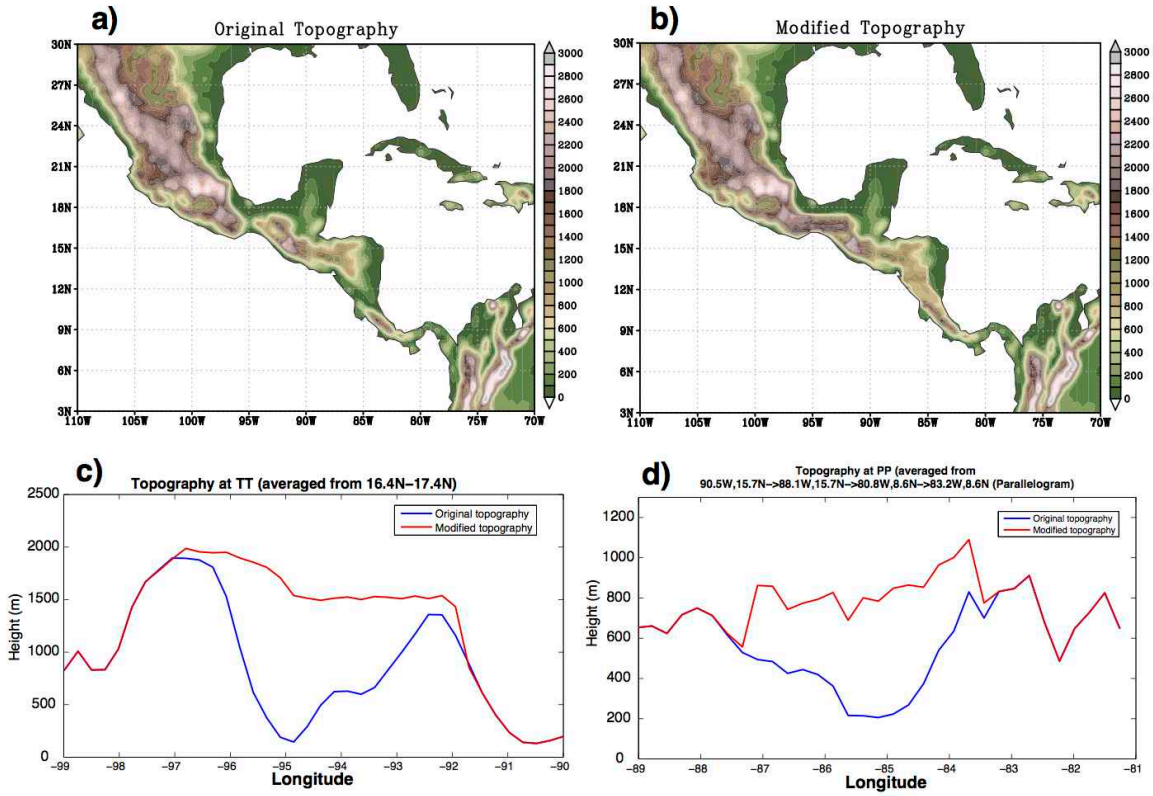

Figure 4.1 Topography (unit: m) data used by TCM for a) CTL and b) NOGAP simulations. c) and d) area-averaged surface elevation for TT and PP. Blue curves show original elevations, while red curves show modified elevations.

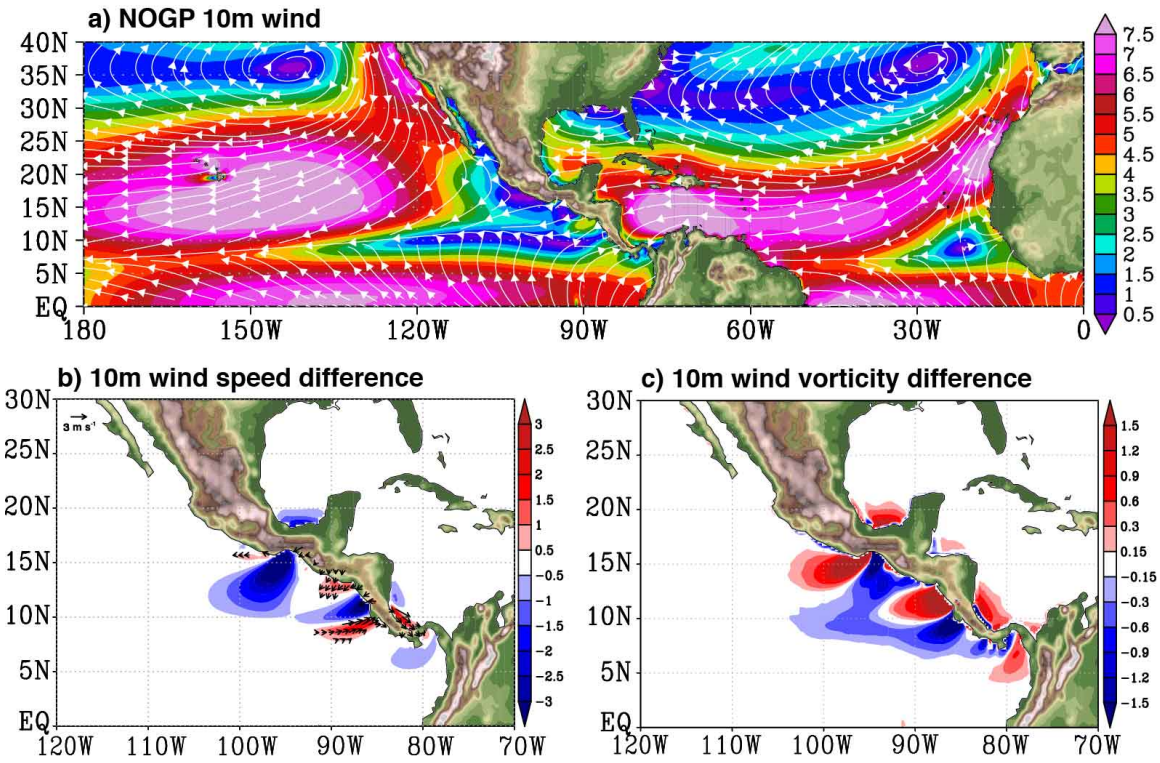

Figure 4.2 a) Composite of JJASON 1990-2016 averaged 10-m wind over oceans from 3-member ensemble TCM NOGAP simulations. Color shading indicates wind velocity (unit: m s^{-1}), and streamline indicates wind direction. Difference of b) wind speed (unit: m s^{-1}) and c) relative vorticity (unit: 10^{-5} s^{-1}) relative to CTL. Vector denotes the wind vector anomalies stronger than 0.5 m s^{-1}.

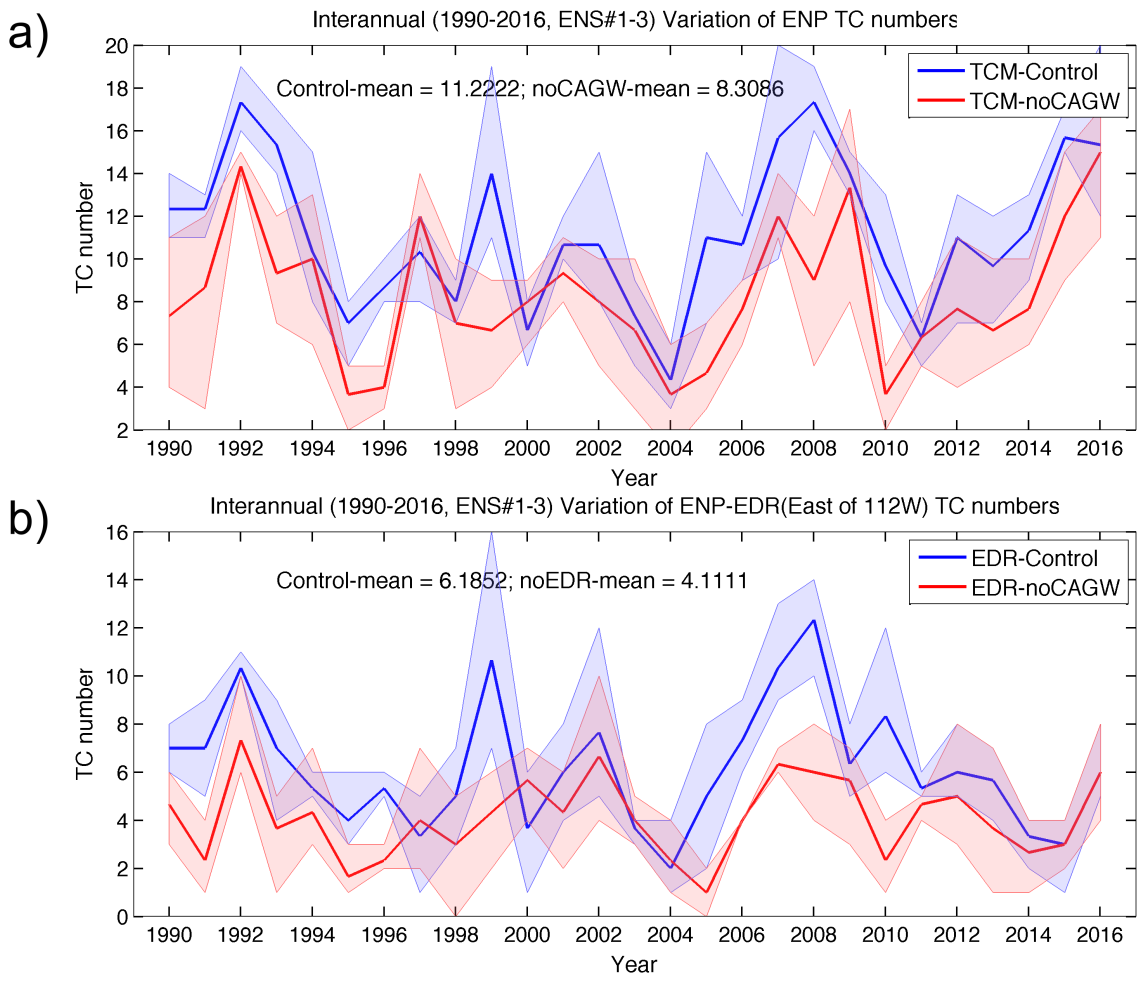

Figure 4.3 Time series of simulated hurricane season mean number of TCs over a) ENP and b) EDR of ENP from CTL simulation (blue curves) and NOGAP simulation (red curves). The mean values of each curves are listed on the panel.

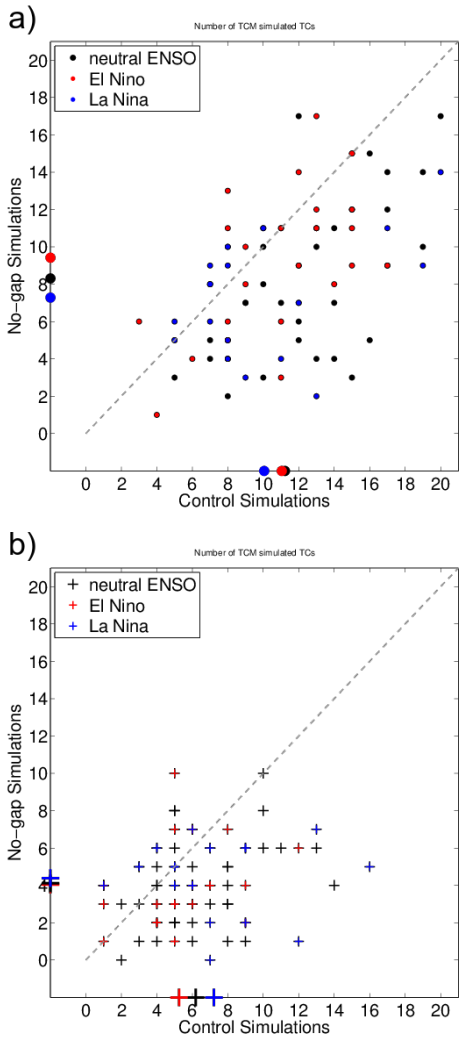

Figure 4.4 Scatterplots of simulated hurricane seasons mean number of TCs over a) ENP and b) EDR of ENP from 3-member ensemble TCM CTL versus NOGAP simulations. Gray line is the diagonal line with the slope of 1. Black, red, and blue indicate neutral ENSO, El Niño, and La Niña hurricane seasons, respectively. The markers on the axes represent the mean values averaged from each category (e.g. the red dot on the x-axis of the top panel indicates the mean value of simulated TC numbers from CTL during El Niño hurricane season).

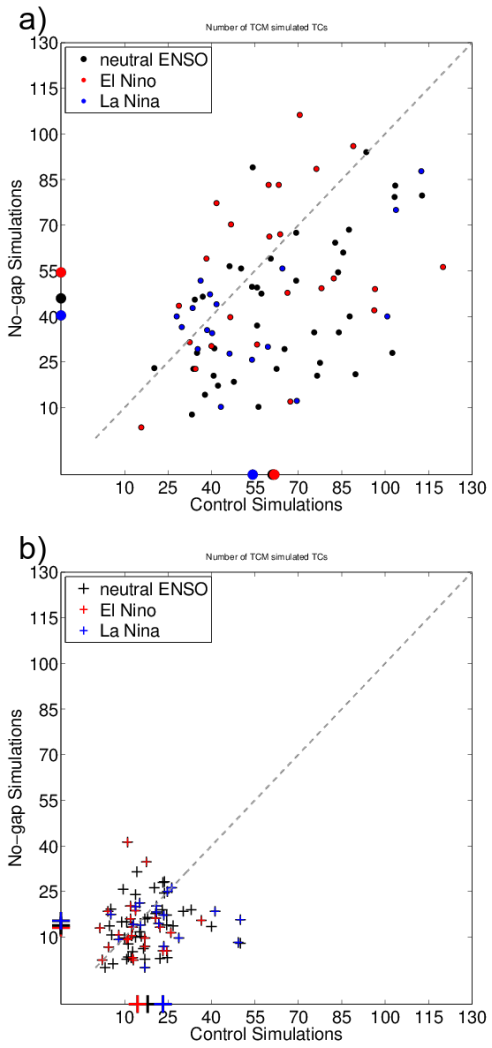

Figure 4.5 Similar to Figure 4.4, but for the scatterplot of simulated number of TC days from CTL versus NOGAP simulations.

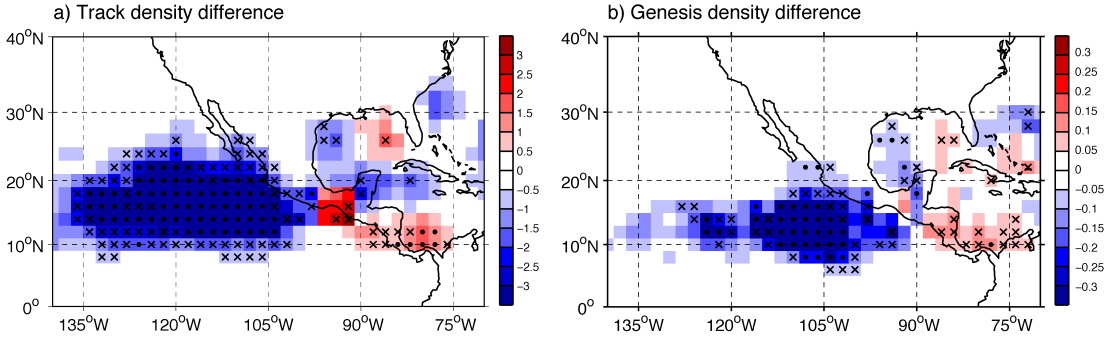

Figure 4.6 Composite differences of a) track density and b) genesis density from NOGAP minus CTL simulation (unit: TCs per decade). Black dots (crosses) denote statistical confidence at the 95% (90%) level.

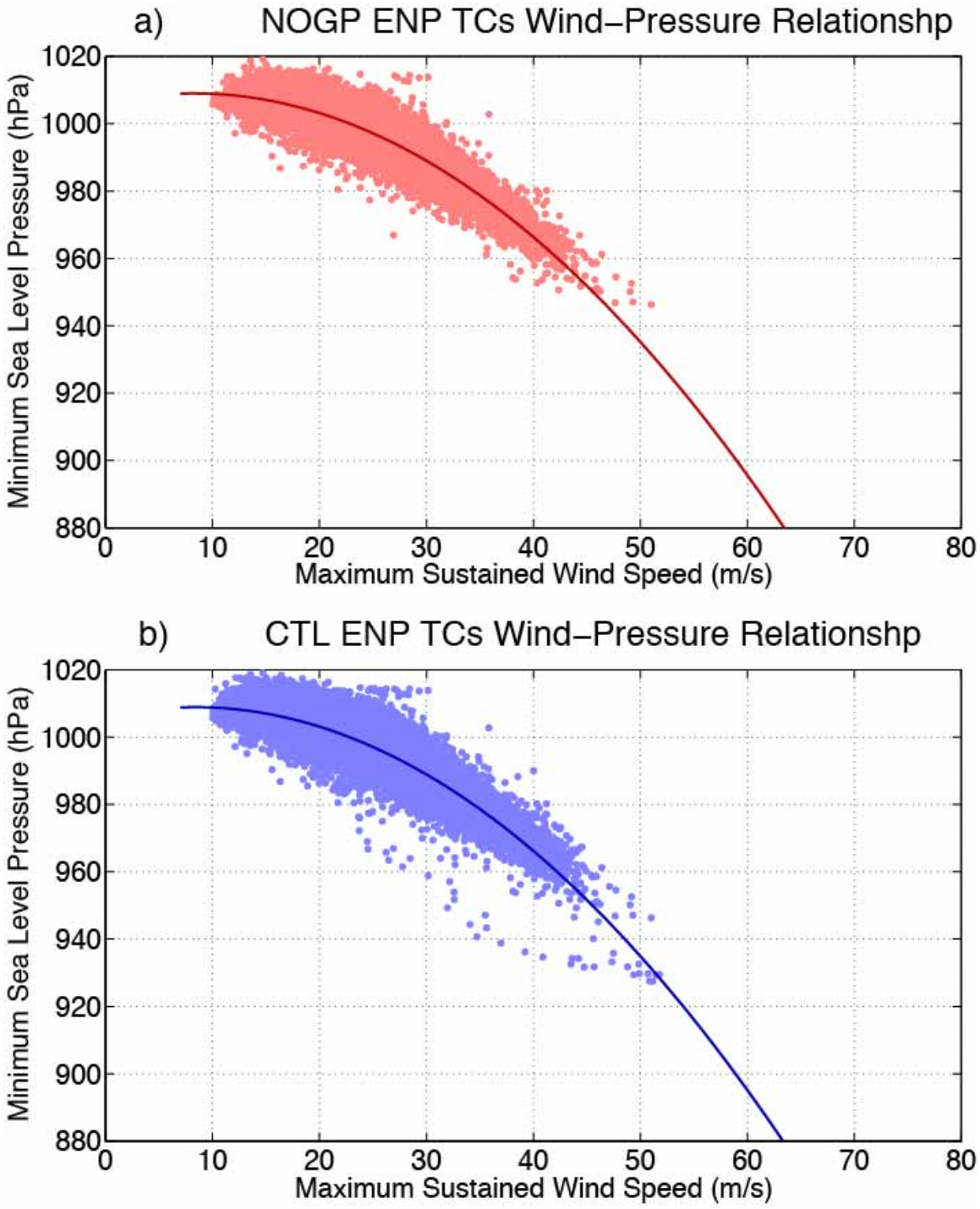

Figure 4.7 Scatterplots of simulated TC surface maximum wind speed versus minimum sea level pressure from a) NOGAP and b) CTL simulation. Solid lines are least squares quadratic best-fit lines to the points.

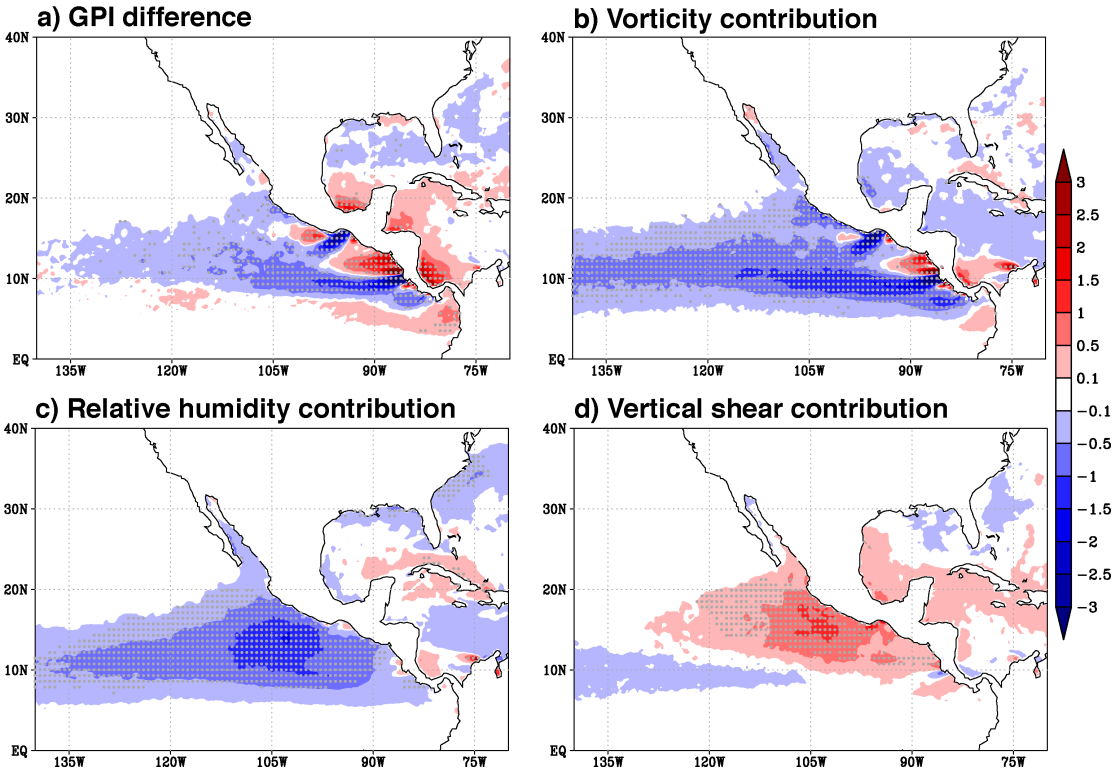

Figure 4.8 a) GPI difference (unitless) from NOGAP minus CTL simulation. The relative contribution to GPI difference from b) 850 hPa vorticity, c) 600 hPa relative humidity and d) 200-850 hPa vertical wind shear term. Potential intensity term's contribution is small, and not shown. The contributions are estimated in same way as documented in Patricola et al., (2015). Gray dots highlight statistical confidence at the 95% level. Positive anomalies indicate more favorable conditions for TC genesis.

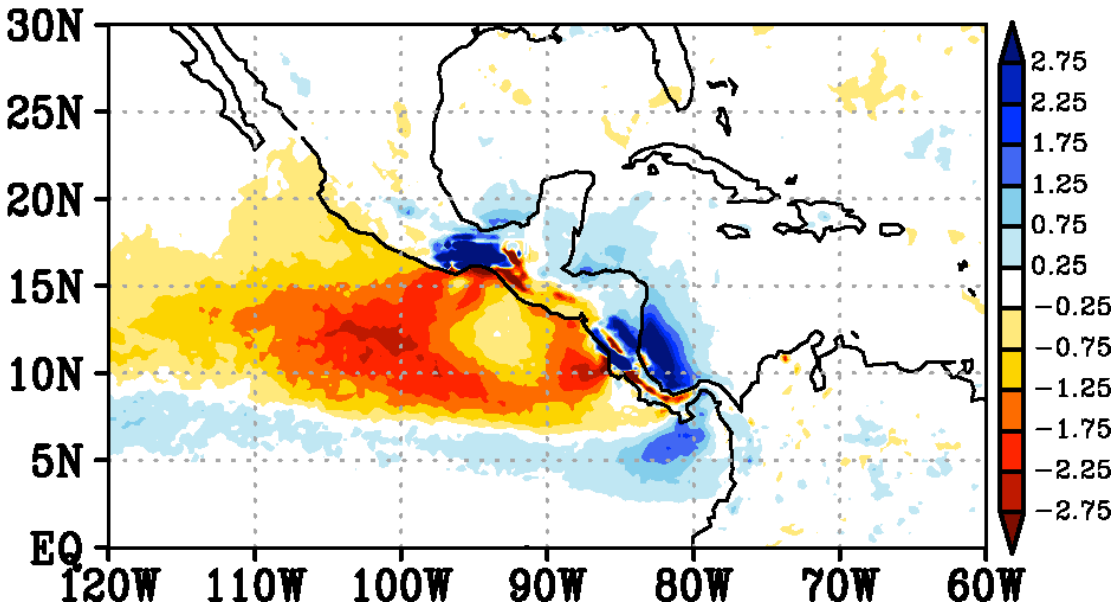

Figure 4.9 Composite differences of rainfall (unit: mm day^{-1}) from NOGAP minus CTL simulation. Note that cold color shadings indicate more rainfall while warm colors indicate less rainfall

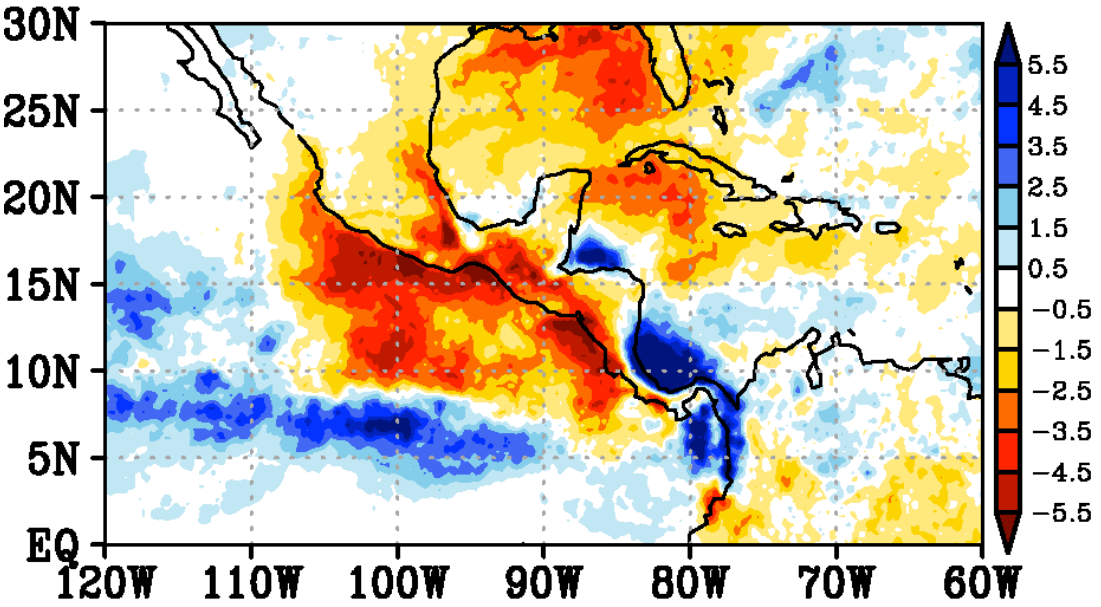

Figure 4.10 TRMM3B43 retrieval of rainfall difference (unit: mm day^{-1}) during CAGW events relative to non-CAGW events.

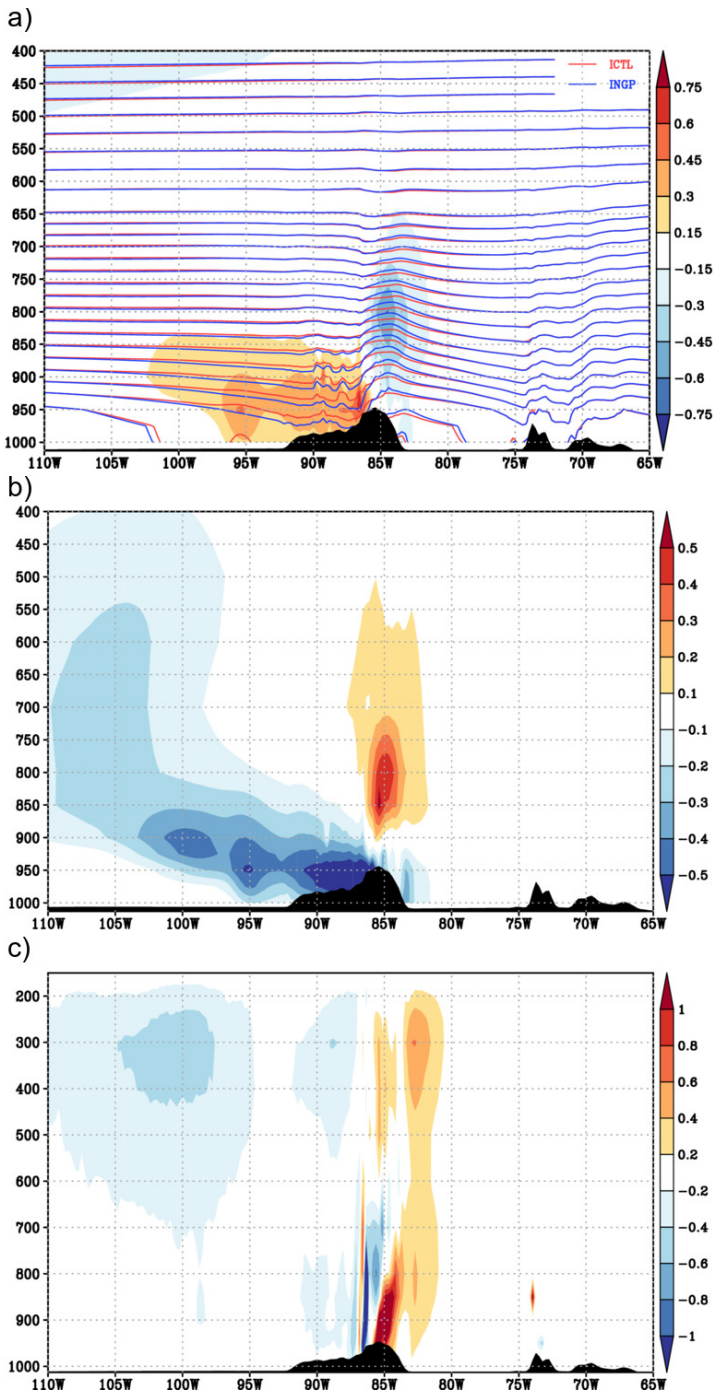

Figure 4.11 Meridional mean vertical cross section of a) potential temperature (contour; unit: K), b) specific humidity (shading; unit: g/kg) and c) vertical velocity (unit: cm s^{-1}) difference averaged from 10°N-15°N. Difference is calculated from NOGAP minus CTL simulation. Red and blue curves in panel a) indicate isotropes from CTL and NOGAP, respectively. Isotropes have the interval of 1K when potential temperature is below 315K, and 2K above 315K. Black shadings indicate the surface elevations from NOGAP simulation.

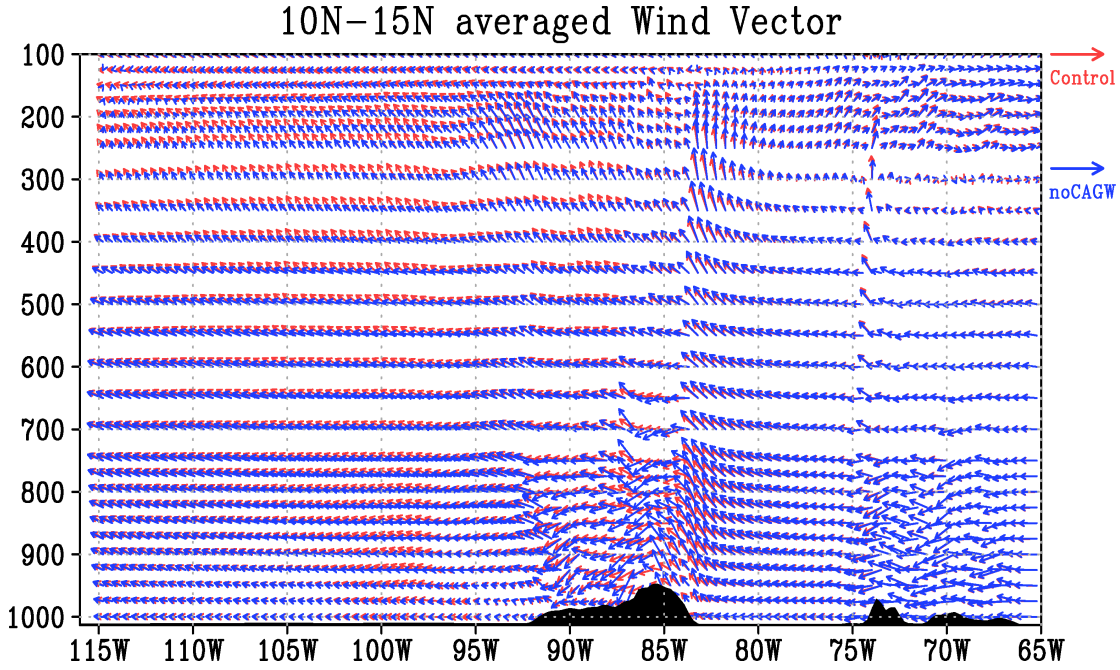

Figure 4.12 Schematic plot of mountain's blocking effect on easterlies near PP. Red and blue arrows indicate the cases of normal and non-gap topography, respectively. Note that the vertical velocity is scaled up by a factor of 500 for clarity.

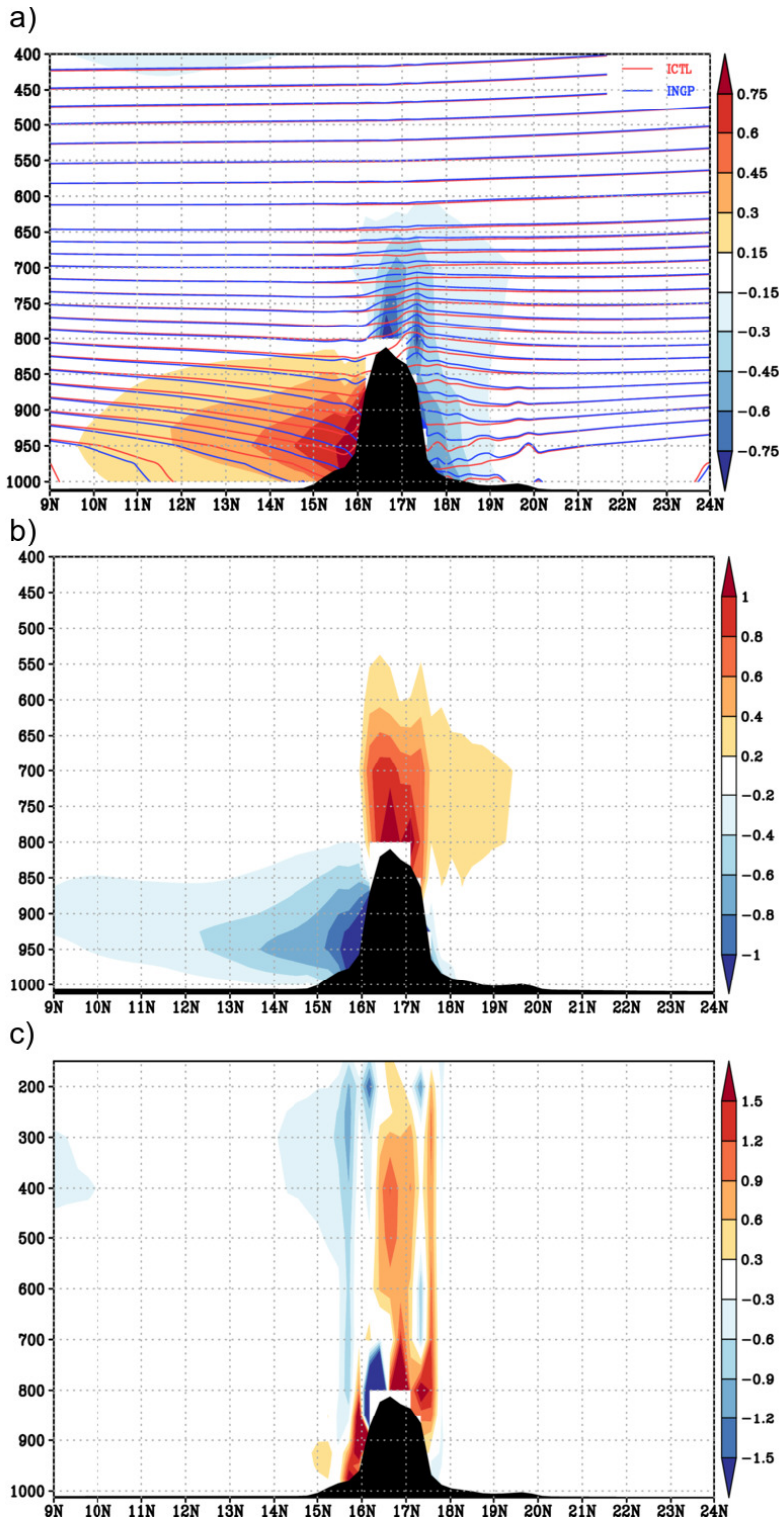

Figure 4.13 Same as Figure 4.11, but for zonal mean vertical cross section averaged from 97°W-92°W.

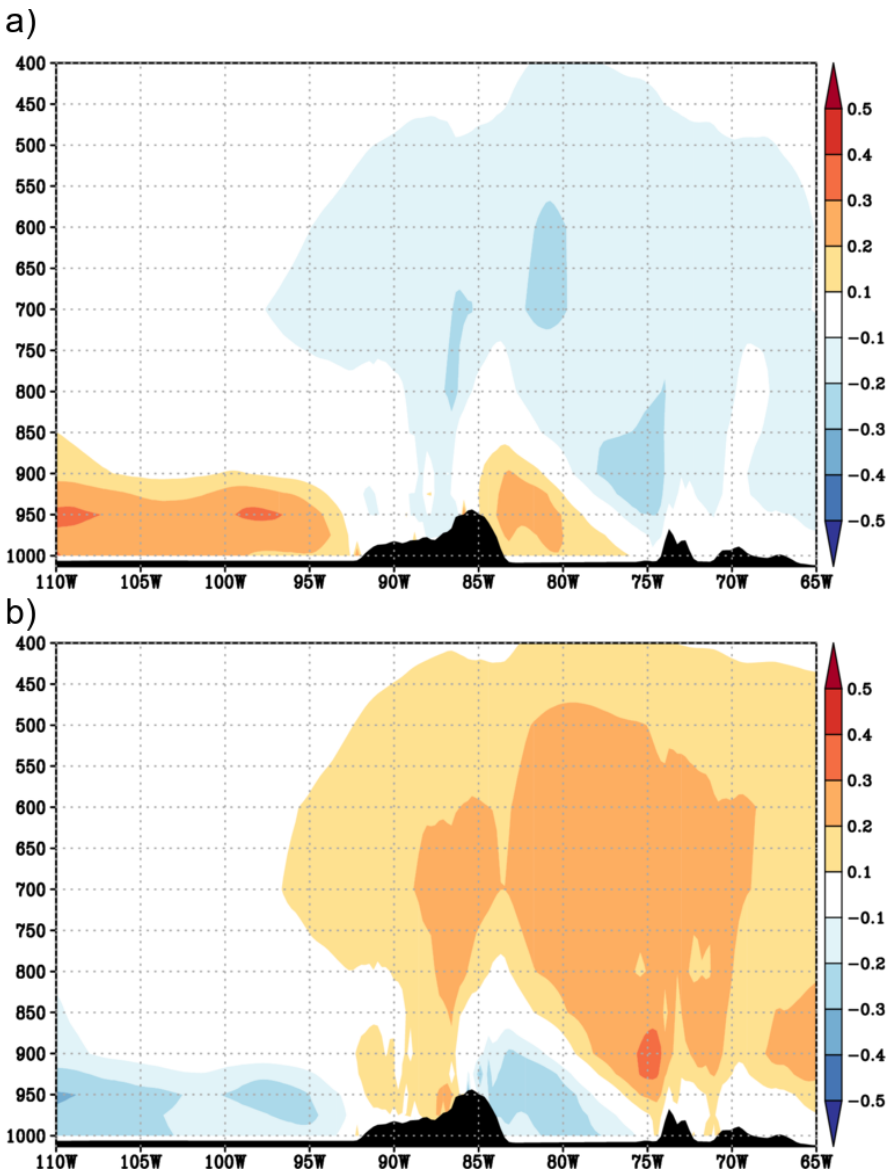

Figure 4.14 NOGAP simulated meridional mean vertical cross section of specific humidity anomaly (unit: g kg^{-1}) during a) El Niño and b) La Niña relative to 27-season climatology.

CHAPTER V

CONCLUSIONS AND FUTURE WORK

The impacts of Central American gap winds (CAGW) on eastern North Pacific (ENP) tropical cyclones (TCs) are investigated in this dissertation. A unique topographically-locked feature, the Sierra Madre, generally blocks the low-level flows from the north Atlantic (NA), except for three narrow passages at the Isthmus of Tehuantepec (TT), Gulf of Papagayo (PP), and in Central Panama (PN). These narrow mountain gaps generate gale-force CAGW, which in turn triggers significant near-surface vorticity perturbations through horizontal shear effect and additional jet curvatures. Since initial low-level cyclonic vorticity is very important for TC genesis, how these vorticity perturbations can contribute to ENP TC activity was unknown. Our findings suggest that CAGWs drive timescale-dependent and spatially-dependent responses in tropical cyclogenesis. On the seasonal timescale, we conducted composite analysis of TC track density and genesis density based on different phases of the El Niño-Southern Oscillation (ENSO) in observations and simulations with a newly improved Tropical Channel Model (TCM) based on the Weather Research and Forecasting (WRF) model. To further investigate the underlying dynamic processes that control TC variations, we evaluated the genesis potential index (GPI) and the relative contributions from each of four component terms. On the synoptic scale, we performed two sets of experiments with real topography (CTL) and idealized topography without mountain gaps (NOGAP) to hindcast 1990-2016

hurricane seasons using the TCM. Sensitivity experiments were first conducted to determine the optimal TCM configuration for reproducing realistic regional circulation features and ENP TC activity. Rigorous analyses were explored to quantify CAGW's impacts on ENP TCs on difference timescales. The main conclusions of this dissertation research are summarized as follows.

5.1 Conclusions

The previous convectional view that El Niño (La Niña) drives basin-wide enhancements (reductions) of ENP TC activity through decreased (increased) vertical wind shear, anomalous warm (cold) SST, and a more (less) humid mid-troposphere is incomplete. We found that ENSO instead drives spatially-complex patterns in ENP TC activity. Indeed, composites of observed track and genesis density suggests that ENSO drives intrabasin ENP TC variability, with enhanced TC activity confined only to western portion, with TC reductions over the eastern nearshore area during El Niño. The opposite sign of changes are observed during La Niña. GPI analysis suggests that this west-east spatial pattern in the ENP TC response to ENSO is primarily forced by CAGW-induced anomalous low-level vorticity during ENSO. Stronger CAGW during El Niño results in net anticyclonic vorticity anomalies unfavorable for TC formation, while cyclonic vorticity anomalies during La Niña in turn favor TC formation.

To fully quantify CAGW's influence on ENP TCs, numerical modeling with precise representations of regional circulations is essential. By making large sets of sensitivity

tests of model physical parameterization schemes, we developed a new TCM configuration which has great ability to capture reasonable CAGW and ENP TC distributions, as compared against observations and reanalyses. In addition, the newly configured TCM is able to simulate ENSO-induced intrabasin ENP TCs variability, which is a great improvement from the old configuration with significant model biases and allows us to further understand the observationally-based findings.

We next investigated the impact of the CAGWs on the synoptic timescale by conducting TCM simulations with artificially closed topography at the mountainous gaps at TT and PP. With the TT and PP gaps closed, the CAGW are clearly blocked in the TCM simulation, while keeping other large-scale features analogous to control simulations that use real topography. After eliminating the CAGW, the TCM produces ~26% fewer ENP TCs and ~25% less accumulated days with TC occurrence. This significant suppression is especially effective in the eastern nearshore area, but the overall impacts cover the entire ENP. Furthermore, the ENSO-induced intrabasin TC variability can also be significantly eliminated just by blocking the CAGW, further confirming CAGW's dominant role in west-east variations of TC response to ENSO.

An environmental favorability analysis suggests that although CAGW-triggered low-level vorticity contributes most to the ENP TC formations, increased vertical shear between upper-level westerlies and low-level easterly jets can inhibit TC genesis. In addition to the direct impacts on the low-level, CAGW-affiliated mountain waves can also influence mid-level moisture content, which is another important factor that

modulates ENP TCs. The presence of CAGW deflects the steady upstream flows, whereas a mountain wave is generated when residual flows pass over artificially imposed mountainous barriers. This mountain wave can remotely generate mid-level moisture supplying from low-level, and make environment conditions more favorable for tropical cyclogenesis.

Our findings shed new light on the dynamical linkage between ENP TC activity and the unique topography-locked CAGW feature. As all historical ENP TCs that made landfall onto the American Continent formed in the eastern nearshore area of the ENP, this dissertation highlights the importance of properly resolving and representing CAGW to improve seasonal ENP TC forecasting skill.

5.2 Future work

Despite the progress we made in this dissertation to better elucidate the underlying physical processes that control CAGW's modulation on ENP TCs, there are still some questions remaining to be solved in future research.

First, as documented in Chapter II, the formation of ENSO-induced mid-level humidity anomalies over Central America, which acts as another source of intrabasin variability, is still unknown. Of particular note is that many previous studies only focused on the ENSO peak season, that is boreal winter. How ENSO's modulation on the atmospheric circulation during boreal summer and fall of the ENSO onset year is largely unknown. More investigations should be undertaken in future studies.

Second, although the newly configured TCM shows great improvement from the previous version, in terms of more realistic simulated ENP TC distributions and relevant regional circulation features, it still exhibits some biases. The TCM tends to overestimate frequency and magnitude of CAGW, while the simulated number of ENP TCs is systematically less than the observed. Combined, these biases are a source of uncertainty in our results. Also, the lack of air-sea interaction processes in the atmospheric only TCM may potentially influence the simulated TCs. To more comprehensively understand CAGW's impact on regional circulation, an atmosphere-ocean coupled TCM with finer resolution is highly recommended. This is a target for future research.

Third, we still lack fundamental understanding of CAGW-affiliated mountain wave's remote impacts on downstream flows. Why the uplifted upstream flows due to mountain's blocking can bifurcate to easterly and westerly branches at upper-levels is another subject of intensive study. More high-resolution numerical simulation and *in situ* observational studies are clearly needed to better understanding this scientific question.

REFERENCES

Alexander, M. A., Seo, H., Xie, S. P., and J. D. Scott, 2012: ENSO's Impact on the Gap Wind Regions of the Eastern Tropical Pacific Ocean. Journal of Climate, 25(10), 3549-3565.

Atlas, R., R. N. Hoffman, J. Ardizzone, S. M. Leidner, J. C. Jusem, D. K. Smith, D. Gombos, 2011: A cross-calibrated, multiplatform ocean surface wind velocity product for meteorological and oceanographic applications. Bulletin of the American Meteorological Society, 92, 157-174.

Avila, L. A., 1991: Eastern North Pacific hurricane season of 1990. Monthly Weather Review, 119, 2034–2046.

Avila, L. A., and R. J. Pasch, 1992: Atlantic tropical systems of 1991. Monthly Weather Review, 120, 2688–2696.

Avila, L., 2016: The 2015 Eastern North Pacific Hurricane Season: A very active Year. Weatherwise, 69, 36-42.

Bell, G. D., and Coauthors, 2000: Climate assessment for 1999. Bulletin of the American Meteorological Society, 81, S1–S50.

Bister, M., and K. A. Emanuel, 1998: Dissipative heating and hurricane intensity. Meteorology and Atmospheric Physics, 65, 233–240.

Bister, M., and K. A. Emanuel, 2002: Low frequency variability of tropical cyclone potential intensity. 1. Interannual to interdecadal variability. Journal of Geophysical Research, 107, 4801.

Bourassa, M. A., L. Zamudio, and J. O'Brien, 1999: Noninertial flow in NSCAT observations of Tehuantepec winds. Journal of Geophysical Research, 104 (C5), 311–319.

Bove, M. C., O'Brien, J. J., Eisner, J. B., Landsea, C. W., and X. Niu, 1998: Effect of El Niño on US landfalling hurricanes, revisited. Bulletin of the American Meteorological Society, 79(11), 2477-2482.

Brennan, M. J., Cobb III, H. D., and R. D. Knabb, 2000: Observations of Gulf of Tehuantepec gap wind events from QuikSCAT: An updated event climatology and operational model evaluation. Weather Forecasting, 25, 646-658.

Camargo, S. J., Emanuel, K. A., and A. H, Sobel, 2007: Use of a genesis potential index to diagnose ENSO effects on tropical cyclone genesis. Journal of Climate, 20(19), 4819-4834.

Camargo, S. J., A. W. Robertson, A. G. Barnston, and M. Ghil, 2008: Clustering of eastern North Pacific tropical cyclone tracks: ENSO and MJO effects. Geochemistry, Geophysics, Geosystems, **9,** Q06V05.

Camargo, S. J., M. C. Wheeler, and A. H. Sobel, 2009: Diagnosis of the MJO modulation of tropical cyclogenesis using an empirical index. Journal of the Atmospheric Sciences, 66, 3061–3074.

Chan, J. C. L., 1985: Tropical cyclone activity in the northwest Pacific in relation to the El Niño/Southern Oscillation phenomenon. Monthly Weather Review, 113, 599–606.

Chang, P., Saravanan, R., L. Ji and G.C. Hegerl, 2000: The Effect of Local Sea-Surface Temperatures on Atmospheric Circulation over the Tropical Atlantic Sector, Journal of Climate, 13, 2195-2216.

Charney, J. G., and A. Eliassen, 1964: On the growth of the hurricane depression. Journal of the Atmospheric Sciences, 21(1), 68-75.

Chelton, D. B., Freilich, M. H. and S. K. Esbensen, 2000a: Satellite observations of the wind jets off the Pacific coast of Central America. Part I: Case studies and statistical characteristics. Monthly Weather Review, 128, 1993-2018.

Chelton, D. B., Freilich, M. H. and S. K. Esbensen, 2000b: Satellite observations of the wind jets off the Pacific coast of Central America. Part II: Regional relationships and dynamical considerations. Monthly Weather Review, 128, 2019–2043.

Chelton, D. B., M. G. Schlax, M. H. Freilich, and R. F. Milliff, 2004: Satellite measurements reveal persistent small-scale features in ocean winds. Science, 303, 978–983.

Chen, T.-C., Wang, S.-Y., Yen, M.-C., & Gallus Jr., W. A. (2004). Role of the monsoon gyre in the interannual variation of tropical cyclone formation over the western North Pacific. *Weather Forecasting*, 19, 776–785.

Chen, T.-C., Wang, S.-Y., Yen, M.-C., & Clark, A.J. (2008b). Are tropical cyclones less effectively formed by easterly waves in the western North Pacific than in the North Atlantic? Monthly Weather Review, 136, 4527–4540.

Chiang, J. C. H., and D. J. Vimont, 2004: Analagous meridional modes of atmosphere-ocean variability in the tropical Pacific and tropical Atlantic. Journal of Climate,17(21), 4143-4158.

Chu, P. S., and J. Wang, 1997: Tropical Cyclone Occurrences in the Vicinity of Hawaii: Are the Differences between El Niño and Non-El Niño Years Significant?*. Journal of Climate, 10(10), 2683-2689.

Chu, P-S., 2004: ENSO and tropical cyclone activity. *Hurricanes and Typhoons, Past, Present and Future,* R. J. Murnane and K.-B. Liu, Eds., Columbia University Press, 297–332.

Collins, J. M., and I. M. Mason, 2000: Local environmental conditions related to seasonal tropical cyclone activity in the northeast Pacific basin. Geophysical research letters, 27(23), 3881-3884.

Collins, J. M., 2007: The relationship of ENSO and relative humidity to interannual variations of hurricane frequency in the North-East Pacific ocean. Papers of Applied Geography Conferences, 30, 324-333.

Collins, J. M., 2010: Contrasting high North-East Pacific tropical cyclone activity with low North Atlantic activity. Southeastern Geographer, 50(1), 83-98.

Collins, J.M. et al., 2016: The Record-Breaking 2015 Hurricane Season in the eastern North Pacific: An Analysis of Environmental Conditions. Geophysical. Research. Letter. 43, 9217-9224.

Crétat, J., B. Pohl, Y. Richard, and P. Drobinski, 2011b: Uncertainties in simulating regional climate of Southern Africa: Sensitivity to physical parameterizations using WRF. Climate Dynamics, 38, 613-634.

Dai, A., and T. M. L., Wigley, 2000: Global patterns of ENSO‐induced precipitation. Geophysical Research Letters, 27(9), 1283-1286.

Dudhia, J., 1989: Numerical study of convection observed during the winter monsoon experiment using a mesoscale two-dimensional model. Journal of the Atmospheric Sciences, 46, 3077–3107.

Dunn, G. E. (1940). Cyclogenesis in the tropical Atlantic. Bulletin of the American Meteorological Society, 21, 215-229.

Efron, B. and R. Tibshirani, 1991: Statistical data analysis in the computer age. Science 253, 390-3953.

Emanuel, K. A., 1986: An air-sea interaction theory for tropical cyclones. Part I: Steady-state maintenance. Journal of the Atmospheric Sciences, 43(6), 585-605.

Emanuel, K. A., 1995: Sensitivity of tropical cyclones to surface exchange coefficients and a revised steady-state model incorporating eye dynamics. Journal of the Atmospheric Sciences, 52, 3969–3976.

Emanuel, K. A., and D. Nolan, 2004: Tropical cyclone activity and global climate. Preprints, 26th Conf. on Hurricanes and Tropical Meteorology, Miami, FL, Amer. Meteor. Soc., 240–241.

Emanuel, K., and A. Sobel, 2013: Response of tropical sea surface temperature, precipitation, and tropical cyclone ‐ related variables to changes in global and local forcing. Journal of Advances in Modeling Earth Systems, 5(2), 447-458.

Englehart, P. J., and A. V. Douglas, 2001: The role of eastern North Pacific tropical storms in the rainfall climatology of western Mexico. International Journal of Climatology, 21(11), 1357-1370.

Englehart, P. J., and A. V. Douglas, 2002: Mexico's summer rainfall patterns: an analysis of regional modes and changes in their teleconnectivity. Atmósfera, 15(3), 147-164.

Evans, J. P., M. Ekstrom, and F. Ji, 2012: Evaluating the performance of a WRF physics ensemble over south-east Australia. Climate Dynamics, 39, 1241-1258.

Farfàn, L. M., and J. Zehnder, 1997: Orographic influence on the synoptic-scale circulations associated with the genesis of Hurricane Guillermo (1991). Monthly Weather Review, 125, 2683–2698.

Frank, N. L. (1970). Atlantic Tropical Systems of 1969. Monthly Weather Review, 98, 307-314.

Frank, W. M., 1977: The structure and energetics of the tropical cyclone. I. Storm structure. Monthly Weather Review, 105, 1119–1135.

Frank, W. M. (1988). Tropical cyclone formation. A Global View of Tropical Cyclones, R. L. Elsberry, Ed., Office of Naval Research, 53–90.

Fu, D., P. Chang, and C. M. Patricola, 2016: Intrabasin variability of East Pacific tropical cyclones during ENSO regulated by central American gap winds, Scientific Reports, 7.

Gray, W. M., 1979: Hurricanes: Their formation, structure and likely role in the tropical circulation. Meteorology over the tropical oceans, 77, 155-218.

Gray, W. M., 1984a: Atlantic seasonal hurricane frequency. Part I: El Niño and 30 mb quasi-biennial oscillation influences. Monthly Weather Review, 112, 1649–1668.

Gray, W. M., and J. D. Sheaffer, 1991: El Niño and QBO influences on tropical cyclone activity. Teleconnections Linking Worldwide Anomalies, M. H. Glantz, R. W. Katz, and N. Nicholls, Eds., Cambridge University Press, 257–284.

Gutzler, D. S., Wood, K. M., Ritchie, E. A., Douglas, A. V., an M. D. Lewis, 2013: Interannual variability of tropical cyclone activity along the Pacific coast of North America. Atmósfera, 26, 149-162.

Han, J., and H.-L. Pan, 2011: Revision of convection and vertical diffusion schemes in the NCEP Global Forecasting System. Wea. Forecasting, 26, 520–533.

Holbach, H. M., and M. A. Bourassa, 2014: The effects of gap-wind-induced vorticity, the monsoon trough, and the ITCZ on east Pacific tropical cyclogenesis. Monthly Weather Review, 142(3), 1312-1325.

Irwin, R. P., and R. E. Davis, 1999: The relationship between the Southern Oscillation

Index and tropical cyclone tracks in the eastern North Pacific. Geophysical research letters, 26(15), 2251-2254.

Jien, J. Y., Gough, W. A., and K. Butler, 2015: The Influence of El Niño–Southern Oscillation on Tropical Cyclone Activity in the Eastern North Pacific Basin. Journal of Climate, 28(6), 2459-2474.

Karnauskas, K. B., Busalacchi, A. J., and R. Murtugudde, 2008: Low-frequency variability and remote forcing of gap winds over the east Pacific warm pool. Journal of Climate, 21(19), 4901-4918.

Kimberlain, T. B., Blake, E. S. and J. P. Cangialosi, 2016: "Tropical cyclone report: Hurricane Patricia (EP202015) 20-24 October 2015" (Technic Report, National Hurricane Center, Miami, FL).

Klotzbach, P. J., 2014: The Madden–Julian oscillation's impacts on worldwide tropical cyclone activity. J. Climate, 27, 2317–2330.

Knapp, K. R., Kruk, M. C., Levinson, D. H., Diamond, H. J., and C. J. Neumann, 2010: The international best track archive for climate stewardship (IBTrACS) unifying tropical cyclone data. Bulletin of the American Meteorological Society, 91(3), 363-376.

Knutson, T., J. Sirutis, S. Garner, I. Held, and R. E. Tuleya, 2007: Simulation of the recent multidecadal increase of Atlantic hurricane activity using an 18-km-grid regional model. Bull. Amer. Meteor. Soc., 88,1549–1565.

Lander, M.A. (1994). An exploratory analysis of the relations between tropical storm formation in the western north Pacific and ENSO. Monthly Weather Review, 122, 636-651.

Landsea, C.W. (1993). A climatology of intense (or major) Atlantic hurricanes. Monthly Weather Review, 121, 1703-1713.

Landsea, C. W., 2000: El Niño–Southern Oscillation and the seasonal predictability of tropical cyclones. El Niño: Impacts of Multiscale Variability on Natural Ecosystems and Society, H. F. Díaz and V. Markgraf, Eds., Cambridge University Press, 149–181.

Levine, A. S., 2012: The influence of gap wind events on the monsoon trough and implications for eastern North Pacific cyclogenesis. 30th Conference on Hurricanes and Tropical Meteorology, Ponte Vedra, FL, Amer. Meteor. Soc., 3C.3.

Liang, J. H., J. C. McWilliams, and N. Grube, 2009: The high-frequency response of the ocean to mountain gap winds in the northeastern tropical Pacific. Journal of Geophysical Research, 114, C12005.

Lin, Y.-L., R. D. Farley, and H. D. Orville, 1983: Bulk parameterization of the snow field in a cloud model. J. Climate Appl. Meteor., 22, 1065–1092.

Manabe S., J. L. Holloway, and H. M. Stone, 1970: Tropical circulation in a time-integration of a global model atmosphere. Journal of the Atmospheric Sciences, 27, 580–613.

Mlawer, E. J., S. J. Taubman, P. D. Brown, M. J. Iacono, and S. A. Clough, 1997: Radiative transfer for inhomogeneous atmosphere: RRTM, a validated correlated-k model for the long wave. J. Geophys. Res., 102, D14. 16663–16682.

Molinari, J., D. Knight, M. Dickinson, D. Vollaro, and S. Skubis, 1997: Potential vorticity, easterly waves, and eastern Pacific tropical cyclogenesis. Monthly Weather Review, 125, 2699–2708.

Molinari, J., D. Vollaro, S. Skubis, and M. Dickinson, 2000a: Origins and Mechanisms of Eastern Pacific Tropical Cyclogenesis: A Case Study. Monthly Weather Review, 128, 125–139.

Molinari, J., and D. Vollaro, 2000b: Planetary- and synoptic-scale influences on eastern Pacific tropical cyclogenesis. Monthly Weather Review, 128, 3296–3307.

Montgomery, M. T., and J. Enagonio, 1998: Tropical cyclogenesis via convectively forced vortex Rossby waves in a three-dimensional quasigeostrophic model. Journal of the Atmospheric Sciences, 55, 3176–3207.

Mozer, J. B., and J. A. Zehnder, 1996: Lee vorticity production by large-scale tropical mountain ranges. Part I: Eastern North Pacific tropical cyclogenesis. Journal of Atmospheric Sciences, 53, 521–538.

Murakami, H., B. Wang, and A. Kitoh, 2011: Future change in western North Pacific typhoons: Projections by a 20-km-mesh global atmospheric model. Journal of Climate, 24, 1154–1169.

Nasrollahi, N., A. AghaKouchak, J. Li, X. Gao, K. Hsu,

and S. Sorooshian, 2012: Assessing the impacts of different WRF precipitation physics in hurricane simulations. Weather Forecasting, 27, 1003–1016.

Nicholls, N., 1979: A possible method for predicting seasonal tropical cyclone activity in the Australian region. Monthly Weather Review, 107, 1221–1224.

Patricola, C. M., Chang, P., and R. Saravanan, 2015: Degree of simulated suppression of Atlantic tropical cyclones modulated by flavour of El Niño. Nature Geoscience, 9, 155-160.

Patricola, C. M., R. Saravanan, and P. Chang, 2017: A teleconnection between Atlantic sea surface temperature and eastern and central North Pacific tropical cyclones, Geophysical Research Letter, 44, 1167–1174.

Philander, S. G., 1990: *El Niño, La Niña, and the southern oscillation* (Academic Press, Cambridge, MA).

Ralph, T. U. and W. A. Gough, 2009: The influence of sea surface temperature on eastern North Pacific tropical cyclone activity. Theoretical and Applied Climatology. 95, 257-264.

Rasmusson, E. M., and T. H. Carpenter, 1982: Variations in Tropical Sea Surface Temperature and Surface Wind Fields Associated with the Southern Oscillation/El Niño. Monthly Weather Review, 110, 354–384.

Ricciardulli, L., and F.J. Wentz, 2015: A scatterometer geophysical model function for climate-quality winds: QuikSCAT Ku-2011. Journal of Atmospheric and Oceanic Technology, 32, 1829-1846.

Ritchie, E. A., (1995). Mesoscale aspects of tropical cyclone formation. (Ph.D. dissertation), Centre for Dynamical Meteorology and Oceanography, Monash University, Melbourne, Victoria, Australia, 167 pp.

Ritchie, E. A., K. M. Wood, D. S. Gutzler, and S. R. White, 2011: The influence of Eastern Pacific tropical cyclone remnants on the southwestern United States, Monthly Weather Review, 139, 192–210

Ritchie, E. A., and G. J. Holland, 1997: Scale interactions during the formation of Typhoon Irving. Monthly Weather Review, 125, 1377– 1396.

Rogers, R. F., S. Aberson, M. M. Bell, D. J. Cecil, J. D. Doyle, J. Morgerman, L. K. Shay, and C.Velden, 2017: Rewriting the tropical record books: The extraordinary intensification of Hurricane Patricia (2015). Bulletin of the American Meteorological Society, 98, 2091–2112.

Romero-Centeno, R., Zavala-Hidalgo, J., Gallegos, A., and J. J. O'Brien, 2003: Isthmus of Tehuantepec wind climatology and ENSO signal. Journal of Climate, 16(15), 2628-2639.

Romero-Vadillo, E., O. Zaytsev, and R. Morales-Pérez, 2007: Tropical cyclone statistics in the northeastern Pacific, Atmosfera, 20, 197–213.

Russell, J. O., Aiyyer, A., White, J. D., & Hannah, W. (2017). Revisiting the connection between African Easterly Waves and Atlantic tropical cyclogenesis. *Geophysical Research Lett*er, 44, 587–595.

Saha, S., and Coauthors, 2010: The NCEP Climate Forecast System Reanalysis. Bulletin of the American Meteorological Society, 91, 1015–1057.

Saha, S., and Coauthors, 2014: The NCEP Climate Forecast System Version 2. Journal of Climate, 27, 2185-2208.

Schultz, D. M., W. E. Bracken, L. F. Bosart, G. J. Hakim, M. A. Bedrick, M. J. Dickinson, and K. R. Tyle, 1997: The 1993 Superstorm cold surge: Frontal structure, gap flow, and tropical impact. Monthly weather review,125, 5–39.

Skamarock, W. C., J. B. Klemp, J. Dudhia, D. O. Gill, D. M. Barker, W. Wang, and J. G. Powers, 2005: A description of the Advanced Research WRF version 2. NCAR Tech. Note NCAR/TN-468+STR, 88 pp.

Simpson, J., Ritchie, E., Holland, G. J., Halverson, J., and S. Stewart, 1997: Mesoscale interactions in tropical cyclone genesis. Monthly weather review, 125(10), 2643-2661.

Steenburgh, W. J., Schultz, D. M., and A. B. Colle, 1998: The structure and evolution of gap outflow over the Gulf of Tehuantepec, Mexico. Monthly weather review,126, 2673-2691.

Stumpf, H. G., 1975b: Satellite detection of upwelling in the Gulf of Tehuantepec, Mexico. Journal of Physical Oceanography, 5, 383–388.

Sun, F., and J.-Y. Yu, 2006: Impacts of Central America gap winds on the SST annual cycle in the eastern Pacific warm pool. Geophysical Research Letters, 33, L06710.

Tang, B. H., and J. D. Neelin, 2004: ENSO influence on Atlantic hurricanes via tropospheric warming. Geophysical Research Letters, 31(24).

Trenberth, K. E., 1998: Atmospheric moisture residence times and cycling: Implications for rainfall rates with climate change. Climatic Change, 39, 667–694.

Waliser, D. E., and Coauthors, 2012: The "year" of tropical convection (May 2008–April 2010): Climate variability and weather highlights. Bulletin of the American Meteorological Society, 93, 1189–1218.

Walsh, K., and Coauthors, 2015: Hurricanes and climate: The U.S. CLIVAR working group on hurricanes. Bulletin of the American Meteorological Society, 96, 997–1017.

Wang, B., and J. C. Chan, 2002: How strong ENSO events affect tropical storm activity over the western North Pacific. Journal of Climate, 15(13), 1643-1658.

Whitney, L. D., and J. S. Hobgood, 1997: The relationship between sea surface temperatures and maximum intensities of tropical cyclones in the Eastern North Pacific Ocean, Journal of Climate, 10, 2921–2930.

Wood, K. M., and E. A. Ritchie (2013), An updated climatology of tropical cyclone impacts on the southwestern United States. *Monthly Weather Review*, *141*(12), 4322-4336.

Xie, S.-P., H. Xu, W. S. Kessler, and M. Nonaka (2005), Air–sea interaction over the

eastern Pacific warm pool, gap winds, thermocline dome, and atmospheric convection. *J. Climate*, *18*, 5–20.

Yoshida, R. & Ishikawa, H. (2013). Environmental factors contributing to tropical cyclone genesis over the western North Pacific. Monthly Weather Review, 141, 451–467.

Zarzycki, C. M., Jablonowski, C., Thatcher, D. R., & Taylor, M. A. (2015). Effects of localized grid refinement on the general circulation and climatology in the Community Atmosphere Model. *Journal of Climate*, *28*(7), 2777-2803.

Zehnder, J. A., 1991: The interaction of planetary-scale tropical easterly waves with topography: A mechanism for the initia- tion of tropical cyclones. J. Atmos. Sci., 48, 1217–1230.

Zehnder, J. A., and R. L. Gall, 1991: On a mechanism for orographic triggering of tropical cyclones in the eastern North Pacific. Tellus, 43A, 25–36.

Zhao, H., and G. B. Raga, 2015: On the distinct interannual variability of tropical cyclone activity over the eastern North Pacific. Atmósfera 28.3, 61-178.